

Extreme Air-Sea Interactions over the Gulf Stream

Rhys Parfitt

THESIS SUBMITTED FOR THE DEGREE
OF DOCTOR OF PHILOSOPHY OF
IMPERIAL COLLEGE LONDON AND FOR
THE DIPLOMA OF IMPERIAL COLLEGE
LONDON

May, 2014

Space and Atmospheric Physics Group,
The Blackett Laboratory,
Imperial College London,
London SW7 2BW,
UK

Student Declaration

I hereby declare that the work presented in this thesis is my own and that all else is appropriately referenced.

Rhys Parfitt

Copyright Declaration

The copyright of this thesis rests with the author and is made available under a Creative Commons Attribution Non-Commercial No Derivatives licence. Researchers are free to copy, distribute or transmit the thesis on the condition that they attribute it, that they do not use it for commercial purposes and that they do not alter, transform or build upon it. For any reuse or redistribution, researchers must make clear to others the licence terms of this work.

Acknowledgements

My first acknowledgements must go to my supervisor Arnaud Czaja, whose seemingly limitless knowledge and generosity has guided me throughout this entire project. He has been a friend as well as a mentor and I am immensely grateful for everything he has done. I would like to direct thanks to my thesis committee, Jo Haigh and Bob Forsyth, for all the helpful comments through the years, with additional thanks to the former for agreeing to be my internal Viva exam assessor. Thanks must also go to my external Viva exam assessor, Ian Boutle, for taking the time to review and examine the research presented in these pages.

Thanks to all the members of the Space and Atmospheric Group, who have provided me with such a pleasant work environment and have also allowed me many interesting discussions over the years. I give special thanks to my closest friend from Imperial, Gordon, who has been there throughout the entirety of this PhD, and has been like a brother to me.

Finally, I would like to thank my mother and my father, whose constant love and support have been unyielding for my entire life. Mum, you are simply the kindest person I know and Dad, I can truly only hope to one day become the man that you are. I dedicate this thesis to both of you.

Rhys Parfitt

Abstract

The ocean carries more heat poleward than the atmosphere at low latitudes, whilst the reverse occurs at high latitudes. In the Northern Hemisphere, the largest ocean-atmosphere heat fluxes occur over the Gulf Stream, suggesting that an ocean-atmosphere “relay” is active at mid-latitudes. This thesis is concerned with the significance of the extremes in air-sea heat fluxes over the Gulf Stream.

In the first research chapter, the direct interaction between the ocean and the atmosphere is examined in the ERA-Interim dataset. Based on Lagrangian trajectory calculations, the most extreme air-sea heat flux events are found to be associated entirely with air of continental origin. The subsequent heat gain in the overlying air is caused almost completely by surface heat fluxes. For average air-sea heat fluxes, the associated air is both continental and maritime in origin, with a noticeable contribution to the heat content of the air parcels from entrainment at the top of the boundary layer.

The second research chapter determines the causes for variations in surface heat flux in the ERA-Interim dataset. Roughly 90% of the time, one observes a baroclinic waveguide of varying strength over the Gulf Stream, setting the intensity of the air-sea heat exchange and the mean state in precipitation and tropospheric wind divergence. A potential mechanism whereby a change in sea-surface temperature gradient could cause an alteration of these mean patterns is discussed.

Finally, the link between sea-surface temperature gradients and atmospheric fronts is explored in model simulations. A smoothing in the sea-surface temperature gradient is found to broadly reduce front intensity over the Gulf Stream.

Increases in front intensity are shown to be consistent with a thermal damping mechanism. A significant effect is also observed on the regional precipitation and tropospheric vertical velocity, as well as on the direction of frontal propagation.

Contents

1. Introduction	22
1.1 Earth's meridional temperature gradient	22
1.2 Potential vorticity	24
1.3 Mid-latitude cyclogenesis	25
1.4 Mid-latitude storm tracks	27
1.5 Western Boundary Currents and air-sea interactions	30
1.6 Ocean-atmosphere turbulent heat fluxes	34
1.7 Extratropical cyclone structure	36
1.8 Thesis outline	39
2. A Lagrangian view of air-sea interactions over the Gulf Stream	
Stream	42
2.1 Introduction	42
2.2 Gulf Stream heat flux index	43
2.2.1 Heat flux dataset	43
2.2.2 Gulf Stream heat flux domain	45
2.3 The Lagrangian Trajectory Model	50
2.3.1 Initial development	50
2.3.2 Specification	51
2.3.3 The Eady model	53
2.3.4 Theoretical testing of the LTM	57
2.3.5 Qualitative comparison with a realistic case	66
2.4 EE and ME trajectory analysis	68
2.5 The Gulf Stream boundary layer heat budget	76
2.5.1. Moist enthalpy	79

2.5.2 The boundary layer heat budget	83
2.6 Conclusions	90
3. The contribution of extreme events to the mean atmospheric state in the Gulf Stream region in wintertime	93
3.1 Introduction	93
3.2 The variation of surface heat flux with atmospheric state	
3.3 The contribution of extremes to the mean pattern in precipitation over the Gulf Stream	101
3.4 The contribution of extremes to the mean pattern in tropospheric wind divergence over the Gulf Stream	107
3.5 Attempting to understand the interaction of the Gulf Stream Front with synoptic atmospheric transients	113
3.6 Conclusions	120
4. The impact of sea-surface temperature on atmospheric fronts propagating over the Gulf Stream	126
4.1 Introduction	126
4.2 Model dataset	128
4.2.1 Sea-surface temperature	128
4.2.2 Identification of atmospheric fronts	130
4.3 The effect of sea-surface temperature gradient on atmospheric front strength	134
4.4 Thermal damping of fronts	137
4.5 Steering of atmospheric fronts by sea-surface isotherms	140
4.6 The effect of sea-surface temperature gradient on vertical velocity and precipitation	144
4.6.1 Precipitation	144

4.6.2 Vertical velocity	149
4.7 Conclusions	157
5. Conclusions	161
Bibliography	168
Appendix	186
A.1 Symbols and Physical Constants	186
A.2 Abbreviations	188

List of Figures

- 1.1 Annual mean of the zonal mean potential temperature in ERA-40 data, 1979-2001 (Källberg et al., 2005).
- 1.2 Schematic detailing how baroclinic instability leads to cyclone formation. Near-surface temperature contours are shown, as is the tropopause location, with positive PV anomalies indicated with a + and arrows denoting associated airflows. (a) A PV anomaly at the tropopause induces weak cyclonic vorticity at the surface. (b) This induced vorticity distorts the surface meridional temperature gradient. (c) This surface vorticity now feeds back to the tropopause.
- 1.3 NH winter storm track structure based on high-pass time-filtered transients in ECMWF data for DJF 1979-84. The thin contours are of height variance (contour interval 15m^2) and arrows indicate the vector $(\overline{v'^2 - u'^2}, \overline{-u'v'})$, both at 250hPa. Also shown are single contours of the 700hPa horizontal temperature flux (thick dashed contour at 10 K m s^{-1}), 700hPa vertical temperature flux (thick dotted contour at 0.2 K Pa s^{-1}), and the column mean diabatic heating (thick solid contour at 50 W m^{-2}). (Hoskins and Valdes, 1990).
- 1.4 Diagram of the five major ocean gyres (boxed). Major ocean currents are marked by arrows and annotated. Figure courtesy of the National Oceanography Centre.

- 1.5 Annual climatology of rain rate: (a) observed by satellites, and in the AFES with (b) observed and (c) smoothed SSTs. Contours of SST are also shown at 2°C intervals, with dashed contours for 10°C and 20°C (Minobe et al., 2008).
- 1.6 The required total heat transport from the top-of-atmosphere radiation (RT) is compared with the derived estimate of the adjusted ocean heat transport (OT) and implied atmospheric transport (AT) (Trenberth and Caron, 2001).
- 1.7 Schematic illustrating the frontal structure and airflows within a mid-latitude cyclone. The cold and warm fronts are denoted by the blue and red lines respectively. The three main airflows are shown by arrows, along with an indication of their inflow and outflow levels. The cold conveyor belt remains near the surface throughout.
- 2.1 Wintertime (DJF) heat flux data 1979-2011. (a) Average global surface latent heat flux. (b) Average global surface sensible heat flux. (c) Total (latent and sensible) surface heat flux over the Gulf Stream. Land is illustrated in white. The rectangular box shown is the Gulf Stream Domain used in this Chapter. (d) GS domain-averaged total heat flux for DJF 1979 calculated in red as the average between 12:00 and 15:00UTC and in black as the average across the whole day. (e) The standard deviation of the average total daily heat flux. All figures are in Wm^{-2} .
- 2.2 In blue: GS domain-averaged total daily latent heat flux, averaged across (a) EEs and (b) MEs with a time lag of $\pm 3\text{d}$. The green and red lines represent \pm one standard deviation in the heat flux

across each set of days.

- 2.3 Eady-wave theoretical test analysis of the LTM for an initial potential temperature perturbation of 0.1K and a LTM time-step of 1 hour. In blue: Numerically solved 8-day wave trajectories. In green: 4-day forward- and back-trajectories as produced by the LTM. In red: The difference between the LTM and the numerical solution. See text for further description.
- 2.4 As in Figure 2.3, but for an initial potential temperature perturbation of 1K.
- 2.5 As in Figure 2.3, but for an initial potential temperature perturbation of 10K.
- 2.6 As in Figure 2.3, but for a LTM time step of 1 minute.
- 2.7 As in Figure 2.3, but for an initial temperature perturbation of 1K and a LTM time step of 1 minute.
- 2.8 As in Figure 2.3, but for an initial temperature perturbation of 10K and a LTM time step of 1 minute.
- 2.9 (Right) Six-day forward trajectories, and three-day backward trajectories, starting 12:00 UTC 23 Jan 1987, of which the first 2 days were identified as a WCB, using the Lagrangian model FLEXTRA (Eckhardt et al., 2004). Positions along the forward trajectories are marked every 24h. (Left) Comparable calculations done by the LTM for 3 days forward and backward trajectories.
- 2.10 Trajectory positions at $t = 0\text{d}$, $3\frac{1}{4}$ days before 12:00UTC on (a) EEs and (b) MEs.

- 2.11 Average across all trajectories on EEs (red) and MEs (blue) of the (a) parcel longitude and latitude (b) parcel pressure height and (c) parcel geopotential height.
- 2.12 Average across all trajectories on EEs (red) and MEs (blue) of the (a) parcel relative humidity (b) parcel specific humidity (c) parcel moist static energy (d) parcel temperature (e) overlying tropopause height and (f) underlying surface pressure.
- 2.13 Surface pressure at $t = 3\frac{1}{4}$ d, averaged across (a) EEs and (b) MEs. (c) Average mean sea level pressure, 12:00UTC, DJF, 1979-2011.
- 2.14 (a)-(e) Composites of the MSLP averaged across EEs from two days prior to the EEs through to two days afterwards.
- 2.15 As in Figure 2.14, but for MEs.
- 2.16 Trajectory positions at $t = 6\frac{1}{2}$ d, $3\frac{1}{4}$ days after 12:00UTC on (a) EEs and (b) MEs.
- 2.17 Average on EEs (red) and MEs (blue) of the parcel geopotential height, parcel specific humidity and parcel temperature across all trajectories that end up (a,c,e) north of 35.25°N (b,d,f) south of 35.25°N . It is noted that the vertical scale is different in (a) and (b), and in (c) and (d).
- 2.18 Average on EEs (red) and MEs (blue) of the parcel moist static energy and overlying tropopause height across all trajectories that end up (a,c) north of 35.25°N (b,d) south of 35.25°N .
- 2.19 In blue: GS domain-averaged daily boundary layer height, averaged across (a) EEs and (b) MEs with a time lag of ± 3 d. The green and red lines represent \pm one standard deviation in the boundary

layer height across each set of days. The corresponding time t is also given for reference.

- 2.20 Main processes affecting the boundary layer heat budget over the GS. Strong ocean-atmosphere heat fluxes exist at the surface, with entrainment flux affecting at the boundary layer top. Radiation is represented with a “net” arrow at the boundary layer top, but naturally exists at the surface as well, and can act to cool or warm the boundary layer. The net flux in the horizontal is assumed to be zero.
- 2.21 In blue: The thermal energy budget in the MABL above the GS domain for each of the representative trajectories on EEs. A line of unit gradient is shown in red and the line of best fit is shown in black.
- 2.22 As in Figure 2.21, but for trajectories on MEs.
- 3.1 Time-mean wintertime anomalies in the mean sea-level pressure, averaged across deciles in the GSI from (a) 0-10% to (j) 90-100%. The thirty-three year average wintertime mean sea-level pressure is shown in (k). The rectangular black box in each plot represents the Gulf Stream domain.
- 3.2 Composite of MSLP, averaged across the bottom 10% in the GSI, with a lag of (i) -1 (ii) 0 (iii) + 1 days.
- 3.3 Composite of (a) the tropopause depth and (b) the boundary layer height, averaged across the top 10% in the GSI, with a lag of (i) -1 (ii) 0 (iii) +1 days.
- 3.4 Tropopause depth, averaged across deciles in the GSI from (a) 0-10%

to (j) 90-100%. The thirty-three year average wintertime tropopause depth is shown in (k). The rectangular black box in each plot represents the Gulf Stream domain.

- 3.5 As in Figure 3.4, but for the boundary layer height.
- 3.6 Contribution of each decile in GSI, from (a) 0-10% to (j) 90-100%, towards the thirty-three year average wintertime convective precipitation (k). Sea-surface temperature contours from 8°C to 26°C at intervals of 2°C are marked in white. Continental grid points are marked out in white.
- 3.7 As in Figure 3.6, but for the large-scale precipitation.
- 3.8 Composite of total precipitation averaged across the bottom 10% in the GSI, with a lag of (i) - 2 (ii) -1 (iii) 0 (iv) + 1 (v) + 2 days.
- 3.9 The relative percentage contribution of (a) the bottom 20% and (b) the top 20% in GSI towards the convective and large-scale precipitation in the GS region.
- 3.10 Twenty-year wintertime mean of (a) convective precipitation and (b) large-scale precipitation, showing both the GS domain and the domain (42-64.5W,33-43.5N).
- 3.11 Contribution of each decile in GSI, from (a) 0-10% to (j) 90-100%, towards the thirty-three year average wintertime wind divergence at 950hPa (k). Sea-surface temperature contours from 8°C to 26°C at intervals of 2°C are marked in black. Continental grid points are marked out in white.
- 3.12 Contribution of each decile in GSI, from (a) 0-10% to (j) 90-100%, towards the thirty-three year average wintertime upper-level (500hPa-

200hPa averaged) wind divergence (k). Sea-surface temperature contours from 8°C to 26°C at intervals of 2°C are marked in black. Continental grid points are marked out in white.

- 3.13 As in Figure 3.10, but for the vertical velocity at 950hPa.
- 3.14 Composites of vertical velocity time-mean anomalies averaged across (a) the top 10% and (b) the bottom 10% in the GSI, at 500hPa, with a lag of (i) - 2 (ii) -1 (iii) 0 (iv) + 1 (v) + 2 days.
- 3.15 Composite of tropopause depth (contour) and boundary layer height (colour) in the GS region, averaged across EEs.
- 3.16 Longitudinal composites of meridional ((a),(c),(e)) and vertical velocity ((b),(d),(f)), averaged across EEs with each day centred on the maximum in tropopause depth at constant latitude 37.5°, with a lag of ((a),(b)) -1, ((c),(d)) 0, ((e),(f)) +1 days.
- 3.17 Longitudinal composites of atmospheric potential vorticity, averaged across EEs with each day centred on the maximum in tropopause depth at constant latitude 37.5°, with a lag of (a) -1, (b) 0, (c) +1 days. The tropopause and the boundary layer top are represented by thin black lines and contours of potential temperature are also marked.
- 3.18 Schematic showing the flow structure induced by a (a) positive and (b) negative PV anomaly of simple shape. The location of each PV anomaly is stippled. The tropopause is marked by the thick black line, and thin lines are of isentropes every 5 K and transverse velocity every 3 m s⁻¹ (Hoskins et al., 1985).

- 3.19 As in Figure 3.17, but for the 1% of days between the 89.5% and 90.5% highest indices in the GSI.
- 3.20 Schematic representation of flow in a deep tropospheric motion system, projected upon a vertical section. The hatched area at the surface represents the layer of small-scale convection, within which subsiding air has its potential temperature raised. Air from this layer enters a cumulonimbus or large-scale circulation and ascends into the upper troposphere. Condensation, C, of water vapour occurs, and small-scale convection may develop again in the cloud system where there is cross-hatching. Precipitation falls from the cloud (pecked lines) and there is some evaporation, E, outside it. The descending branch of the large-scale circulation is left open on the right to indicate that it continues in several motion systems, accompanied by a slow radiative loss of potential temperature. T marks the tropopause. (Green et al., 1966).
- 4.1 Transverse motion in an idealized frontal zone, with warmer air to the left. The frontogenic horizontal deformation field is such that the meridional velocity increases with latitude, and all isotherms in isobaric surfaces are assumed parallel with the front. Dashed lines: zonal velocity isotachs. Dotted lines: meridional velocity isotachs. Solid lines: streamlines of transverse non-geostrophic circulation. (Eliassen, 1962)
- 4.2 Twenty-year wintertime mean (DJF 1981-2000) of SST for the (a) CNTL experiment and (b) SMTH experiment. Contours, in black, are shown from 2°C to 20°C, at 2°C intervals. Also shown on both figures, and annotated in (b), are the lines of constant longitude

used for analysis in this chapter. These are (70W, 29.7-43.2N), (60W, 29.7-45.2N), (50W, 29.7-49.7N), (40W, 29.7-49.7N), (30W, 29.7-49.7N). The difference in SST between the CNTL and SMTH experiment is shown in (c).

- 4.3 An example surface map for a baroclinic wave with a strong surface cold front and a developing warm front. Temperature contours every 4K are shown as continuous lines, geopotential contours are marked with dashed lines, and the region of relative vorticity larger than $\frac{f}{2}$ is shaded. The relative vorticity in the cold front region has a maximum of $5f$. (Hoskins, 1982).
- 4.4 (a) An atmospheric front, as defined in the text, highlighted in magenta, at 12:00UTC on December 28th 1981. Also shown at that time is the vertical velocity (colour), and contours of SST from 2°C to 20°C, at 2°C intervals (black). (b) Another atmospheric front, as defined in the text, identified at 18:00UTC on February 28th 2001. (c) Fraction of wintertime days in the CNTL experiment where the front variable F exceeds unity. Contours of SST are as in Fig. 4.2(a). (d) Percentage of wintertime days where (i) a cold front and (ii) a warm front is objectively identified in the Atlantic, from Berry et al. (2011).
- 4.5 (a) As in Figure 4.4(c), but for the SMTH experiment. (b) The percentage reduction in the occurrence of $F \geq 1$ in the SMTH experiment, relative to the CNTL experiment.
- 4.6 (a) Average wintertime value of F when an atmospheric front ($F \geq$

- 1) is present, with the percentage reduction in F in the SMTH relative to the CNTL experiments shown in (b). This percentage change is calculated for two higher thresholds of atmospheric front intensity in (c) $F \geq 3$ and (d) $F \geq 5$.
- 4.7 Schematic of an atmospheric cold front passing over (a) a strong SST gradient (b) a smoothed SST gradient.
- 4.8 Schematic illustrating the angles δ_1 and δ_2 between the frontal horizontal temperature gradient at 925hPa and lines of constant longitude, for cold fronts and warm fronts respectively.
- 4.9 The percentage distribution of δ for each of 10 bins (-5° - 5° to 85° - 95° at equal intervals) for (a) (70W, 29.7-43.2N) (b) (60W, 29.7-45.2N) (c) (50W, 29.7-49.7N), (d) (40W, 29.7-49.7N) and (e) (30W, 29.7-49.7N). (f) As in (c), but for 91 different bins (-0.5° - 0.5° to 89.5° - 90.5° at equal intervals). The CNTL simulation is shown in red, whilst the SMTH is shown in black.
- 4.10 Histograms of (a) convective and (b) large-scale precipitation for the constant longitude domain (60W, 29.7-45.2N) across the twenty-year wintertime analysis period, for both the CNTL and SMTH experiments. Each bin is 1mm day^{-1} wide, and each histogram has a total of 228,480 data points.
- 4.11 Twenty-year wintertime mean in (a) convective precipitation and (c) large scale precipitation in the CNTL experiment. Mean contours of SST are shown in black. The average reduction in the SMTH experiment from the CNTL experiment is shown for the (b) convective precipitation and (d) large scale precipitation.

- 4.12 Angle between the mean SST gradients in the CNTL and SMTH experiments.
- 4.13 Average angle in wintertime between the frontal horizontal temperature gradient at 925hPa and the mean CNTL and mean SMTH SST gradients, for the regions where there is (a) an average reduction in large-scale precipitation in the SMTH experiment relative to the CNTL, and (b) an average increase in large-scale precipitation in the SMTH experiment relative to the CNTL. The broad dark blue areas represent the regions that are not under consideration in their respective plot.
- 4.14 Relative distribution across all days of vertical velocity at (a) 925hPa and (b) 500hPa for the constant longitude domain (70W, 29.7-43.2N) for the CNTL (red) and SMTH (black) experiments.
- 4.15 Relative distribution across all days of vertical velocity at 925hPa for the CNTL (red) and SMTH (black) experiments for the constant longitude domains (a) (70W, 29.7-43.2N) (b) (60W, 29.7-45.2N) (c) (50W, 29.7-49.7N), (d) (40W, 29.7-49.7N) and (e) (30W, 29.7-49.7N).
- 4.16 As in Figure 4.15, but for the vertical velocity at 500hPa.
- 4.17 As in Figure 4.15, but for the vertical velocity at 300hPa.
- 4.18 Twenty-year wintertime mean in (a) vertical velocity at 925hPa, (c) vertical velocity at 500hPa and (e) vertical velocity at 300hPa in the CNTL experiment. Mean contours of SST are shown in black.

The average reduction in the SMTH experiment from the CNTL experiment is shown for the vertical velocity at (b) 925hPa, (d) 500hPa and (f) 300hPa.

- 5.1 Schematic showing a cyclone passing over the Gulf Stream. A smoothing of the SST gradient, as in Minobe et al. (2008), reduces the convective available potential energy on the warm side of the Gulf Stream, resulting in the largest region of reduction in convective precipitation. Colocated with a broad area of the cold sector is a region of negative PV.
- 5.2 Correlation between the December-March North Atlantic Oscillation index and global surface temperature (SST is used over the oceans) (Marshall et al., 2001).

List of Tables

- 2.1 Errors between theoretical and LTM backward-trajectory output for an interpolation time step of 1 minute and initial potential temperature perturbations of 0.1K, 1K and 10K.
- 2.2 As in Table 2.1, but for LTM forward-trajectory output.
- 2.3 Percentages of trajectories on EEs and MEs that end up north and south of the 35.25° latitude line.
- 2.4 Table representing the average time spent in the MABL above the GS domain in our heat budget analysis, the number of trajectories that exit the GS domain through the boundary layer top, and the contribution of the conversion term to the r.h.s of the heat budget in Equation 2.40.

CHAPTER 1

INTRODUCTION

1.1 EARTH'S MERIDIONAL TEMPERATURE GRADIENT

A striking feature of atmospheric and oceanic motions is the occurrence of fluctuations with time-scales that are not directly related to the periodicities of solar heating. Furthermore, casual observations of the weather show these fluctuations occur erratically in time. This suggests that if the state of the flow is unstable with regards to small ‘eddies’ present in any real system, then the latter may amplify with time. Synoptic scale (approximately 1000km scale) transient eddies are one of the essential components of the tropospheric general circulation, transporting substantial moisture, heat and momentum meridionally. These synoptic eddies are now understood to arise from the release of potential energy stored in the pole-equator temperature gradient of the Earth. (The orientation and orbit of our planet result in more solar radiation incident at the equator than at the pole, causing such a meridional temperature gradient). This gradient is illustrated in Figure 1.1, taken from the European Centre for Medium Range Weather Forecasts (ECMWF) Re-analysis (ERA)-40 Atlas, which shows the annual mean of the zonal mean potential temperature for the period 1979-2001 (Källberg et al., 2005). The potential temperature is the temperature an air parcel would acquire if brought adiabatically to a pressure of 1000hPa.

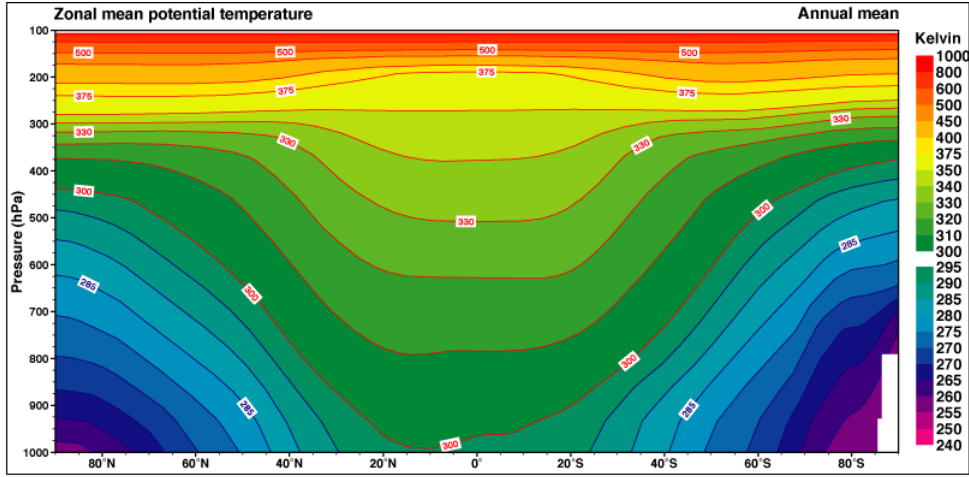


Figure 1.1: Annual mean of the zonal mean potential temperature in ERA-40 data, 1979-2001 (Källberg et al., 2005).

On a rapidly rotating planet, geostrophic and hydrostatic balance link the vertical shear of the wind to this gradient¹

$$\frac{\partial \theta}{\partial y} = -\frac{f \theta}{g} \frac{\partial u}{\partial z}, \quad (1.1)$$

where u is the zonal windspeed, θ is the potential temperature, f is the Coriolis parameter and g is the gravitational acceleration. The associated momentum transport is responsible for mid-latitude westerlies, organised into an eddy-driven “polar-front jet”; these resulting jet systems are referred to as *baroclinic* (e.g. Charney, 1947). Perturbations to these jets can draw from the large amount of potential energy stored within and convert it into eddy kinetic energy, rapidly growing into cyclones, which then propagate and mix warm air polewards and cold air equatorwards, acting to reduce the meridional temperature gradient (Bjerknes, 1919). The basic mechanism for this is called “baroclinic instability”, and the term “baroclinicity” used as a measure of how suitable

¹All symbols and physical constants are defined in Appendix A.

atmospheric conditions are for the amplification of such perturbations.

1.2 POTENTIAL VORTICITY

In the early 1930s, there did not yet exist a general statement about vorticity conservation that was satisfied for baroclinic flow in the atmosphere and ocean. However, in 1936, for hydrostatic shallow water equations, Rossby introduced a conservation of *potential vorticity*, PV, (a term coined in a later paper in which he extended to the stratified case), that was applicable in a baroclinic context (Rossby, 1936, 1940). The expression for PV was further generalised to a non-hydrostatic, continuously stratified fluid by Ertel (1942). The Ertel-Rossby PV is defined as

$$PV = \frac{1}{\rho} \zeta \cdot \nabla \theta, \quad (1.2)$$

where ρ is the density of air and ζ is the absolute vorticity (calculated relative to an inertial frame, and thus containing a term due to the Earth's rotation). Ertel's theorem then states that for frictionless, adiabatic fluid motion, the Lagrangian PV is conserved (i.e. $\frac{D(PV)}{Dt} = 0$). PV in the troposphere is typically small and positive, on the order of 10^{-7} to 10^{-6} K kg⁻¹ m² s⁻¹ = 0.1 to 1 PVU, driven by a positive vertical component of absolute vorticity from the Coriolis force ($\zeta_z \approx f \sim 10^{-4}$ s⁻¹), and a small increase in potential temperature with height ($\frac{\partial \theta}{\partial z} \sim 5 \times 10^{-3}$ K m⁻¹), whereas in the stratosphere, it is significantly higher ($\frac{\partial \theta}{\partial z} \sim 4.5 \times 10^{-2}$ K m⁻¹). The dynamic tropopause is based on PV, with isentropic surfaces making the transition from the troposphere to stratosphere usually featuring a sharp gradient in PV between the two air masses (Hoskins et al., 1985, Davis and Emanuel, 1991). The 1-3 PVU band lies in the transition zone of the weakly stratified upper troposphere and the relatively strongly

stratified lower stratosphere (Morgan and Nielsen-Gammon, 1998), and a single PV surface within this gradient can be used to define the tropopause.

In the 1940s and 50s, research into atmospheric PV continued (Reed and Sanders, 1953), however scientists were unable to use PV theory to explicitly show why cyclones formed near fronts, so PV analysis was disfavoured. However, a major review in the mid-1980s clarified why it is isentropic (not horizontal or isobaric) gradients and fluxes of PV that are dynamically significant (Hoskins et al. 1985). Another significant result to stem from this paper was the “invertibility principle” as applied to PV: given a global PV distribution under a suitable boundary condition (e.g. geostrophic balance), with complete boundary conditions, it is possible to diagnostically deduce all the other dynamical fields such as winds, potential temperatures and geopotential heights.

1.3 MID-LATITUDE CYCLOGENESIS

The process by which baroclinic instability leads to cyclone formation is demonstrated in Figure 1.2. Illustrated in Figure 1.2(a) is an initial southwards or downwards perturbation at the tropopause leading to an intrusion of stratospheric air into the tropopause, air which will have higher PV because of larger static stability (a measure of which is given by the Brunt-Väisälä frequency N , where $N^2 = \frac{g}{\theta} \frac{\partial \theta}{\partial z}$) than its surroundings. This positive PV anomaly will have a positive cyclonic circulation associated with it which, as a consequence of the invertibility principle, will extend throughout the troposphere, decaying in strength but still inducing weak cyclonic vorticity at the surface. This induced surface circulation transports warm air polewards and cold air equatorwards, deforming the surface meridional temperature gradient (Figure 1.2(b)). A warm temperature anomaly in the surface temperature field acts dynamically

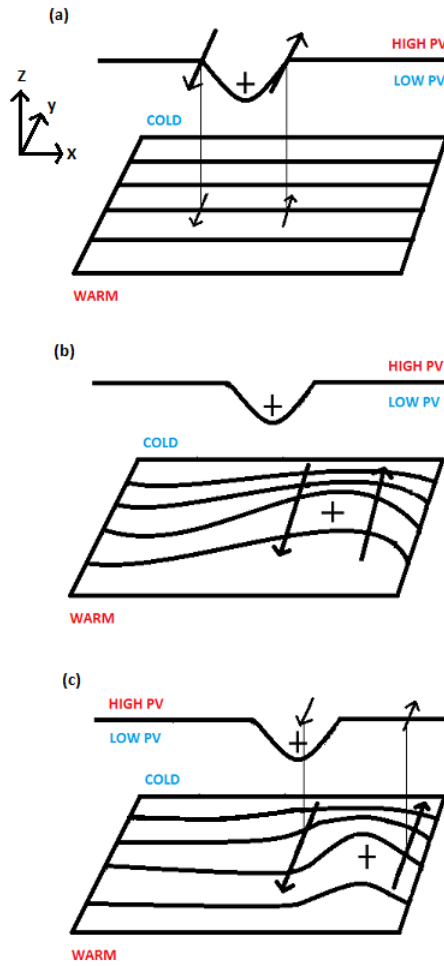


Figure 1.2: Schematic detailing how baroclinic instability leads to cyclone formation. Near-surface temperature contours are shown, as is the tropopause location, with positive PV anomalies indicated with a + and arrows denoting associated airflows. (a) A PV anomaly at the tropopause induces weak cyclonic vorticity at the surface. (b) This induced vorticity distorts the surface meridional temperature gradient. (c) This surface vorticity now feeds back to the tropopause.

as a positive PV anomaly located below the surface (Bretherton, 1966), and this anomaly will therefore have increased static stability and an associated cyclonic circulation. This surface vorticity will create a weak circulation anomaly at the tropopause (Figure 1.2(c)), and in this manner it is possible for the induced surface PV anomaly to feedback and intensify the initial perturbation. Baroclinic instability is the process by which the anomalies at the surface and the tropopause become phase-locked, and mutually intensify each other to form a baroclinic wave. The surface warm (cold) anomaly, with its cyclonic (anti-cyclonic) circulation associated with it, forms the low (high)-pressure part of the wave.

Pioneering papers by Eady (1949) and Charney (1947) fit a mathematical framework to baroclinic instability and demonstrated that the cyclonic growth rate is proportional to the meridional temperature gradient. Eady's model of baroclinic instability will be discussed further in Chapter 2.

1.4 MID-LATITUDE STORM TRACKS

The term "storm-track" often refers to (Eulerian) areas of high wind or high tropospheric geopotential height variability at synoptic time scales (roughly 1-7 days), and can be considered a synoptic indicator of storm activity. Indeed, these storm tracks can be related directly to baroclinic waves (Wallace et al., 1988). Such concentrated regions of eddy activity reach a maximum over the mid-latitude oceans in both the Northern and Southern Hemisphere (NH and SH respectively) (Blackmon et al., 1977, Trenberth, 1981, Hoskins et al., 1983). In wintertime, the zonal storm-track average is broadly similar between the NH and SH, bearing in mind the NH has stronger regional structure. In summertime however, the NH storm track weakens in activity and shifts poleward, whereas

the activity in the SH persists, becoming more concentrated in latitude and shifting slightly equatorwards (Trenberth, 1991).

In NH wintertime, the main storm tracks extend from the east coasts of North America and Asia across the Atlantic and Pacific oceans respectively. A summary of some of the features of these NH storm tracks is shown in Figure 1.3, taken from Hoskins and Valdes (1990), for six winters of ECMWF data (December-February, DJF, 1979-84). Upstream of the two regions of maximum synoptic time scale height-field variance are maxima of poleward and upward heat flux by these systems. The vector $(\overline{v'^2 - u'^2}, \overline{-u'v'})$ is indicated at 250hPa, and where these arrows diverge there is a tendency to force the mean westerly flow. Also indicated are the regions, poleward of 20°N, of maximum column-averaged diabatic heating.

Calculations by Simmons and Hoskins (1979) show that at mid-latitudes a packet of baroclinic wave activity leaves behind a region of low-level baroclinicity, with the potential temperature contours pushed far to the north and south. It is therefore curious that such mid-latitude storm-tracks are persistent, rather than constantly changing latitude. Hoskins and Valdes (1990) confirm that the direct thermal effect of eddies indeed acts against such storm-track existence. However, they find that land-sea differences off the east coasts and indirect eddy-induced mean diabatic heating in the storm-track region act to maintain the mean maximum in baroclinicity, suggesting a possible system of self-maintenance. Although the first to invoke this baroclinic response to the land-sea contrast, they were unable to convincingly show a role for ocean currents.

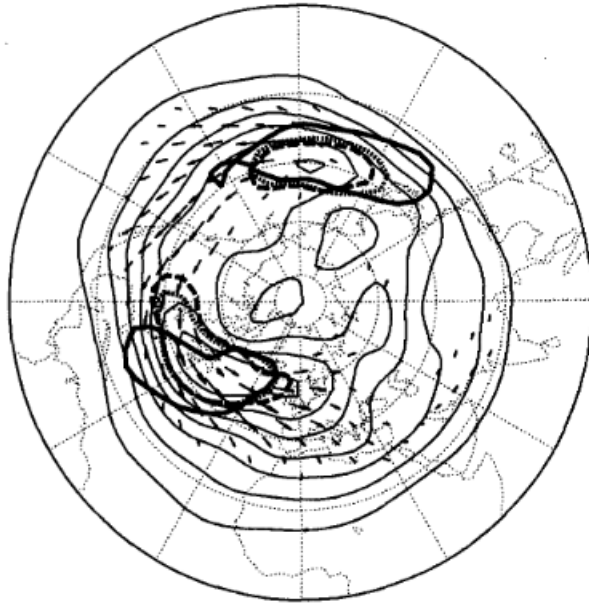


Figure 1.3: NH winter storm track structure based on high-pass time-filtered transients in ECMWF data for DJF 1979-84. The thin contours are of height variance (contour interval 15m^2) and arrows indicate the vector $(\overline{v'^2 - u'^2}, -\overline{u'v'})$, both at 250hPa. Also shown are single contours of the 700hPa horizontal temperature flux (thick dashed contour at 10 K m s^{-1}), 700hPa vertical temperature flux (thick dotted contour at 0.2 K Pa s^{-1}), and the column mean diabatic heating (thick solid contour at 50 W m^{-2}). (Hoskins and Valdes, 1990).

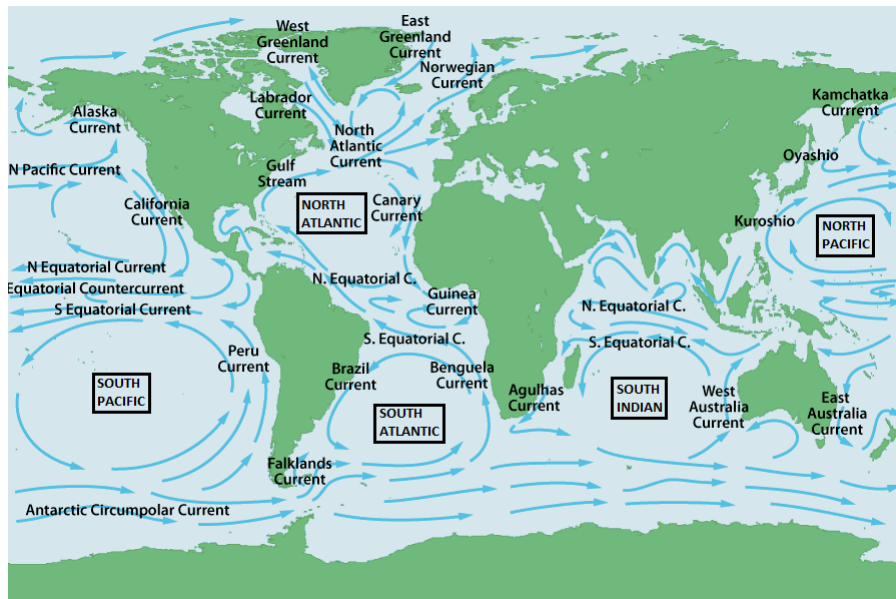


Figure 1.4: Diagram of the five major ocean gyres (boxed). Major ocean currents are marked by arrows and annotated. Figure courtesy of the National Oceanography Centre.

1.5 WESTERN BOUNDARY CURRENTS AND AIR-SEA INTERACTIONS

On a broad general scale, the Earth’s rotation results in five major systems of rotating ocean currents called gyres: North Atlantic (NA), North Pacific (NP), South Atlantic (SA), South Pacific (SP) and South Indian (SI). Each of these subtropical gyres is flanked by Western and Eastern Boundary Currents (WBCs/EBCs). In general, WBCs (EBCs) are warm (cool), as they transport water from equatorial (polar) regions. WBCs are narrower, faster and deeper than their eastern counterparts due to “western intensification” (Stommel, 1948). A simple interpretation of this intensification is that the centre of the gyre is slightly offset due to the increasing strength of the Coriolis effect as one moves

poleward. The WBC systems are called the Gulf Stream (GS) in the NA, the Kuroshio Extension in the NP, the Brazil Current in the SA, the East Australian Current in the SP and the Agulhas Current in the SI. The currents in the SH are weaker than those in the NH, partly because WBCs require extended land barriers that are generally absent in the SH. These major ocean currents are depicted in Figure 1.4, from the National Oceanography Centre, with the five major ocean gyres additionally annotated. The heat transport of strong ocean currents like the WBCs act to confine sharp sea-surface temperature (SST) gradients into narrow frontal zones.

Prior to Hoskins and Valdes (1990) invoking the baroclinic response to the land-sea contrast, local ocean-atmospheric forcing over the WBCs had nonetheless already been long documented (e.g. Bjerknes, 1964). Sweet et al. (1981) noted that SST fronts such as the GS modify the shear in the lower-atmosphere wind profile, causing changes in the boundary layer height. Calm seas and surface winds were found over the cold regions of the GS, with increased sea state and strong winds found on the warmer flank. Wallace et al. (1989) attributed these effects to the coupling of surface winds with free-troposphere winds, the coupling itself due to the instability of the boundary layer. Yet up until the late nineties, the search for oceanic feedback into the atmosphere had not yet produced any conclusive evidence in the extra-tropics. However, with the launch of satellites designed specifically to measure near-surface wind vectors (e.g. NSCAT, 1996, QuikSCAT, 1999), extensive research was produced which highlighted very clearly the importance of oceanic currents for mid-latitude weather systems. With satellite measurements, solid covariability in SST and surface wind speed over WBCs was found, with increased (reduced) wind speeds associated with warm (cold) SST anomalies (Chelton et al., 2004, Nonaka and Xie, 2003). The frequency of high wind events is also notably

modulated by the SST fronts and their meanders (Sampe and Xie, 2007). Indeed, positive SST-wind correlation results from a vertical shear adjustment mechanism - an increase in SST reduces the static stability of the atmosphere, intensifying vertical turbulence mixing and bringing fast-moving air from aloft down to the sea surface (Booth et al., 2010). It is this momentum-mixing mechanism that explains why surface storm track maxima occur on the western side of the ocean basins, even though the mean winds are strongest near the centre where the transient eddy fluxes are largest. During non-storm conditions also, locally thermally forced perturbations near the GS SST frontal region are the dominant modifier of cross-frontal winds (Song et al., 2006).

Additional studies of storm-tracks over WBCs have also suggested that individual synoptic weather systems are modified and often enhanced when they pass over the strong SST gradients (e.g. Sanders 1986), with large cyclonic growth rates and cyclogenesis densities shown over the WBCs (Hoskins and Hodges, 2002). Indeed, rapidly growing synoptic storms (“bombs”) have been shown to intensify and track along WBCs (e.g. Colucci, 1976, Chen et al. 1992). For example, in a study of winter cyclones off the east coast of the Carolinas, Cione et al. (1993) observed that 85% of strong storms intensified within a narrow highly baroclinic region, and that these intense events were characterized by smaller Gulf Stream Front-to-land distances; the decreasing distance between the GS and the coastline producing an increased baroclinic marine atmospheric boundary layer (MABL). It is this enhancement of low-level baroclinicity by SST gradients that is likely crucial to the increased eddy activity (Nakamura and Shimpo, 2004, Nakamura et al., 2004).

In addition to the influence of baroclinicity, oceanic fronts affect the diabatic heating of the atmosphere via turbulent surface heat fluxes, with differential heating at the surface affecting atmosphere front strength (e.g. Persson et al,

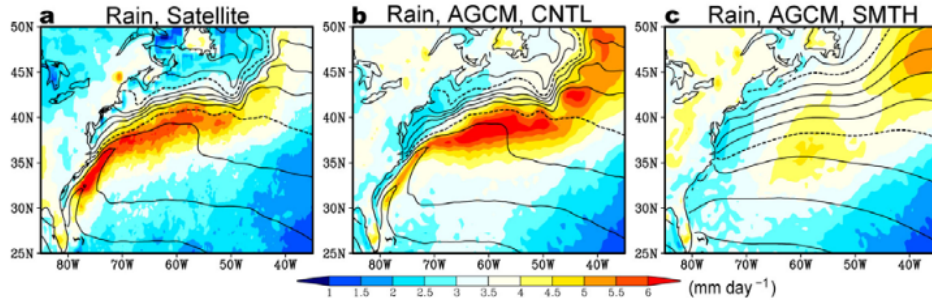


Figure 1.5: Annual climatology of rain rate: (a) observed by satellites, and in the AFES with (b) observed and (c) smoothed SSTs. Contours of SST are also shown at 2°C intervals, with dashed contours for 10°C and 20°C (Minobe et al., 2008).

2008, Giordani and Caniaux, 2001). Atmospheric diabatic heating can also cause potential vorticity anomalies (Stoelinga, 1996), as well as induce upper-level mass flux divergences that enhance storms and destabilize the atmosphere (Businger et al., 2005). These differential surface sensible heat fluxes caused by air flowing across sharp SST gradients have also been suggested as a possible system of baroclinicity maintenance against eroding eddy-heat fluxes (“oceanic baroclinic adjustment”, Nakamura et al., 2008).

Recently, the deep influence of WBCs in the troposphere has been well established (Liu et al., 2007, Tokinaga et al., 2009, Kobashi et al., 2008). For example, in a paper by Minobe et al. (2008), high resolution operational analyses from the ECMWF are used to convincingly show that the GS in fact directly affects the entire troposphere, from the surface all the way up to the tropopause, in a systematic manner. On a climatic timescale, it has been hypothesized that relatively low (high) pressures on the warm (cold) flank of the GS front induces wind convergence (divergence) that anchors upward motion (up to heights of 300hPa). This would then enhance precipitation locally, providing diabatic heating to the atmosphere. High instability of the atmosphere as manifested in enhanced ocean-atmosphere latent and sensible heat flux leads

to deep convection, enabling the influence of the warm ocean current to reach the entire troposphere, with upper-tropospheric divergence showing a banded structure similar to the surface convergence and precipitation patterns. However, when the GS SST gradient is smoothed, the observed patterns in surface precipitation disappear, as illustrated in Figure 1.5, from Minobe et al. (2008). Observed- (b) and smoothed- (c) SST simulations are performed using the Atmospheric General Circulation Model For the Earth Simulator (AFES), and are compared with satellite observations from the Tropical Rainfall Measuring Mission (a), from January 2002 - February 2006. This underlines the significance of the oceanic SST gradient in the air-sea interaction over the WBCs. Smoothing such an SST gradient also reduces the mean and variance of surface heat fluxes, as well as storm-track activity in the atmosphere (Taguchi et al., 2009, Nakamura et al., 2008).

1.6 OCEAN-ATMOSPHERE TURBULENT HEAT FLUXES

Figure 1.6, from Trenberth and Caron (2001), shows estimates of the atmospheric and oceanic heat transport, required by top-of-atmosphere radiation, based on National Centers for Environmental Prediction (NCEP) reanalyses and Earth Radiation Budget Experiment (ERBE) data. From the equator to 17° , the poleward ocean transport exceeds that of the atmosphere. However, by 35° latitude, the poleward atmospheric transport accounts for 78% (92%) of the total transport in the NH (SH). Over the ocean, the strongest surface heat fluxes are located in NH wintertime over the WBCs (Yu and Weller, 2007). This is due to the temperature contrast of cold continental air interacting with the relatively warm ocean. Analogous mean surface heat flux peaks exist in SH wintertime, but these are not as strong. At mid-latitudes, these areas of intense ocean-atmosphere heat exchange suggest the presence of an ocean-atmosphere

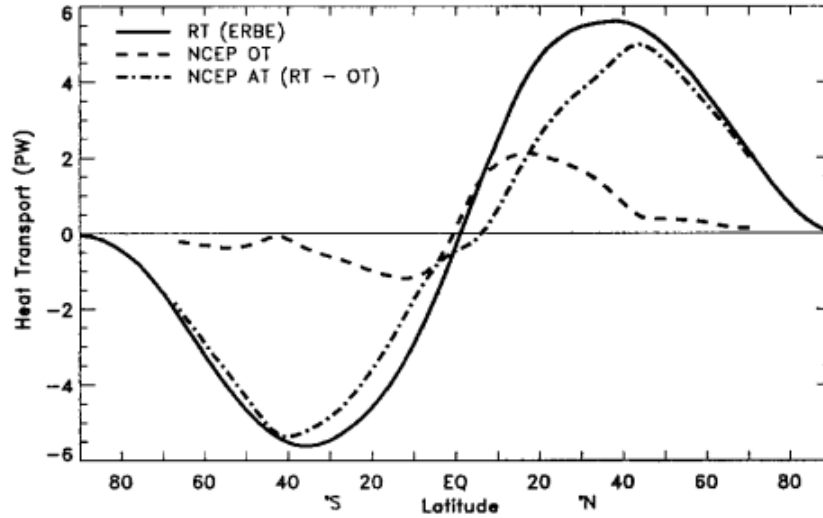


Figure 1.6: The required total heat transport from the top-of-atmosphere radiation (RT) is compared with the derived estimate of the adjusted ocean heat transport (OT) and implied atmospheric transport (AT) (Trenberth and Caron, 2001).

“relay”, whereby the ocean loses a lot of heat to the atmosphere, which then continues to transport it poleward.

Intraseasonal variability of surface heat fluxes over WBCs is a subject of much recent research (Konda et al., 2010, Grodsky et al., 2009). In wintertime, it is found that these turbulent heat fluxes are remarkably variable, with high latent and sensible heat fluxes coinciding in discrete high-flux “events”, each lasting approximately 2-3 days. Additionally, these high-flux events account for a significant proportion of the total wintertime heat flux in the region. On these days northerly flow brings cold dry descending continental air over the warm waters in the WBC region, (over the GS for example, this is forced by westerly flow over the Rocky Mountains producing a downstream north-south standing wave), resulting in the high turbulent heat fluxes and ventilation of the MABL. Clear cyclonic structure is present on heat flux event days over WBCs, with

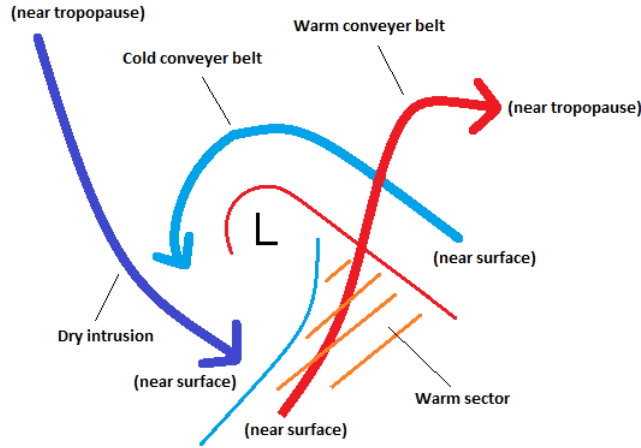


Figure 1.7: Schematic illustrating the frontal structure and airflows within a mid-latitude cyclone. The cold and warm fronts are denoted by the blue and red lines respectively. The three main airflows are shown by arrows, along with an indication of their inflow and outflow levels. The cold conveyer belt remains near the surface throughout.

circulation anomalies that extend throughout the troposphere (Shaman et al, 2010, Alexander and Scott, 1997).

1.7 EXTRATROPICAL CYCLONE STRUCTURE

One of the first conceptual models of extratropical cyclones and the structure of their cloud and precipitation distribution was the Norwegian cyclone model (Bjerknes and Solberg, 1922), which emphasized the continuous role of pre-existing surface fronts to occlusion. With the development of modern remote sensing techniques however, Shapiro and Keyser (1990) suggested an alternative. They argued that continuous frontal deformation in fact rarely occurs, and that there is instead a front “fracture” near the cyclone centre, with the cold front becoming disjointed from the warm front. A schematic of this is shown in Figure

1.7. The cold front becomes perpendicular to the warm front, and there is an extension to the warm front that wraps around the low centre. As a cyclone matures, warm air often becomes encircled by the warm front and trapped in a “warm seclusion”.

Also shown in Figure 1.7 are the three distinct airstreams associated with extratropical cyclones, diagnosed by isentropic analyses of the airflows moving with them. The first of these is the cold conveyer belt (CCB), originating in the cold air ahead of the warm front (Carlson, 1980). The CCB is a low-level airstream that flows westwards relative to the cyclone centre, turning cyclonically around the low centre. It is noted that if moisture is precipitated into it from above, it is also possible for the CCB to become buoyant, ascend and turn anticyclonically.

The second of these is the dry intrusion (Reed and Danielsen, 1959), whose airflow can be identified as an ensemble of trajectories characterized by maximum descent (Wernli, 1997). These trajectories originate from the vicinity of a newly developing tropopause fold, a manifestation of upper-level forcing of cyclogenesis associated with a positive upper-level PV anomaly. As a result, this airflow has extremely low moisture content and is an area of often completely cloud-free air immediately behind the cold front. Clouds can be formed further behind the cold front (e.g. in a cold air outbreak, where cold northerly continental air flows rapidly over the warmer sea surface further behind the cold front). These clouds are shallow, restricted by the much drier air in the dry intrusion above (Browning, 1986).

The final airstream is the main poleward airflow, the warm conveyer belt (WCB, Green et al., 1966, Harrold 1973), which is responsible for most of the cyclone’s meridional energy transport, in terms of both latent and sensible heat, and whose inflow region is strongly influenced by surface forcings, particularly

SSTs above the zonal average (Eckhardt et al., 2004). WCBs originate in the warm sector and are strongly ascending moist airstreams that quickly rise from the boundary layer to the upper troposphere, typically travelling poleward and eastward during the first two days and then turning equatorward in the outflow. Due to this rapid ascent to the upper troposphere, WCBs influence chemical composition in the free troposphere (e.g. Arnold et al., 1997), and on the time scale of a few days transport air pollution from one continent to the other (Stohl et al., 2002).

Indeed, WCBs are the dominant advective transport mechanism for boundary-layer ventilation into the free troposphere (Sinclair et al., 2008), and can ventilate out huge amounts of water vapour (Boutle et al., 2011). In fact, WCBs are usually saturated and play a highly significant role in the cyclone-associated surface precipitation (Browning, 1990), as they are approximately 100% efficient at converting moisture into precipitation (Eckhardt et al., 2004). Furthermore, WCBs have an occurrence frequency of mostly less than 10% and thus are not very abundant features, and yet are still responsible for a huge percentage of the total precipitation in many regions (Pfahl et al., 2013).

WCBs are also highly relevant dynamically and have a strong influence on tropospheric PV-distribution. Condensation is very pronounced in WCB flows, and associated latent heat release leads to cross-isentropic airflow and the creation and destruction of PV (Haynes and McIntyre, 1987). Indeed, diabatic PV changes along WCBs generate positive PV anomalies at low-levels, important for the evolution of the cyclone, and strong negative anomalies at the tropopause, which can have a strong impact on the downstream flow evolution (Massacand et al., 2001, Madonna et al., 2013). Such a positive PV anomaly below the heating should enhance the circulation of the lower boundary wave discussed in Section 1.3, whilst the negative anomaly would erode the PV ahead of the

upper-level trough. Indeed, in this way, both these effects suggest that increased moisture should intensify cyclogenesis.

1.8 THESIS OUTLINE

In terms of ocean-atmosphere interaction, a clear connection exists between WBCs, synoptic scale storm activity in these areas and subsequent atmospheric motions, whereby it has been shown each can have a substantial effect on the other. However, the mechanisms whereby WBCs affect the climate on monthly and longer timescales remain poorly understood - what is responsible for the significant influence of the strong oceanic frontal zones on the overlying mean tropospheric state? As aforementioned, WBCs are intense regions of synoptic activity, closely connected to highly variable extremes in ocean-atmosphere heat exchange. The overall aim of this thesis is to assess the differences between days of average and extreme air-sea heat flux over the WBCs, to assess the extent to which the most extreme air-sea heat flux events over the WBCs shape the climatological mean over these areas, and in doing so to further understanding of the air-sea interaction over the WBCs. This aim will be broken down into three chapters.

Chapter 2. The aim of this chapter is to understand what differences are present in the direct air-sea interaction on these extreme heat flux events compared with an average day. The focus of this chapter will be on the wintertime GS extension. Firstly, a (Lagrangian) trajectory model is constructed and both tested theoretically with the Eady model and verified against known trajectory calculations of WCBs. Initially, the model is used to differentiate the origins of the air parcels over the GS between days of extreme and median heat flux

and classify these trajectories. Then, the differences in the boundary layer heat budget between these days will be addressed, by comparing the ocean-atmosphere heat input with that advected away by the trajectories. The role of different processes on these days is subsequently discussed.

Chapter 3. Firstly in this chapter, the variation of the ocean-atmosphere heat exchange with initial atmospheric state is considered - given a value of surface heat flux, what atmospheric conditions do we expect to find causing it? Having ascertained this relationship, the focus is then on understanding the extent to which different subsets of the heat flux affect the mean wintertime atmospheric state. In particular, attention is directed towards the mean patterns in tropospheric wind divergence and precipitation. Finally, given the results of the chapter, a potential explanation is offered for understanding the strong influence of the sharp SST gradients of the GS on the mean wintertime pattern in precipitation.

Chapter 4. The relationship between the SST gradient and atmospheric fronts over the GS is explored in this chapter. Does a smoothing of the SST gradient result in a damping of the atmospheric fronts? If so, what is the extent of the damping and is there a dependence on initial front strength or location over the GS? The significance of the angle between atmospheric fronts and the SST gradient is assessed and the question of whether the SST gradient affects the direction of frontal propagation is considered. The corresponding effect on associated atmospheric variables such as vertical velocity and precipitation is also examined.

The data used in Chapters 2 and 3 is ECMWF Interim Reanalysis data (ERA Interim) (Berrisford et al., 2009), whilst in Chapter 4, the data is from the Atmospheric General Circulation Model for the Earth Simulator (AFES; Ohfuchi et al., 2004) version 2 (Enomoto et al., 2008). These datasets are discussed in more detail in the individual chapters.

CHAPTER 2

A LAGRANGIAN VIEW OF AIR-SEA INTERACTIONS OVER THE GULF STREAM

2.1 INTRODUCTION

The strong relationship between anomalies of turbulent ocean-atmosphere heat fluxes at mid-latitudes and anomalies in atmospheric circulation has been extensively documented at various timescales (e.g. monthly - Cayan, 1992, Deser and Timlin, 1997). However, accurate examination of the air-sea exchange and the mechanisms of their coupled interaction in the areas of the WBCs necessitates analysis on synoptic timescales, as it is the highly variable surface heat flux, as opposed to the mean flux field, that forms the actual signal at the air-sea interface. The focus of this chapter is on the wintertime GS extension, which along with the adjacent waters of the northwestern portion of the subtropical gyre is where the strongest average air-sea heat fluxes occur globally (Esbensen and Kushnir, 1981, Josey et al., 1999).

Over the GS, recent analysis demonstrates that the synoptic patterns of heat fluxes are associated with synoptic atmospheric transients propagating over it (Zolina and Gulev, 2003). In fact, synoptic storms are responsible for a large fraction of total seasonal heat fluxes in the region. Over the last 60 years, an increase in the number of these high-flux events has caused increased heat fluxes

over the GS, with increasing long-term trends in the eddy heat flux and low-level baroclinicity associated with them (Shaman et al., 2010). Given that there is a significant switch in the relative importance of poleward heat transport from the ocean to the atmosphere at mid-latitudes, as discussed in Section 1.6, it is essential to understand the nature and the extent of these discrete events of extreme air-sea heat transfer and how the underlying processes differ from the average day.

In this chapter, an attempt is made to classify and quantify the main differences in the direct air-sea heat exchange between days of extreme surface heat flux over the GS and days of average heat flux. This is accomplished by analysing atmospheric trajectories on both sets of days, using a custom built Lagrangian trajectory model. Section 2.2 defines our GS domain of interest and our associated index of air-sea heat flux. In Section 2.3, the Lagrangian trajectory model we will be using is described, including model error analysis. In Section 2.4, we analyse trajectories on days of extreme and average heat flux over our GS domain, and classify and quantify the differences. Section 2.5 considers the differences in the overlying atmospheric heat budget on days of extreme and average heat flux, and a summary is presented in Section 2.6.

2.2 GULF STREAM HEAT FLUX INDEX

2.2.1 HEAT FLUX DATASET

The dataset used to examine surface heat fluxes in this thesis will be ECMWF Interim Reanalysis data (ERA Interim) (Berrisford et al., 2009). The ERA-Interim reanalysis utilises a 4D-var data assimilation system to incorporate observations over a 12-hour reanalysis period, with forecasts starting at 00:00UTC (Coordinated Universal Time) and 12:00UTC, with spectral resolution T255

($\sim 0.7^\circ$). Surface latent heat fluxes (LHF) and sensible heat fluxes (SHF) are computed from bulk aerodynamic formulas, in terms of differences between parameters at the first model level above the surface, at a given height z_n , and those at the surface:

$$SHF = \rho C_H |U_n| (s_{surf} - s_n), \quad (2.1)$$

$$LHF = \rho C_Q |U_n| (\alpha_{surf} q_{sat} - \alpha_n q_n), \quad (2.2)$$

where the subscript *surf* denotes values at the surface, $s = c_p T + gz$ is the dry static energy, T is the air temperature, c_p is the specific heat capacity of air at constant pressure, C_H and C_Q are transfer exchange coefficients, $|U_n|$ is the wind speed, which includes a free convection parameter, q_n is the specific humidity, $q_{sat}(s_{surf})$ is the saturation specific humidity, and α_n and α_{surf} are land-dependent factors (over water, $\alpha_n = 1$ and $\alpha_{surf} = 1$) (ECMWF IFS documentation IV).

Both the sensible and latent surface heat fluxes are not analysed fields, and are consequently taken from short-range forecast accumulations produced from forecasts beginning at 00:00 and 12:00UTC. Such accumulated forecast fields are affected by spin-up, i.e. they vary with forecast length. This is due to the fact that surface fluxes strongly depend on imbalances between the initial conditions and the atmosphere consistent with the forecast model's physics and dynamics (White and Saha, 1999). However, 12-month running means of the globally-averaged surface sensible and latent heat fluxes in ERA-Interim only exhibit up to around 1Wm^{-2} between forecasts taken with length 0h-12h and those with 24h-36h (Källberg, 2011). This figure represents only about 5% (1%) of the globally-averaged surface sensible (latent) heat flux. In addition, a 20-year

average (1989-2008) of the difference in net surface energy flux (i.e. incl. surface solar and thermal radiation) from forecasts 24h-36h and 00h-12h is shown to be roughly 10Wm^{-2} over the GS region. This is a relatively small fraction compared to the range of daily surface heat fluxes over the GS (e.g. Shaman et al., 2010), and spin-up should not cause any relevant error in the present analysis. In this chapter, observations from 12:00UTC are used to initialize 3 hour time-step forecast simulations. Accumulated surface sensible and latent heat fluxes are then projected onto a longitude-latitude grid of resolution $1.5^\circ \times 1.5^\circ$. Dividing by the time step then yields the average value of the heat fluxes between the start of the forecast and the forecast step, i.e. between 12:00 and 15:00 UTC.

It should be noted that some unavoidable error does exist between surface heat fluxes from ECMWF reanalyses compared with buoy measurements. However, buoy measurements are not widely available over the timescales required for this study, and ECMWF reanalyses is on the same order of error as other reanalyses such as those from NCEP-National Center for Atmospheric Research (Josey et al., 2001).

2.2.2 GULF STREAM HEAT FLUX DOMAIN

The period of analysis in this study will be thirty-three years, December-February (DJF) 1979-2011. For the purposes of defining a GS heat flux index, the average value of the heat flux between 12:00 and 15:00 UTC on a particular day, as discussed in the previous section, will be considered for now to be the “daily” heat flux. It is noted here that the mean diurnal cycle in both sensible and latent heat flux over the GS is known to be relatively small ($\sim 10\text{Wm}^{-2}$, Clayson et al., SeaFlux Version 1 Documentation). Indeed, this suggests that an average between 12:00UTC and 15:00UTC is sufficiently representative of the whole day. In this chapter, we will use the convention that positive (negative) surface heat

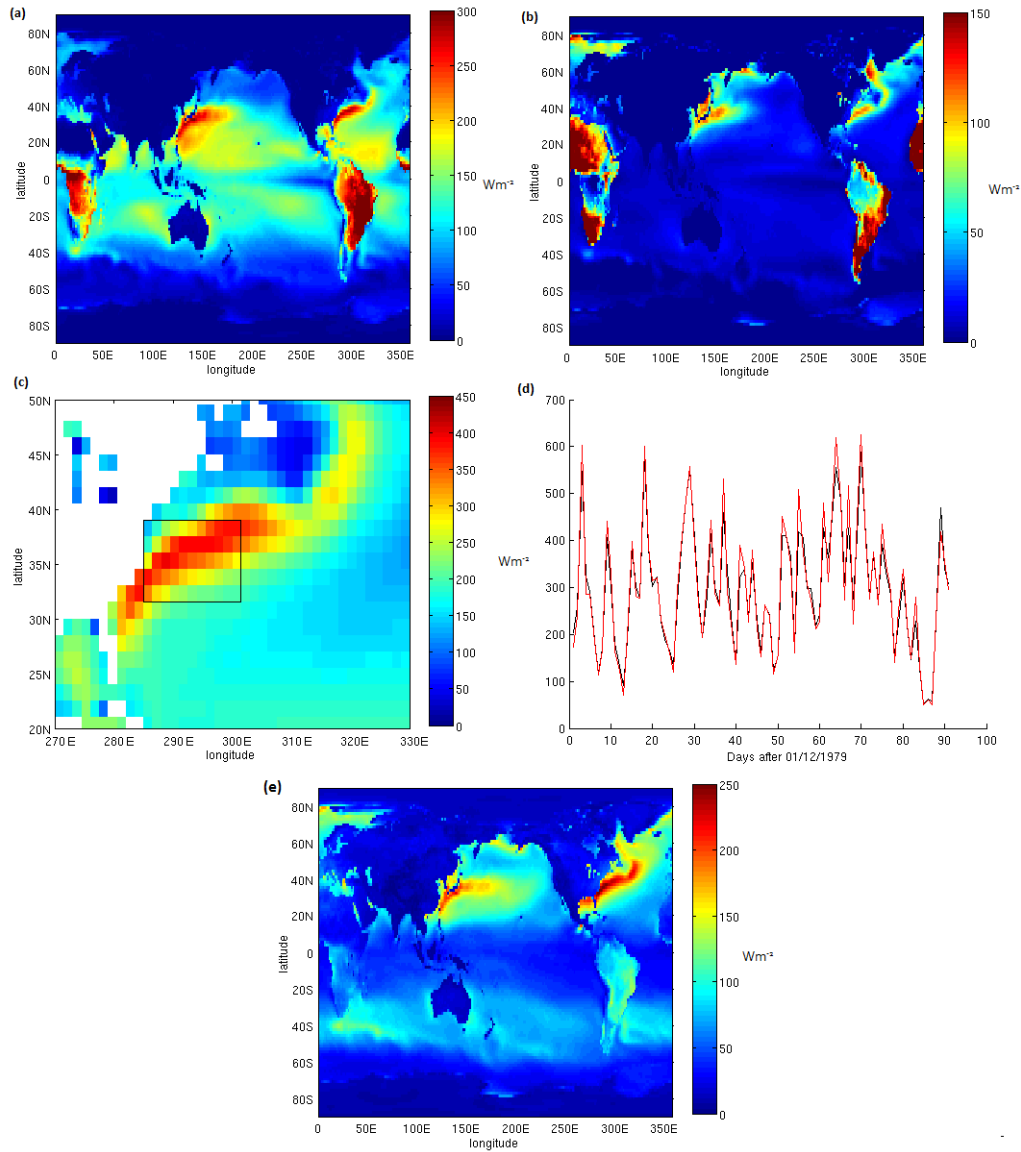


Figure 2.1: Wintertime (DJF) heat flux data 1979-2011. (a) Average global surface latent heat flux. (b) Average global surface sensible heat flux. (c) Total (latent and sensible) surface heat flux over the Gulf Stream. Land is illustrated in white. The rectangular box shown is the Gulf Stream Domain used in this Chapter. (d) GS domain-averaged total heat flux for DJF 1979 calculated in red as the average between 12:00 and 15:00UTC and in black as the average across the whole day. (e) The standard deviation of the average total daily heat flux. All figures are in Wm^{-2} .

fluxes are directed into the atmosphere (ocean). Figures 2.1(a) and (b) illustrate the thirty-three year DJF averages of the latent and surface sensible daily heat fluxes globally. For both of these plots, the scale has been restricted to show only positive surface heat fluxes. Whilst in certain locations, both the mean latent and sensible heat flux are in fact negative, the overwhelming majority of these regions are over the continents. Here, we are concerned with the turbulent heat exchange between the ocean and the atmosphere. Indeed, in Figure 2.1(c), the thirty-three year DJF average of the total (the sum of the latent and sensible) daily heat flux is shown in the GS area. Over the ocean in the GS region, both the mean ocean-atmosphere latent and sensible heat fluxes are positive everywhere. Also shown is the rectangular domain (285° - 301.5° , 31.5° - 39°) defined in this study as the “Gulf Stream Heat Flux Domain”, chosen to be representative of the maximum average total heat flux in the region. Figure 2.4(d) shows the GS domain-averaged total “daily” heat flux, as defined previously as the average value between 12:00 and 15:00UTC, for the winter season starting on 1 December 1979 (91 days) in red. Also shown in black is the GS domain-averaged total heat flux for the same season, but each day the total heat flux is instead computed as an average across the entire day (calculated from the average of two 12-hour accumulated forecasts from 00:00UTC and 12:00UTC on that day). Both graphs show an extremely high degree of similarity, validating our earlier assertion that the average value of the total heat flux between 12:00 and 15:00UTC is representative of the whole day.

The standard deviation of the total daily heat flux in the GS area is shown in Figure 2.1(e). As discussed in Section 1.6, heat fluxes in this region are highly variable, and strong ocean-atmosphere heat transfer is associated with overlying synoptic storm activity. The structure of an extra-tropical cyclone was examined in Section 1.7. Within the WCB region, air that is moist and warm

can pass over a cooler sea surface, losing heat and becoming super-saturated with respect to the surface, forcing moisture to condense out. Here, there can potentially be negative fluxes of both sensible and latent heat. Positive heat fluxes generally occur behind the cold front of the cyclone, extending towards the high pressure part of the associated baroclinic wave (Sinclair et al., 2010). Figures 2.1(a) and (b) show that averaging over an extended period of time results in the collocation of the maximum means in latent and sensible heat flux.

Within a baroclinic wave however, whilst latent and sensible heat fluxes are highly correlated, their maximum values do not have to be entirely coincident (Boutle et al., 2010). The greatest thermal advection of cold air over the warm sea-surface is to the east of the trailing high centre, giving the largest contrast in temperature, and hence the greatest sensible heat-flux occurs here. However, the largest saturation deficit occurs to the south of the high centre where the air temperature and SSTs are higher, leading to a higher saturation vapour pressure, and hence the largest latent heat fluxes occur here. (There is however a secondary maximum in both sensible and latent heat fluxes to the south west of the low centre, caused by the low-level jet wrapping around the cyclone centre increasing wind speeds in this region).

In this chapter, we are concerned with the differences between individual events of extreme air-sea heat flux and days with average heat flux, including analysis of atmospheric trajectories on these days. Although the GS domain is large enough to incorporate different areas of a baroclinic wave, it is nonetheless important to have as accurate an idea as possible what aspect of such a wave we could be using to define our extreme heat flux events. For this reason, a thirty-three year Gulf Stream Index (GSI) is defined, ranking the 2979 DJF days between 1979 and 2011 by their GS domain averaged latent, as opposed

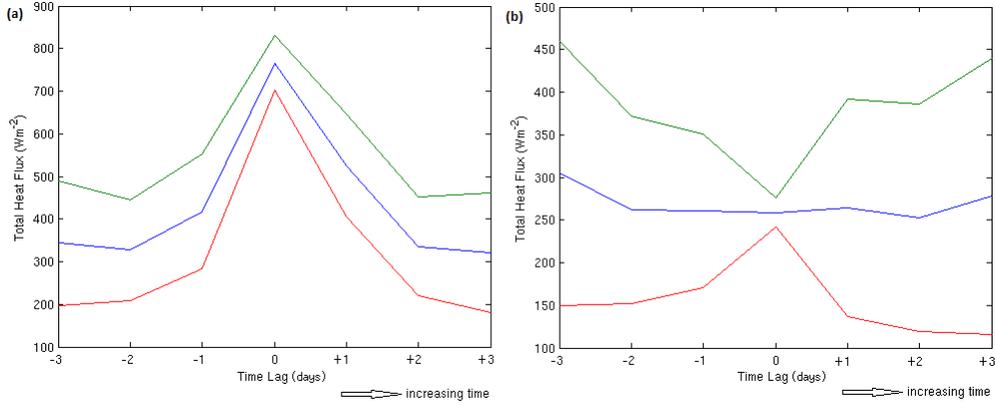


Figure 2.2: In blue: GS domain-averaged total daily latent heat flux, averaged across (a) EEs and (b) MEs with a time lag of ± 3 d. The green and red lines represent \pm one standard deviation in the heat flux across each set of days.

to total, daily heat flux.

Across the GS domain, the average daily latent heat flux in our GSI is 213.43Wm^{-2} . In this chapter, we will examine the differences between the most extreme 1% of latent heat flux events in the GSI (EEs), and the median 1% of latent heat flux events (MEs). Figure 2.2 illustrates the GS domain averaged total heat fluxes for EEs and MEs, averaged across their thirty days with a time-lag of ± 3 days. Also shown is one standard deviation difference in the heat flux across each set of days. The discrete nature of the extreme heat flux events is clear, with a consistently sharp spike at zero lag. For MEs however, there is no analogous spike, and the standard deviations are relatively large, indicating there is no discernible pre- or post-conditions for these.

2.3 THE LAGRANGIAN TRAJECTORY MODEL

2.3.1 INITIAL DEVELOPMENT

In order to classify the origin, destination and physical properties of the airstreams over the GS domain on EEs and MEs, it is necessary to analyse the individual trajectories on these days. Such analysis requires a trajectory model; unfortunately, these are not widely available for general use. The British Atmospheric Data Centre (BADC) offers an online trajectory service that can be used to calculate forward and backward trajectories from a variety of ECMWF data sources at 1.125° or 2.5° horizontal resolution. However, it is not currently possible to use ERA-Interim reanalysis data at the higher 0.7° horizontal resolution, nor is it possible to track all the physical variables associated with the trajectories. To this end, a Lagrangian Trajectory Model (LTM) was developed in MATLAB.

As aforementioned, the LTM is intended to analyse ERA-Interim reanalysis data, of 0.7° horizontal resolution and 37 pressure levels, available every six hours. The data was to be input directly into the code in order to track parcel locations, forwards and backwards, at successive intervals from the initial position. Any trajectory is to be calculated via

$$\mathbf{x}(t + \Delta t) = \mathbf{x}(t) + \mathbf{v}(\mathbf{x}, t)\Delta t, \quad (2.3)$$

with t being time, Δt the time increment, \mathbf{x} the position vector and \mathbf{v} the wind velocity vector. In general, a wind velocity vector used like this will include several parts in addition to the gridded velocity, such as factors for turbulent velocity fluctuations and mesoscale wind fluctuations (e.g. Draxler and Hess, 1997, Stohl et al., 1998). Whilst these additional factors can potentially be

significant dynamically (e.g. Gupta et al., 1997, Liu, 1956), both these aspects are usually concerned with the dispersive nature of the atmosphere, and will be ignored as a first approximation here. Indeed, accounting for turbulent and mesoscale fluctuations significantly adds to code complexity and computational time. Returning to Equation (2.3), one can see that it will be necessary at each step to interpolate in space for the new wind velocities at that location. Furthermore, it is obvious that a time increment of six hours will not be sufficiently accurate to calculate particle advection, especially for synoptic scale activity, and it will therefore be necessary to adopt a smaller time step by interpolating in time also.

2.3.2 SPECIFICATION

The ERA-Interim reanalysis data mentioned in the previous section is to be input into the LTM at an initial time t_1 (12:00 UTC on our EEs and MEs), with the initial position (longitude, latitude, pressure), \mathbf{x}_1 , to be chosen from regular ERA defined grid points within the GS domain. The meridional and zonal components of the wind velocity, \mathbf{v}_1 , at this grid point are then used to calculate the meridional and zonal changes in distance along great circles of the Earth (assumed to be spherical), to the next timestep $t_1 + \Delta t$, where $\Delta t < 6h$. By holding the longitude (latitude) constant, this meridional (zonal) change in distance is then converted into a change in latitude (longitude) via the Haversine formula

$$\text{haversin}\left(\frac{d}{R_E}\right) = \text{haversin}(\phi_2 - \phi_1) + \cos(\phi_1)\cos(\phi_2)\text{haversin}(\lambda_2 - \lambda_1), \quad (2.4)$$

where $\text{haversin}(\Theta) = \sin^2\left(\frac{\Theta}{2}\right)$, d is the change of distance along a great circle

of the Earth, R_E is the radius of Earth, ϕ_1 and ϕ_2 are the latitudes at positions \mathbf{x}_1 and \mathbf{x}_2 , and λ_1 and λ_2 are the longitudes. The vertical component of \mathbf{v}_1 is also used to calculate the change in pressure, before equation (2.3) is then used to calculate the new position, $\mathbf{x}_2(t_1 + \Delta t)$.

At this next location, \mathbf{x}_2 , interpolation in space is required to calculate the velocity here, \mathbf{v}_2 , from the gridded wind velocities at that time. This is achieved by first locating the closest ERA grid point to \mathbf{x}_2 , and subsequently establishing an interpolation grid along every axis. Multiple trial grid sizes were used in order to choose the optimal size to balance accuracy and computational time. With a fixed vertical size of 3 grid points, variation of the horizontal dimensions in steps of 5 (5x5, 10x10 etc.) showed significant improvement in accuracy up to a size of 15x15, with a reasonable increase in computational time. At 20x20, the increase in accuracy rapidly saturated, whilst the computational time continued to steadily increase. With the horizontal grid fixed at 15x15, variation in the vertical was tested. Here, the restriction was much more rigid, as a decrease to 2 grid points showed a drastic decrease in accuracy, whereas an increase to 4 grid points exhibited a completely impractical increase to computational time. Thus, in the LTM, the interpolation grid was chosen to measure 15x15x3 in terms of grid points. This interpolation grid is then used to calculate the wind velocities at \mathbf{x}_2 , at both t_1 and the successive ERA data time, $t_1 + 6h$. The velocity at $t_1 + \Delta t$ is now calculated using a linearly weighted addition, depending on the number of timesteps in $6h$. After m time-steps, where $m \leq 6$,

$$\mathbf{v}_2 = \frac{6-m}{6}\mathbf{v}(\mathbf{x}_2, t = t_1) + \frac{m}{6}\mathbf{v}(\mathbf{x}_2, t = t_2). \quad (2.5)$$

This weighted velocity is then applied as before to calculate the next position, and this process iterated through in the same manner for subsequent timesteps. The same method is also applied backwards in time to produce back-trajectories,

as well as forward. As the position at each successive time-step is calculated, the interpolation grid is then also used to compute the atmospheric variables associated with the air parcels. These include the relative humidity, specific humidity, air temperature, and geopotential height at that location, as well as the overlying tropopause pressure and surface pressure beneath.

It is noted that the spatial interpolation used by the LTM is cubic spline interpolation, which uses a special type of piecewise polynomial called a spline. Spline interpolation is favoured to polynomial interpolation, because the interpolation error can be made small even when using low degree polynomials for the spline. Alterations are made to the interpolation grid throughout the advection calculations to ensure it remains above surface pressure throughout, whilst maintaining the same size.

In order to choose a suitable time step, it is necessary to test the LTM theoretically across a size range and assess the associated errors and computational time. This is discussed in the next few sections.

2.3.3 THE EADY MODEL

Decades of observations have confirmed that the major source of synoptic scale activity in the atmosphere is due to baroclinic instability in which the available potential energy, manifested in the sloping density surfaces in the region of the westerly winds is released by cyclone scale motions with wavelengths of order 1000km. As mentioned in Section 1.3, Charney (1947) and Eady (1949) independently produced mathematical descriptions of this baroclinic instability. Whilst the Charney problem is in some ways more complete (e.g. allowing for a beta-effect), the Eady problem displays the instability more transparently, capturing the main features of mid-latitude cyclogenesis in a more mathematically simple format. Considering the GS domain is an intense region of mid-latitude

cyclogenesis, a realistic test platform for the LTM would be to input the theoretical velocities of a parcel in an Eady wave and let the model predict its motion before comparing it to a numerically solved calculation of the parcels trajectory.

The Eady model requires some simplifying assumptions:

1. The motion is on an f-plane.
2. The motion is constrained between two rigid, flat horizontal surfaces, representative of the Earth's surface and a constant-height tropopause.
3. The fluid is uniformly stratified, i.e. N^2 is constant. This is a reasonable approximation for the troposphere.
4. The basic state is assumed to have a uniform shear $U_o(z) = \Lambda z = \frac{U_z}{\Gamma}$, where Λ is the (constant) shear and U_z is the zonal velocity at $z = \Gamma$, where Γ is the domain depth.

Under these assumptions, the basic state streamfunction is given by $\psi = -\Lambda zy$, and the basic state potential vorticity is

$$QGPV = \nabla^2 \psi + \frac{\Gamma^2}{L_d^2} \frac{\partial}{\partial z} \left(\frac{\partial \psi}{\partial z} \right) = 0, \quad (2.6)$$

where $L_d = \frac{N\Gamma}{f}$ is the Rossby deformation radius and $QGPV$ is the quasi-geostrophic potential vorticity, where quasi-geostrophic theory requires the assumption of being close to geostrophic flow at all times. In perturbation form, the linearized $QGPV$ equation is therefore given by

$$\left(\frac{\partial}{\partial t} + \Lambda z \frac{\partial}{\partial x} \right) \left(\nabla^2 \psi' + \frac{\Gamma^2}{L_d^2} \frac{\partial^2 \psi'}{\partial z^2} \right) = 0. \quad (2.7)$$

Next, in the horizontal plane the flow is assumed confined to a channel, periodic in x , and confined between two meridional walls of width L . Then, with $\psi = 0$ imposed at $y = \frac{L}{2}$ and $y = -\frac{L}{2}$, solutions of the form

$$\psi'(x, y, z, t) = Re\Phi(z)\sin(ly)e^{ik(x-ct)}, \quad (2.8)$$

where $l = \frac{n\pi}{L}$, where n is a positive integer, $k^2 = \frac{\mu^2}{L^2} - l^2$, where μ is a non-dimensional horizontal wavenumber parameter, scaled by the inverse of the Rossby radius of deformation, and $c = c_r + ic_i$ is the phase speed. Applying the boundary condition that the vertical velocity $w = 0$ at $z = 0$ and $z = \Gamma$ leads to

$$\Phi(z) = A\cosh\left(\frac{\mu z}{\Gamma}\right) + B\sinh\left(\frac{\mu z}{\Gamma}\right), \quad (2.9)$$

where A and B are constants that satisfy

$$A[(c - \Lambda\Gamma)\mu\sinh(\mu) + \Lambda\Gamma\cosh(\mu)] + B[(c - \Lambda\Gamma)\mu\cosh(\mu) + \Lambda\Gamma\sinh(\mu)] = 0,$$

$$A[\Lambda\Gamma] + B[\mu c] = 0. \quad (2.10)$$

Requiring a non-trivial solution to these coupled homogeneous equations leads to $c_r = \frac{U}{2}$ and an instability growth rate

$$\sigma = kc_i = k\frac{U}{\mu}[(\coth(\frac{\mu}{2}) - \frac{\mu}{2})(\frac{\mu}{2} - \tanh(\frac{\mu}{2}))]^{\frac{1}{2}}. \quad (2.11)$$

From the thermal wind relation $\frac{d\bar{u}}{dz} = -\frac{g}{f\theta_o}\frac{d\bar{\theta}}{dy}$, where θ_o is a reference potential temperature, we can see that this is directly proportional to the meridional temperature gradient. The maximum of this growth rate occurs when $\mu = 1.61$. Setting $A = 1$ yields $B = -\frac{\Lambda\Gamma}{\mu c}$, and now we can work out the horizontal per-

turbation velocities as

$$u'(x, y, z, t) = -\frac{\partial \psi'}{\partial y} = -l \cos(\ly) e^{kc_i t} [\cosh(\frac{\mu z}{\Gamma}) \cos(k(x - c_r t))$$

$$- \frac{U c_r}{\mu |c^2|} \sinh(\frac{\mu z}{\Gamma}) \cos(k(x - c_r t)) - \frac{U c_i}{\mu |c^2|} \sinh(\frac{\mu z}{\Gamma}) \sin(k(x - c_r t))], \quad (2.12a)$$

$$v'(x, y, z, t) = \frac{\partial \psi'}{\partial x} = k \sin(\ly) e^{kc_i t} [-\cosh(\frac{\mu z}{\Gamma}) \sin(k(x - c_r t))$$

$$+ \frac{U c_r}{\mu |c^2|} \sinh(\frac{\mu z}{\Gamma}) \sin(k(x - c_r t)) - \frac{U c_i}{\mu |c^2|} \sinh(\frac{\mu z}{\Gamma}) \cos(k(x - c_r t))]. \quad (2.12b)$$

In order to calculate w' , it is necessary to use the linearized thermodynamic equation

$$\frac{\partial \theta'}{\partial t} + \bar{u} \frac{\partial \theta'}{\partial x} + v' \frac{\partial \bar{\theta}}{\partial y} = -w' \frac{\partial \bar{\theta}}{\partial z}. \quad (2.13)$$

Using the relations $\theta' = \frac{\theta_o f}{g} \frac{\partial \psi'}{\partial z}$ and $\frac{\partial \bar{\theta}}{\partial z} = \frac{\theta_o N^2}{g}$ leads to

$$w'(x, y, z, t) = -\frac{c_i k f \mu}{N^2 \Gamma} \sin(\ly) e^{kc_i t} \sinh(\frac{\mu z}{\Gamma}) \cos(k(x - c_r t))$$

$$- e^{kc_i t} \sin(k(x - c_r t)) \left[\frac{k c_r f \mu}{\Gamma N^2} \sin(\ly) \sinh(\frac{\mu z}{\Gamma}) + \frac{k f}{\Gamma N^2} \sin(\ly) U \cosh(\frac{\mu z}{\Gamma}) \right]$$

$$- \frac{U z k f \mu}{\Gamma^2 N^2} \sin(\ly) e^{kc_i t} [-\sinh(\frac{\mu z}{\Gamma}) \sin(k(x - c_r t)) + \frac{U c_r}{\mu |c^2|} \cosh(\frac{\mu z}{\Gamma}) \sin(k(x - c_r t))]$$

$$\begin{aligned}
& -\frac{U c_i}{\mu |c^2|} \cosh\left(\frac{\mu z}{\Gamma}\right) \cos(k(x - c_r t)) + \frac{f U k}{\Gamma N^2} \sin(\mu y) e^{k c_i t} [-\cosh\left(\frac{\mu z}{\Gamma}\right) \sin(k(x - c_r t)) \\
& + \frac{U c_r}{\mu |c^2|} \sinh\left(\frac{\mu z}{\Gamma}\right) \sin(k(x - c_r t)) - \frac{U c_i}{\mu |c^2|} \sinh\left(\frac{\mu z}{\Gamma}\right) \cos(k(x - c_r t))]. \quad (2.14)
\end{aligned}$$

These velocities can now be used to produce 6-hourly velocity-field data to be input into the LTM.

2.3.4 THEORETICAL TESTING OF THE LTM

In our theoretical testing of the LTM, the first mode ($n = 1$) of the Eady wave discussed previously is used and a value of $\mu = 1.61$ chosen such that the instability growth rate is at a maximum ($\sigma_{max} = 0.26 \text{day}^{-1}$). Choosing typical atmospheric values of $\Gamma = 10 \text{km}$, $U = 10 \text{ms}^{-1}$, $N = 10^{-2} \text{s}^{-1}$ leads to $L_d = 1000 \text{km}$. For simplicity here, a Cartesian grid is used and domain values chosen to be realistic of a Northern Hemispheric baroclinic wave. A value of $L = 10000 \text{km}$ is selected, with a realistic global resolution roughly equal to the ERA 0.7° data we will be using: 40000km across 512 longitude grid points, 20000km across 256 latitude grid points, and 10km across 27 pressure levels (1000-100hPa). Finally, it is necessary to select an initial amplitude of perturbation to use. This is done by assuming a reference $\theta_o = 300 \text{K}$, and choosing an amplitude constant coefficient for ψ' to determine a range of initial values of θ' . Here, three initial potential temperature perturbations are examined, from a very calm 0.1K through a reasonable 1K and up to an extreme upper-bound case of 10K. Indeed, some baroclinic waves over the GS are already large in

magnitude, whilst some are just starting to grow.

For each of these initial perturbations, firstly the differential solver “ode45” on MATLAB is used to integrate the velocities numerically for 8 days. Although some error will exist (as on any differential solver), the ode45 solver is for non-stiff differential problems, making any numerical method of solution stable and any error allowed during the integration process extremely small. The initial position selected for the numerical solver is $[0,2500\text{km},5\text{km}]$, i.e. in the mid-troposphere. After 8-day position vectors have been produced, the position at $t = 4\text{days}$ is noted and this vector used for the initial position for our forward and backward trajectories to be calculated by the LTM. 6-hourly gridded Eady-velocity field data can now be produced for each initial perturbation and 4-day forward and backward trajectories produced by the LTM. Here, we present results for time steps of 1 hour and 1 minute.

Figures 2.3-2.5 illustrate LTM results for the Eady wave simulation for an interpolation time step of 1 hour. For initial potential temperature perturbations of 0.1K and 1K, the LTM tracks the Eady-wave trajectory well, with good agreement between the forward and back-trajectories and the numerically solved trajectory. However, for the extreme initial perturbation of 10K, the LTM displays severe error, with the forward and back-trajectories rapidly diverging from the theoretical solution. With any trajectory model that interpolates in the manner of the LTM, the biggest errors will naturally occur when there are velocities that swiftly change in both space and time. In the extreme 10K case, the trajectory travels close to the top of the vertical domain, resulting in rapid oscillatory-like motion in all directions. It is clear from Figure 2.5 that a time step of 1 hour is not small enough to cope with these. Figures 2.6-2.8 illustrate LTM results for the Eady wave simulation for an interpolation time step of 1 minute. The x- and y-difference charts in Figure 2.8, from days 4-8, demon-

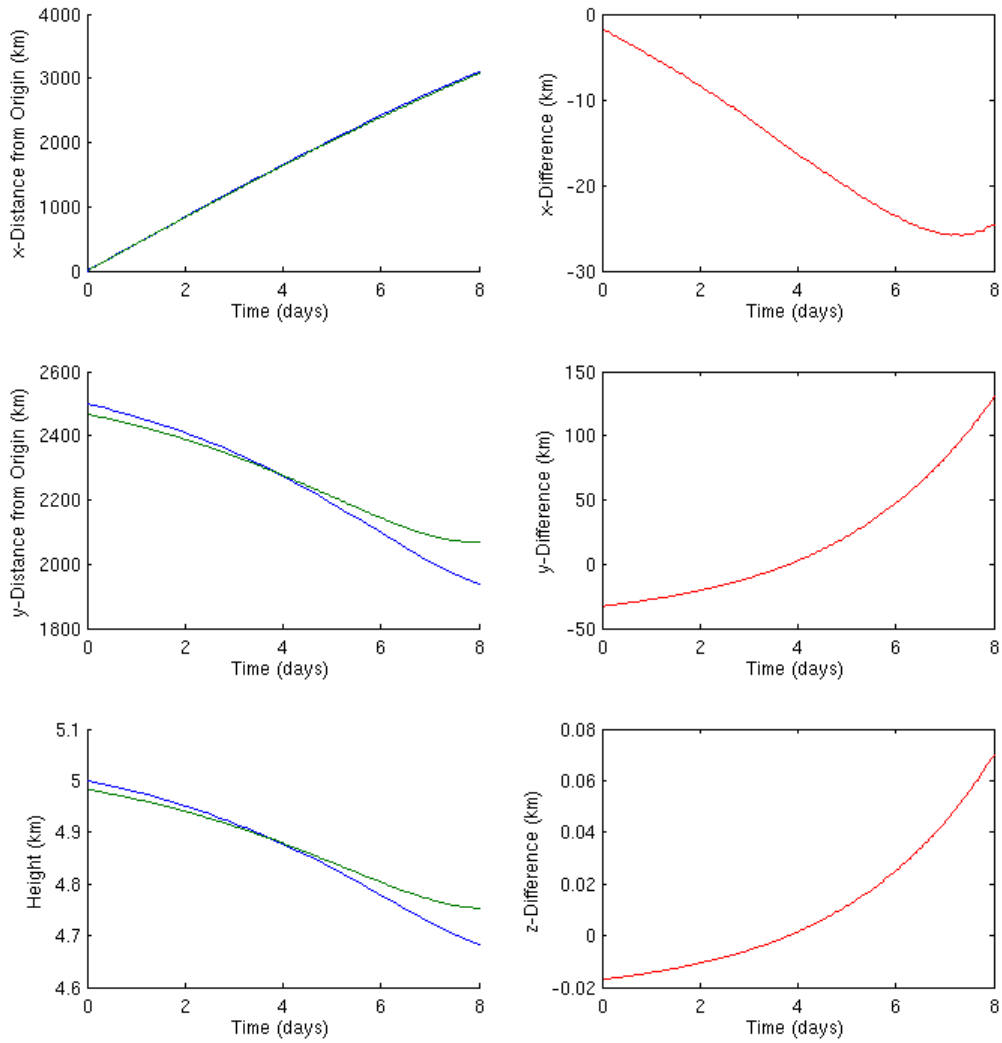


Figure 2.3: Eady-wave theoretical test analysis of the LTM for an initial potential temperature perturbation of 0.1K and a LTM time-step of 1 hour. In blue: Numerically solved 8-day wave trajectories. In green: 4-day forward- and back-trajectories as produced by the LTM. In red: The difference between the LTM and the numerical solution. See text for further description.

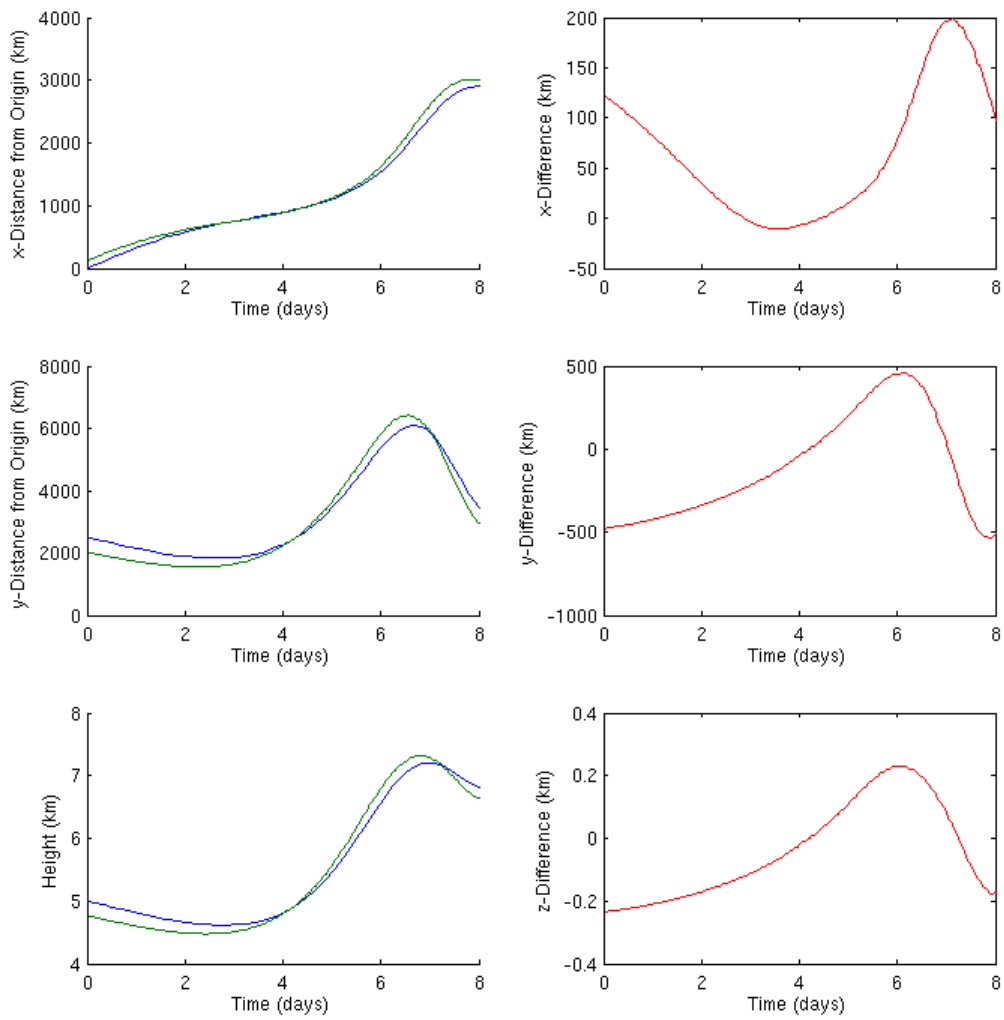


Figure 2.4: As in Figure 2.3, but for an initial potential temperature perturbation of 1K.

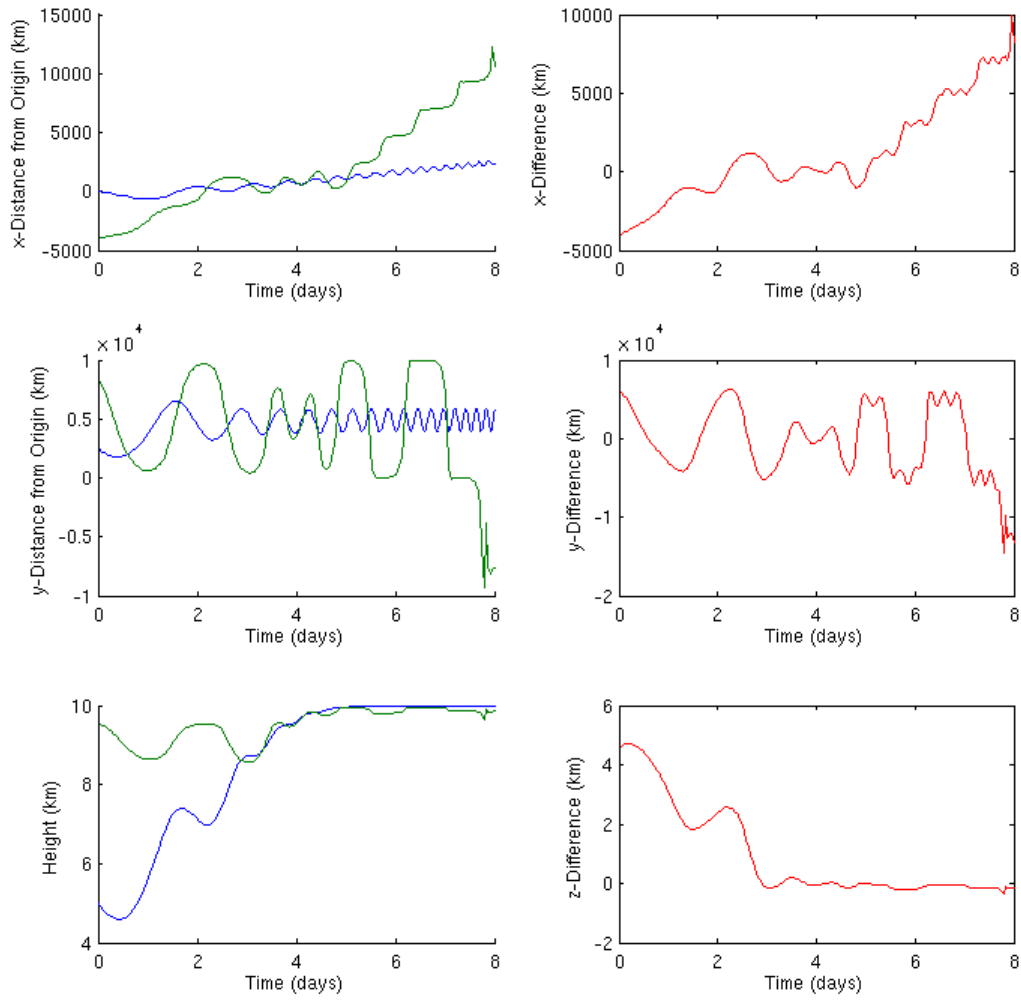


Figure 2.5: As in Figure 2.3, but for an initial potential temperature perturbation of 10K.

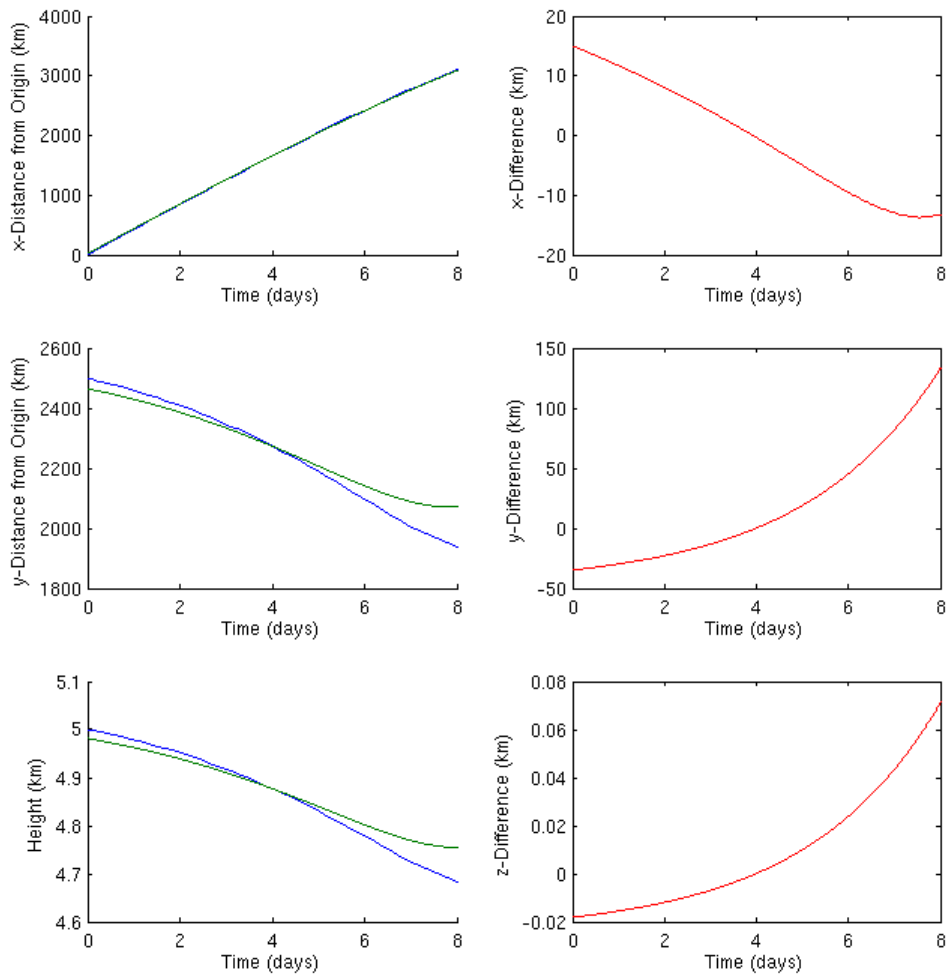


Figure 2.6: As in Figure 2.3, but for a LTM time step of 1 minute.

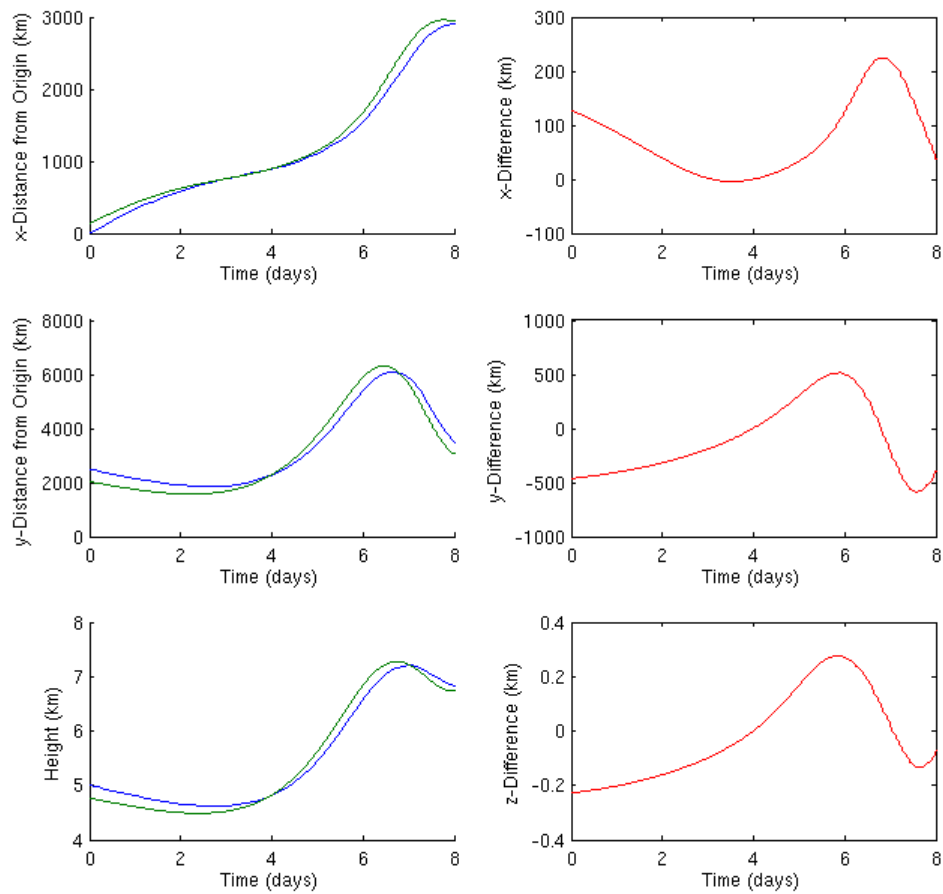


Figure 2.7: As in Figure 2.3, but for an initial temperature perturbation of 1K and a LTM time step of 1 minute.

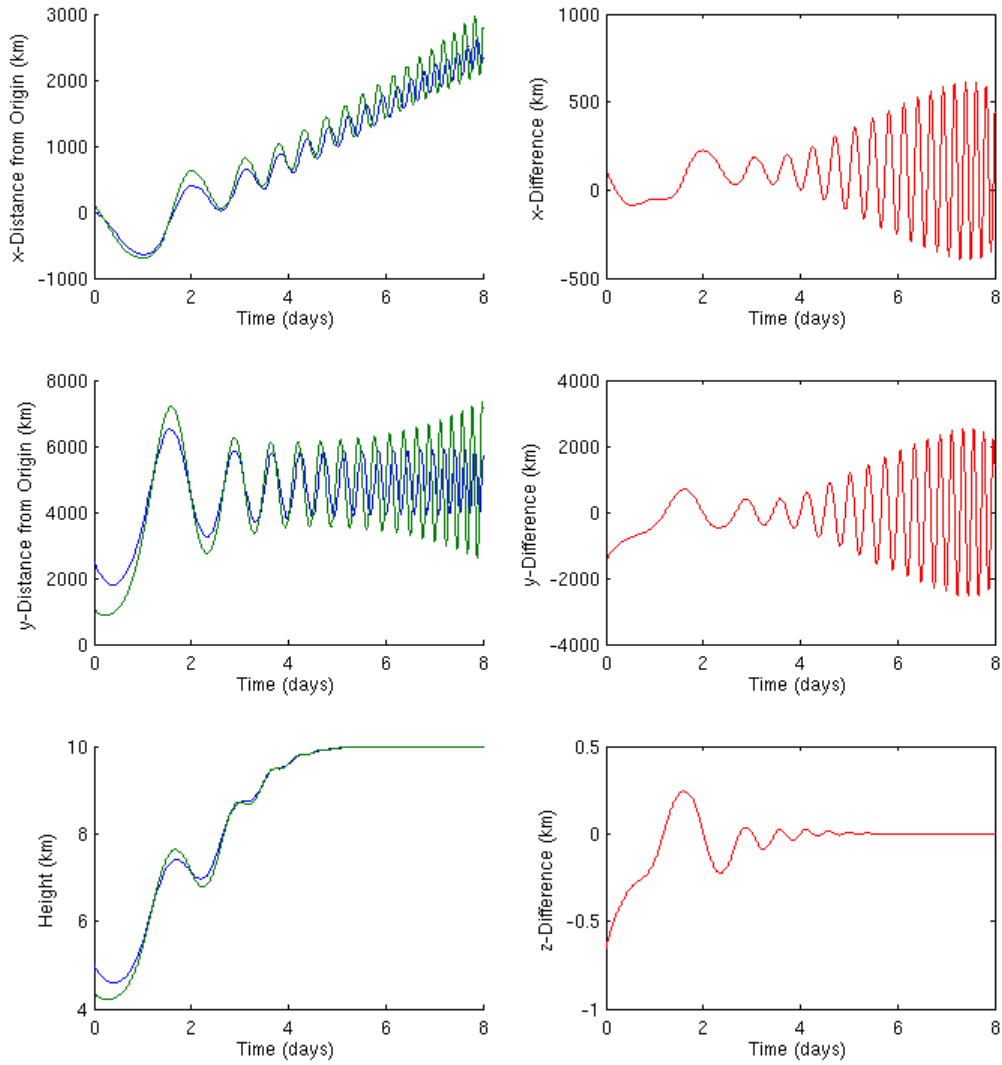


Figure 2.8: As in Figure 2.3, but for an initial temperature perturbation of 10K and a LTM time step of 1 minute.

strate accurately the nature of the increasing amplitude of error associated with high frequency oscillatory-like motion. However, whilst there is not a significant difference to the 1 hour time step in the error for the initial potential temperature perturbations of 0.1K and 1K, there is a marked improvement in the extreme 10K case. A measure of error between the theoretical trajectories and the model output is calculated using the equation

$$Error = \frac{(\Sigma(\mathbf{x}_a - \mathbf{x}_b)^2)^{\frac{1}{2}}}{(\Sigma(\mathbf{x}_b - \mathbf{x}_f)^2)^{\frac{1}{2}}}, \quad (2.15)$$

where \mathbf{x}_a is the LTM output, \mathbf{x}_b are the positions calculated theoretically using numerical integration and \mathbf{x}_f is a vector representing the final position, included in order to accurately represent an error relative to the large scales associated with growing Eady waves.

θ'	0.1K	1K	10K
Error in x	0.35%	3.33%	6.53%
Error in y	6.48%	11.33%	10.15%
Error in z	6.48%	8.83%	3.35%

Table 2.1: Errors between theoretical and LTM backward-trajectory output for an interpolation time step of 1 minute and initial potential temperature perturbations of 0.1K, 1K and 10K.

θ'	0.1K	1K	10K
Error in x	0.40%	4.75%	9.47%
Error in y	19.59%	16.11%	29.48%
Error in z	17.58%	7.21%	1.80%

Table 2.2: As in Table 2.1, but for LTM forward-trajectory output.

Tables 2.1 and 2.2 illustrate the percentage errors calculated by Equation 2.15 for LTM backward and forward trajectories respectively, for an interpolation time step of 1 minute. For the backward trajectory output, the percentage errors in each direction all fall within reason, even for the extreme upper-bound

10K perturbation. For the forward trajectory output, the percentage errors are larger across the board. This is to be expected as the Eady wave grows with time and is more intense here. However, even for these trajectories, the percentage error reads less than 20% in all cases, except for in the y-direction, where the percentage error reads 29.48%. Nevertheless, there are several things to consider. Firstly, the 10K forward-trajectory error is for a developed Eady wave, maturing from a highly intense initial perturbation, and hence represents an extreme upper bound to the analysis here, for which an error of up to 30% is not unreasonable. Indeed, errors of up to 100% have been reported in numerous trajectory models (Stohl, 1998), although average errors of approximately 20% of the travel distance may be considered as more typical in the Northern Hemisphere. In a study of three three-dimensional trajectory models (including FLEXTRA - Stohl et al., 1995, which is considered further in the next section), it was found that when linear spatial interpolation is used, there are deviations in calculations of up to 10% simply between each of the models (Stohl et al., 2001). Secondly, as can be seen from the x- and y-differences in Figure 2.8, the error increases with time. In our real-world analysis in Section 2.4, the forward-trajectory period is $3\frac{1}{4}$ days, and so the associated error will be reduced.

2.3.5 QUALITATIVE COMPARISON WITH A REALISTIC CASE

In Figure 2 in Eckhardt et al. (2004), the Lagrangian trajectory model FLEXTRA (Stohl et al., 1995) is used to calculate 6-day forward (gray) trajectories and 3-day backward (black) trajectories, starting 12:00 UTC 23 Jan 1987 between 30° and 40° N and at 500m above ground level, of WCBs, with 24-hour periods of the forward trajectories marked. WCBs are defined here as those trajectories that, during the first 2 days, travel more than 10° longitude to the east and more than 5° latitude to the north, whilst ascending more than 60% of the

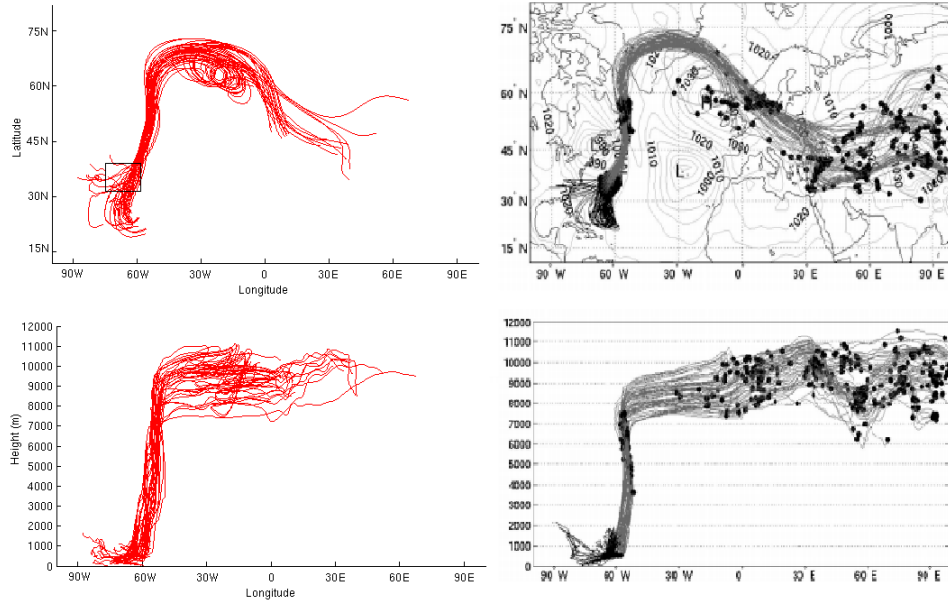


Figure 2.9: (Right) Six-day forward trajectories, and three-day backward trajectories, starting 12:00 UTC 23 Jan 1987, of which the first 2 days were identified as a WCB, using the Lagrangian model FLEXTRA (Eckhardt et al., 2004). Positions along the forward trajectories are marked every 24h. (Left) Comparable calculations done by the LTM for 3 days forward and backward trajectories.

zonally and climatologically averaged tropopause height. Figure 2.9 presents a comparable 3-day forward and backward analysis using the LTM at a time step of 1 minute with ERA-Interim 0.7° data, from regular spacing within our GS domain (that lies inside the latitude boundaries used in Eckhardt et al. (2004)). In our LTM analysis, the tropopause is defined dynamically, using the same ERA-Interim data, as the 2PVU atmospheric level, and the average overlying tropopause between the two days is used to distinguish WCBs, as opposed to the zonal and climatological average; this difference will include (and exclude) some potential WCBs, but should not significantly retract from the comparison. The accuracy of this qualitative “real-world” comparison adds to the previous theoretical test of the LTM, and demonstrates that the LTM is able to accu-

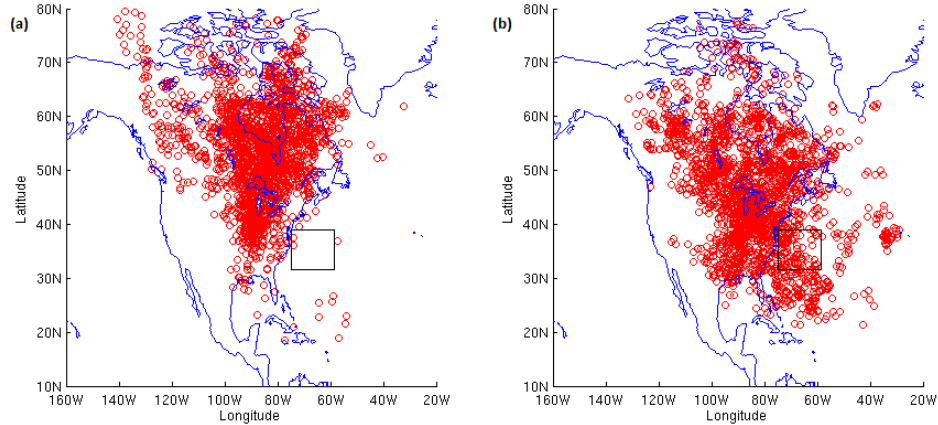


Figure 2.10: Trajectory positions at $t = 0\text{d}$, $3\frac{1}{4}$ days before 12:00UTC on (a) EEs and (b) MEs.

rately reproduce trajectories within airstreams of a cyclone. In addition, it is noted here that initially all trajectory calculations were verified qualitatively against analogous calculations from the BADC, all with comparable success to the aforementioned example.

2.4 EE AND ME TRAJECTORY ANALYSIS

In this section, all the data used is ERA-Interim reanalysis data at 0.7° horizontal resolution with 27 pressure levels (1000-100hPa), provided by the BADC. At 1200 UTC ($t = 3\frac{1}{4}\text{d}$) on the EEs and MEs defined in Section 2.2, initial positions at regular intervals of two horizontal grid points within the GS domain are used to initiate $3\frac{1}{4}$ -day forward and backward trajectories at a pressure level of 950hPa (i.e. low-level), producing a total of 2160, $6\frac{1}{2}$ -day trajectories for the EEs, and similarly for the MEs.

Figures 2.10(a) and (b) illustrate the initial positions (i.e $t = 0\text{d}$) of these trajectories for EEs and MEs, respectively. The GS domain is marked on the

plots, and all these parcels at $t = 0\text{d}$ are located within at $t = 3\frac{1}{4}\text{d}$. The North American continental coast is also marked, and it is possible to see that EEs over the GS region are synonymous with an almost complete exchange of marine air with continental air. On MEs, there is naturally still heavy exchange between them, however a reasonable fraction of the air over the GS at $t = 0\text{d}$ originates over the ocean in the GS region. The marine air here will contain more moisture and will have been warmed by the warm waters underneath, and the surface heat fluxes between the ocean and this air will not be as strong as they would be with the colder continental air. This is consistent with the weaker surface heat fluxes on the MEs.

Figures 2.11 and 2.12 illustrate physical variables averaged over all the trajectories on EEs (red) and the MEs (blue). In Figure 2.11, the average trajectory on EEs and MEs is shown. The average flow prior to our days of extreme heat flux is more northerly than prior to our median days by around 8° , and originates roughly 3° further to the west. Vertically, trajectories prior to EEs originate $\sim 50\text{hPa}$ ($\sim 500\text{m}$) lower in the troposphere on average than those prior to MEs. Obviously, at $t = 3\frac{1}{4}\text{d}$, the trajectories intersect. Post-interaction with the GS domain, air parcels on average travel significantly higher ($\sim 130\text{hPa}$, $\sim 1500\text{m}$) and further east ($\sim 8^\circ$), and slightly further north ($\sim 2^\circ$) after MEs than EEs.

In Figures 2.12 (a)-(d), the averages along the EE (red) and ME (blue) trajectories of some atmospheric variables are presented. On average, trajectories associated with EEs are initially colder and contain less moisture than those associated with MEs. This is to be expected from Equations 2.1 and 2.2, and the greater percentage of trajectories that have continental origin. Both sets of trajectories display a sharp increase in temperature and specific humidity at $\sim t = 3\frac{1}{4}\text{d}$ as they pass over the warm waters of the GS, before exhibiting a decrease with time as they move away to colder regions where some of the

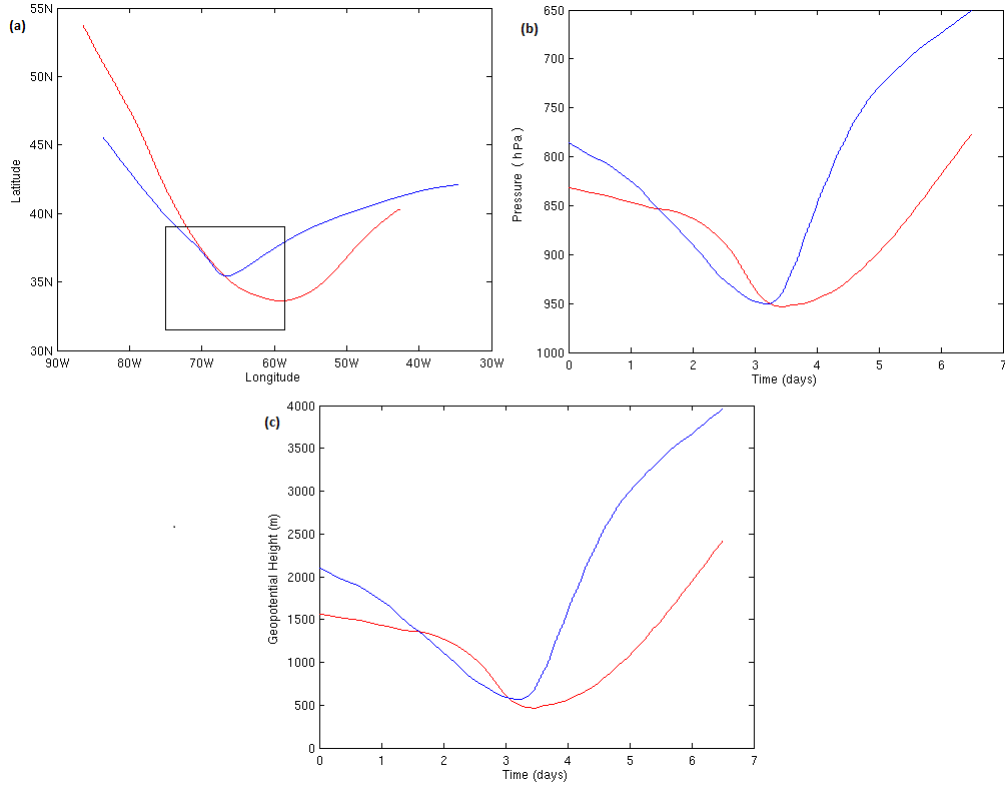


Figure 2.11: Average across all trajectories on EEs (red) and MEs (blue) of the (a) parcel longitude and latitude (b) parcel pressure height and (c) parcel geopotential height.

parcels will precipitate. Opposite to the initial state, the trajectories associated with EEs finish at $t = 6\frac{1}{2}$ d with higher moisture content and temperature than those associated with MEs, a trend that is also reflected in the average moist static energy ($MSE = c_p T + gz + l_v q$, where l_v is the latent heat of vaporization of water) of the air parcels. The average EE relative humidity however, is greater both initially and finally than the ME counterpart. Figures 2.12 (e)-(f) display the average underlying surface pressure and overlying tropopause height following the air parcels on EEs and MEs. On average, prior to interaction with the GS domain, the overlying tropopause height for EEs is lower than for MEs,

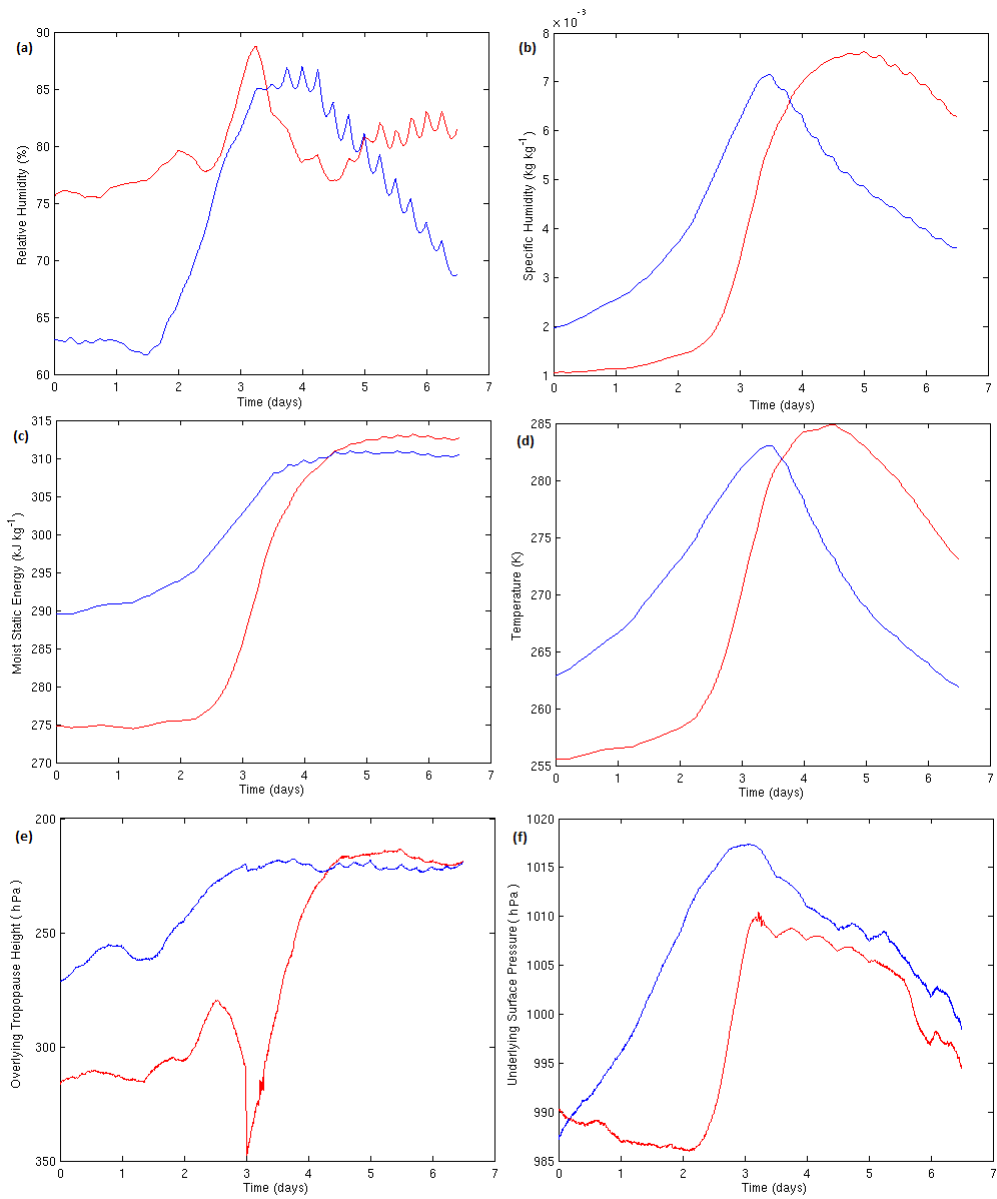


Figure 2.12: Average across all trajectories on EEs (red) and MEs (blue) of the (a) parcel relative humidity (b) parcel specific humidity (c) parcel moist static energy (d) parcel temperature (e) overlying tropopause height and (f) underlying surface pressure.

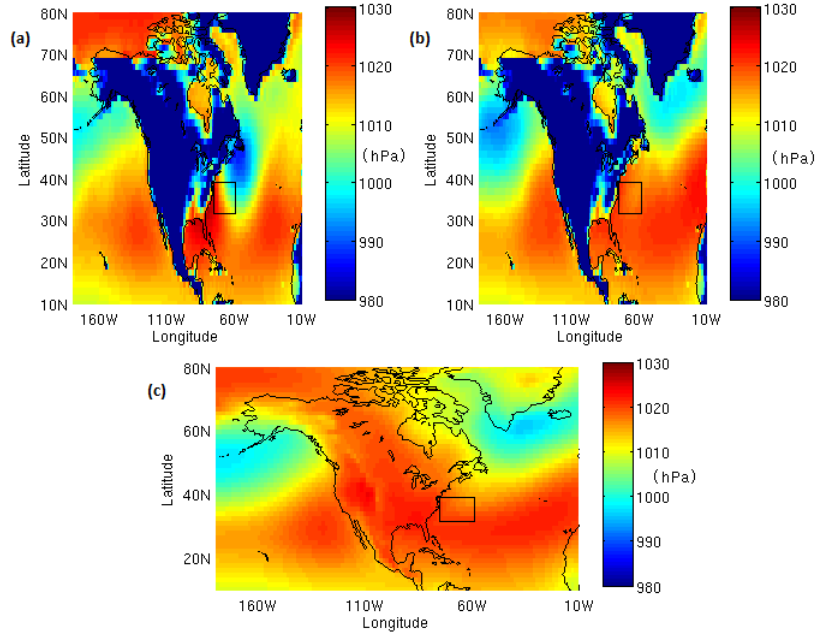


Figure 2.13: Surface pressure at $t = 3\frac{1}{4}$ d, averaged across (a) EEs and (b) MEs. (c) Average mean sea level pressure, 12:00UTC, DJF, 1979-2011.

before exhibiting a sharp spike in depth and subsequently returning rapidly to the same level. With respect to underlying surface pressure, the average starts off the same for EEs and MEs.

Figure 2.13 aids in understanding the trajectory average in Figure 2.12(f) up to $t = 3\frac{1}{4}$ d. As can be seen from Figures 2.13 (a) and (b), the surface pressure over land (over which the majority of the air parcels for both sets of events start) is significantly lower than over the ocean. This is due to the presence of land orography. Figure 2.13(c) illustrates the ERA-Interim, 3-hour forecast, 12:00UTC DJF 1979-2011 average in mean sea level pressure (MSLP, which is the surface pressure “corrected” to sea level, i.e. if the air parcels were actually located at sea level), and as expected the apparent discontinuity between land and ocean disappears. The increase in surface pressure up to $t = 3\frac{1}{4}$ d on MEs

and EEs would therefore appear to be associated with air parcels as they move from land over the ocean. Figures 2.14(a)-(e) illustrate composites of the MSLP from two days prior to EEs through to two days afterwards. As can be seen, a developing westerly low pressure anomaly exists over the GS domain prior to the day of extreme heat flux, that subsequently moves north-east on the day itself. The trailing high pressure anomaly is consistent with a developing baroclinic system (Section 1.3), and the extreme heat fluxes on our EEs with the cold dry air behind the cold fronts in synoptic systems (Section 1.7). Figures 2.15(a)-(e) illustrate the same as in Figure 2.14, but for the MEs, and as can be seen there are no analogous low or high MSLP anomalies. It is possible then that the presence of a low pressure system on EEs, but not MEs, may influence the difference in the manner of the increase to maximum in surface pressure in Figure 2.12(f). In order to assess the extent of this influence, it would be necessary to plot EE and ME trajectory averages for the MSLP to distinguish between the effect of the orography and the cyclone low pressure. Unfortunately, the MSLP trajectory average data is not available and can not be considered here.

In Figure 2.10, it was possible to infer a north-westerly flow for the vast majority of EE air parcels, and to a lesser, but still significant extent for the ME air parcels (with the inclusion of some marine air). Whilst there may be various airstreams originating at different heights, one can have a reasonably general idea of the EE and ME inflows and their physical properties. Figures 2.16(a) and 2.16(b) illustrate the final positions (i.e $t = 6\frac{1}{2}$ d) of these trajectories for EEs and MEs, respectively. With such a wide spread in both longitude and latitude, it is evident that it is harder to make a comparable inferral for the EE and ME outflows and their general properties.

In fact, Table 2.3 illustrates that the percentage of air parcels that travel

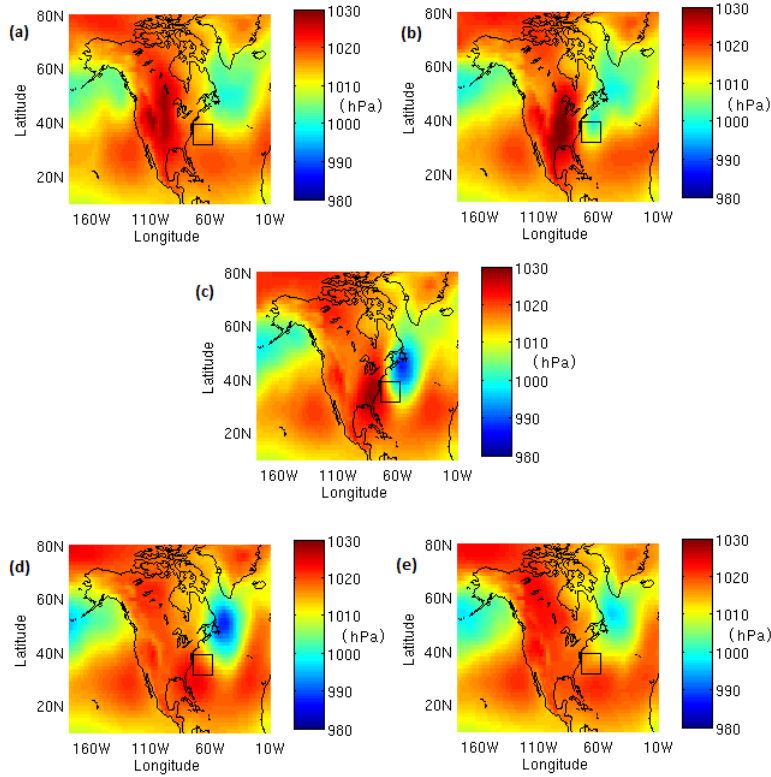


Figure 2.14: (a)-(e) Composites of the MSLP averaged across EEs from two days prior to the EEs through to two days afterwards.

and end up south of the 35.25° latitude line in the middle of the GS domain, whilst less than those that travel and end up north of the line, still make up a significant fraction of the total trajectories on both EEs and MEs. For this reason, it is informative to compare trajectories after $t = 3\frac{1}{4}$ d on EEs and MEs that end up north and south of the 35.25° latitude line.

Figure 2.17 illustrates the trajectory-averaged geopotential height, specific humidity and temperature for parcels that end up north and south of 35.25° N for MEs (blue) and EEs (red). After $t = 3\frac{1}{4}$ d, for both MEs and EEs, trajectories that travel north in general steadily rise, accompanied by a steady decrease

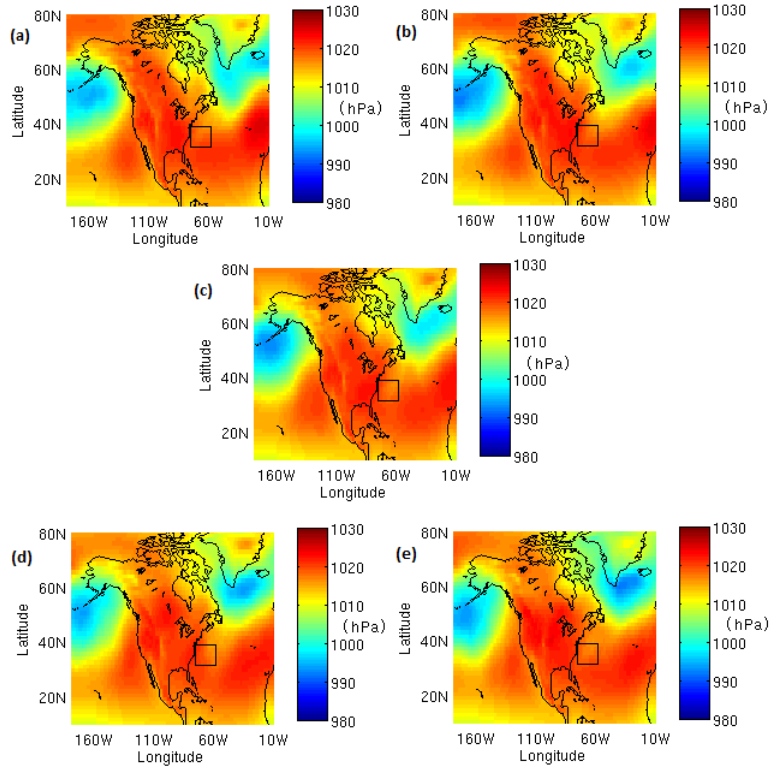


Figure 2.15: As in Figure 2.14, but for MEs.

in temperature and specific humidity (i.e. the parcels rise, cool and precipitate). This is in contrast to those that travel south. On EEs, those that travel south after $t = 3\frac{1}{4}$ d instead remain at low level, increasing in moisture content and rising to a fairly constant temperature. On MEs, those that travel south after $t = 3\frac{1}{4}$ d do generally increase in height for roughly $1\frac{1}{2}$ d (decreasing in temperature and moisture content), before decreasing in height again to relatively low

	>35.25°N	<35.25°N
EE	57.3%	42.7%
ME	63.1%	36.9%

Table 2.3: Percentages of trajectories on EEs and MEs that end up north and south of the 35.25° latitude line.

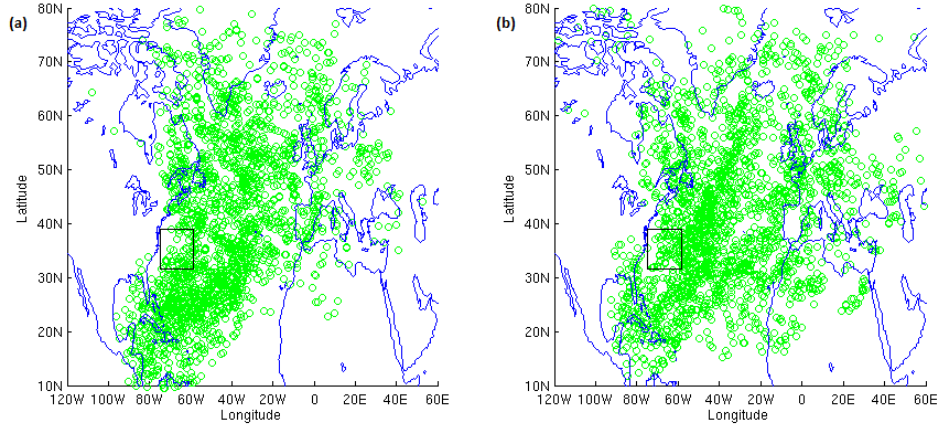


Figure 2.16: Trajectory positions at $t = 6\frac{1}{2}$ d, $3\frac{1}{4}$ days after 12:00UTC on (a) EEs and (b) MEs.

level (and increasing in temperature and moisture content once more).

Figure 2.18 illustrates the trajectory-averaged moist static energy and overlying tropopause height for parcels that end up north and south of 35.25° latitude for MEs (blue) and EEs (red). After $t = 3\frac{1}{4}$ d for north-travelling parcels the MSE reaches a maximum and slowly decreases. On EEs, there is an initial sharp decrease in the overlying tropopause pressure followed by a steady increase, whereas on MEs there is just an increase. After $t = 3\frac{1}{4}$ d for south-travelling parcels, the MSE continually increases whilst there is a continual decrease in the overlying tropopause pressure.

2.5 THE GULF STREAM BOUNDARY LAYER HEAT BUDGET

The results presented in the previous section track atmospheric behaviour over the GS domain on EEs and MEs and illustrate that continental air parcels experience strong changes in their physical variables as they travel over the warmer ocean waters, most notably a significant increase in their moist static

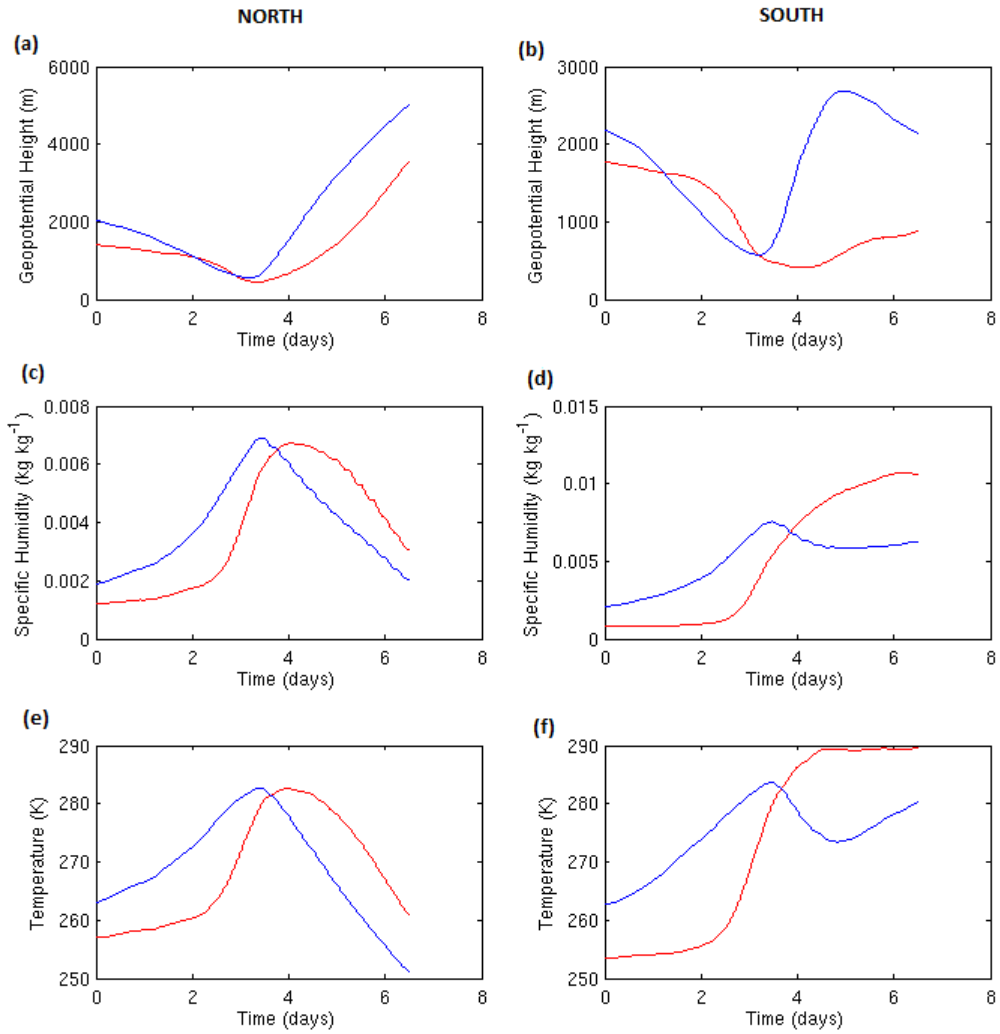


Figure 2.17: Average on EEs (red) and MEs (blue) of the parcel geopotential height, parcel specific humidity and parcel temperature across all trajectories that end up (a,c,e) north of 35.25°N (b,d,f) south of 35.25°N . It is noted that the vertical scale is different in (a) and (b), and in (c) and (d).

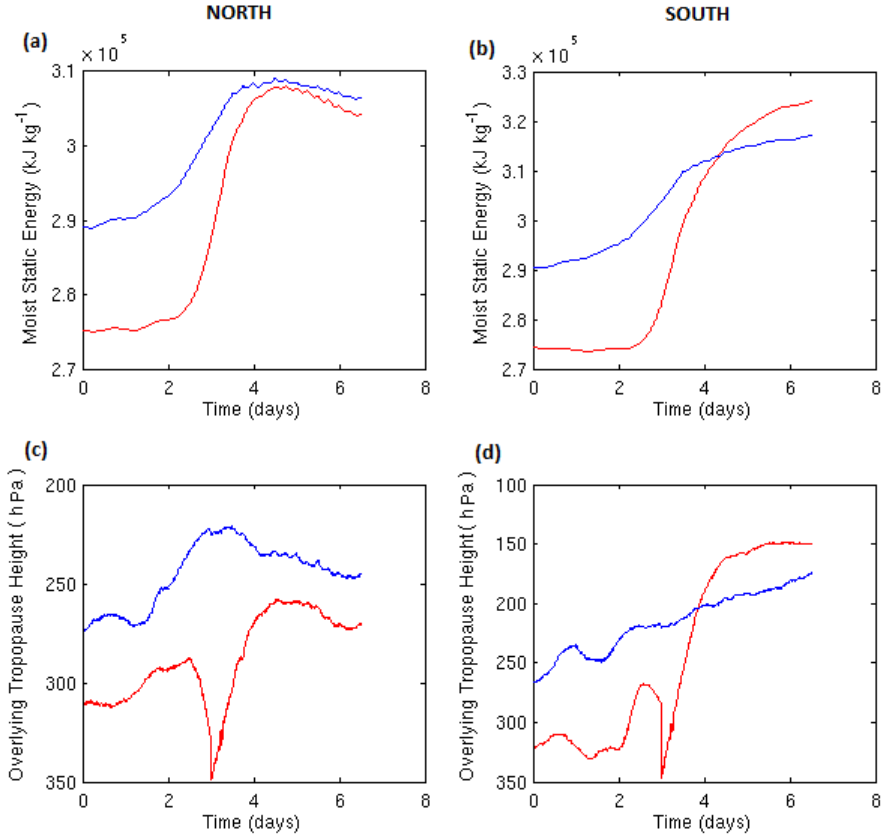


Figure 2.18: Average on EEs (red) and MEs (blue) of the parcel moist static energy and overlying tropopause height across all trajectories that end up (a,c) north of 35.25°N (b,d) south of 35.25°N.

energy. Indeed, in Section 1.6, the concept of an ocean-atmosphere “relay” in poleward heat transport was introduced, with a switch in dominance between the ocean and atmosphere occurring at mid-latitudes. This section is concerned with the direct interaction between the GS and the overlying air parcels. Firstly, an attempt is made to quantify the link between the strong surface heat fluxes in this region and the subsequent atmospheric motions presented previously. This is done by examining the boundary layer heat budget over the GS domain

for our EEs and MEs. Secondly, the differences in atmospheric response to the surface heat fluxes in this region between MEs and EEs are discussed.

2.5.1 MOIST ENTHALPY

Consider a given volume of air of density ρ , composed of a mixture of dry air, water vapour and liquid water, with respective mass mixing ratios q_d , q_v and q_l . Conservation of mass reads (Pauluis and Held, 2002):

$$\partial_t(\rho q_d) + \partial_i(\rho q_d u_i) = 0, \quad (2.16)$$

$$\partial_t(\rho q_v) + \partial_i[\rho q_v u_i + J_{v,i}] = e - \kappa, \quad (2.17)$$

$$\partial_t(\rho q_l) + \partial(\rho q_l u_i) + \partial_z(\rho q_l V_T) = \kappa - e, \quad (2.18)$$

where e and κ refer to the rate of evaporation and condensation per unit volume, V_T is the mean velocity at which cloud droplets and raindrops fall, u_i is the i -th component of velocity, and $J_{v,i}$ represents the i -th component of the diffusive flux of water vapour. By definition, $q_d + q_v + q_l \equiv q_d + q_t = 1$, and summing Equations 2.16-2.18 leads to:

$$\partial_t \rho + \partial_i(\rho u_i) = \dot{q}_v + \dot{q}_l, \quad (2.19)$$

with

$$\dot{q}_v \equiv -\partial_i J_{v,i}, \quad (2.20)$$

$$\dot{q}_l \equiv -\partial_z(\rho q_l V_T). \quad (2.21)$$

The 1st law of thermodynamics for this system can be written in terms of its enthalpy, H , according to (Pauluis and Held, 2002)

$$\delta H = \delta Q + \frac{Dp}{Dt}, \quad (2.22)$$

where δQ is the local heating rate (radiation, sensible heat flux - *not* phase change as it is internal to the sample), $\frac{Dp}{Dt}$ is the pressure variation following the flow, and δH is the local enthalpy change

$$\delta H \equiv \partial_t(\rho h) + \partial_i[\rho u_i h + J_{v,i} h_v] + \partial_z(\rho q_l V_T h_l). \quad (2.23)$$

All the terms in Equation 2.22 are in Wm^{-3} . In Equation 2.23, h is the specific enthalpy of the sample:

$$h = q_d h_d + q_v h_v + q_l h_l, \quad (2.24)$$

with

$$h_d = c_{p,d}(T - T_o) + h_{d,o}, \quad (2.25)$$

$$h_v = c_{p,v}(T - T_o) + h_{v,o}, \quad (2.26)$$

$$h_l = c_l(T - T_o) + h_{l,o}, \quad (2.27)$$

where T_o is a reference temperature at which the enthalpies have the values $h_{d,o}$, $h_{v,o}$ and $h_{l,o} = h_{v,o} - l_v(T_o)$. Equation 2.24 can also be written as

$$h = q_d h_d + q_v (l_v + h_l) + q_l h_l = [(1 - q_t) c_{p,d} + q_t c_l] (T - T_o) + l_v q_v + h_o, \quad (2.28)$$

where

$$h_o = (1 - q_t) h_{d,o} + q_t h_{l,o}. \quad (2.29)$$

Since $h_{v,o} - h_{l,o} = l_v(T_o) \equiv l_{v,o}$, there are only three parameters, $h_{d,o}$, $h_{v,o}$ and $h_{l,o}$, to set in order to select a reference state. Simplicity suggests setting $h_{d,o} = 0$ and choosing $h_{l,o} = 0$ leads to $h_{v,o} = h_{l,o}$, providing $h = h_m$, where h_m is the *moist enthalpy* (Pauluis et al., 2010, Emanuel, 1994, section 4.5)

$$h_m \equiv [(1 - q_t) c_{p,d} + q_t c_l] (T - T_o) + l_v q_v. \quad (2.30)$$

Rewriting the 1st law in Equation 2.22 as

$$\delta H = \rho \frac{Dh}{Dt} + (h - h_v) q_v + (h - h_l) q_l + J_{v,i} \partial_i h_v + \rho q_l V_T \partial_z h_l, \quad (2.30)$$

we can now simplify by looking at the order of magnitude of the terms

$$h - h_v \approx h_d - h_v = (c_{p,d} - c_{p,v})(T - T_o) + h_{d,o} - h_{v,o}, \quad (2.31)$$

$$h - h_l \approx h_d - h_l = (c_{p,d} - c_l)(T - T_o) + h_{d,o} - h_{l,o}, \quad (2.32)$$

and considering the moist enthalpy such that $h_d - h_v \approx (c_{p,d} - c_{p,v})(T - T_o) - l_{v,o} \approx -l_{v,o} \gg h_d - h_l = (c_{p,d} - c_l)(T - T_o)$ leads to

$$\delta H_m \approx \rho \frac{Dh_m}{Dt} - l_{v,o} \dot{q}_v + J_{v,i} \partial_i h_v + \rho q_l V_T \partial_z h_l. \quad (2.33)$$

Equation 2.13 can be simplified even further when considering a low level flow within a boundary layer of thickness τ , with scalings

$$l_{v,o} \dot{q}_v \approx \frac{l_{v,o} \varepsilon}{d}, \quad (2.34)$$

$$l_{v,o} \dot{q}_l \approx \frac{l_{v,o} P}{d}, \quad (2.35)$$

$$J_{v,i} \partial_i h_v \approx J_{v,z} \partial_z h_v \approx \frac{\varepsilon c_{p,v} g}{c_{p,d}}, \quad (2.36)$$

$$\rho q_l V_T \partial_z h_l \approx \frac{P c_l g}{c_{p,d}}, \quad (2.37)$$

where ε and P are the surface evaporation and surface precipitation and it has been assumed the lapse rate is close to the dry adiabat ($g/c_{p,d}$). It can be seen that the last two terms on the r.h.s of Equation 2.33 can be neglected as long as the boundary layer is shallower than a reference depth, τ_{ref} , where in the atmosphere

$$\tau_{ref} \equiv \frac{l_{v,o} c_{p,d}}{g c_l} \simeq 64 km, \quad (2.38)$$

which is indeed the case. As a result, we can now write the 1st law as

$$\rho \frac{Dh_m}{Dt} \approx l_{v,o} \dot{q}_v + \delta Q + \frac{Dp}{Dt}. \quad (2.39)$$

It is noted that the moist enthalpy can be increased by evaporation ($\dot{q}_v > 0$), since a high reference value has been given to vapour, whereas it is not changed by precipitation, since a zero reference value is given to the enthalpy of liquid water.

2.5.2 THE BOUNDARY LAYER HEAT BUDGET

In this section, the aim is to apply Equation 2.39 to the MABL above our GS domain. In a broad general sense, the boundary layer is defined as that part of the atmosphere that directly feels the effect of the Earth's surface. It is possible to physically define the boundary layer in a variety of ways, however the method used by ECMWF involves the bulk Richardson method proposed by Troen and Mahrt (1986). It is defined as the level where the bulk Richardson number, a dimensionless number relating vertical stability and vertical shear, reaches the critical value $Ri_{crit} = 0.25$.

Figure 2.19 illustrates the GS domain-averaged boundary layer height (ECMWF, resolution 1.5° forecast data) on (a) EEs and (b) MEs and for a time lag and lead of 3 days ($t = \frac{1}{4}\text{d}$ to $t = 6\frac{1}{4}\text{d}$), along with plus or minus one standard deviation of heat flux across each day. In a similar manner to Figure 2.2, one observes a discrete spike in boundary layer height over the domain on EEs to coincide with the large spike in surface heat flux, whereas there is no discernible change in boundary layer height on MEs.

Figure 2.20 illustrates the processes affecting the boundary layer heat budget over the GS addressed in Equation 2.39. The surface sensible and latent heat fluxes will increase the moist enthalpy of an example air parcel whilst it is in the

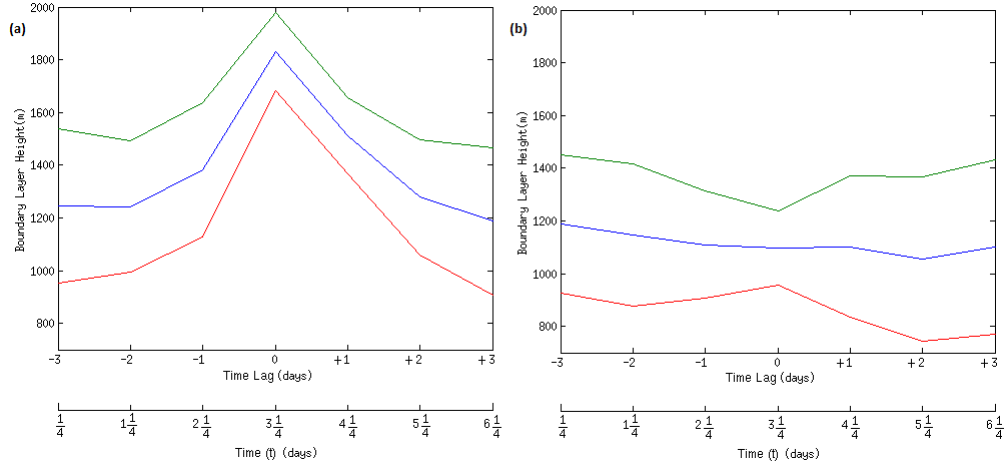


Figure 2.19: In blue: GS domain-averaged daily boundary layer height, averaged across (a) EEs and (b) MEs with a time lag of $\pm 3d$. The green and red lines represent \pm one standard deviation in the boundary layer height across each set of days. The corresponding time t is also given for reference.

domain from h_{in} to h_{out} , whilst the volume can also gain or lose thermal energy via radiation (in all directions) or entrainment flux (at the boundary layer top). Entrainment here is the process whereby the turbulence in the boundary layer spreads with time into the overlying non-turbulent flow. This process can be crucial in controlling the budget of heat in the MABL (as well as other variables such as water vapour and carbon dioxide (Huang et al., 2011). Unfortunately, accurate entrainment parameterizations are very complex and necessitate a high degree of computationally intensive calculation to implement. In addition, accurate calculation of radiation at various levels within the troposphere requires significant use of advanced radiative transfer equations. Indeed, even the sign of longwave radiative heating is controversial near the surface (Stull, 1988), especially at night time where simulations suffer from inaccurate longwave radiation schemes (e.g. Zhong and Fast, 2003). For these reasons, explicit calculations used in our heat budget analysis here ignore the entrainment and radiation flux, and instead focus on the contribution of the surface heat fluxes. Further

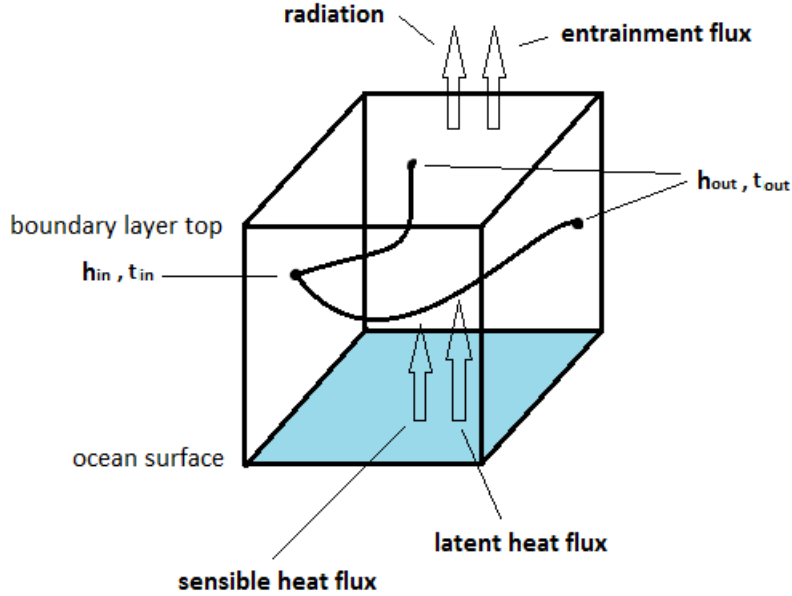


Figure 2.20: Main processes affecting the boundary layer heat budget over the GS. Strong ocean-atmosphere heat fluxes exist at the surface, with entrainment flux affecting at the boundary layer top. Radiation is represented with a “net” arrow at the boundary layer top, but naturally exists at the surface as well, and can act to cool or warm the boundary layer. The net flux in the horizontal is assumed to be zero.

justification is given later in the section. In any case, the results are nevertheless informative, and indeed subsequent inferences about the contribution of the radiation and entrainment fluxes can be made.

In Section 2.4, the $3\frac{1}{4}$ -day forward and back-trajectories of 2160 air parcels that are located above the GS domain on our EEs and MEs were calculated every minute. Taking one of these air parcels travelling through the MABL above the GS domain to be representative of the MABL volume, and ignoring the entrainment and radiation fluxes, Equation 2.39 leads to

$$h_{out} - h_{in} = \int_{t_{in}}^{t_{out}} \frac{Q_l + Q_s}{\rho\tau} dt + \int_{t_{in}}^{t_{out}} \frac{\omega}{\rho} dt. \quad (2.40)$$

In this equation, h_{out} and h_{in} are the moist enthalpies of the air parcel at the time of exit (t_{out}) and entrance (t_{in}) into the MABL above the GS domain respectively, Q_l and Q_s are the surface latent and sensible heat fluxes that act upon the air parcel at each minute along its trajectory, $\rho = \rho(t)$ is the density of the air parcel, $\tau = \tau(t)$ is the height of the MABL above the air parcel and $\omega = \frac{Dp}{Dt}$ is the change in pressure of the air parcel with respect to time. The method of spatial and time-interpolation for τ , ρ , ω , Q_l and Q_s is the same as used in Section 2.4. Furthermore, our results from Figure 2.12(b) show that $q_t \ll 1$ and so Equation 2.30 leads to $h_{out} - h_{in} = c_{p,d}(T_{out} - T_{in}) - l_v(q_{v_{out}} - q_{v_{in}})$.

First of all, all trajectories that are located outside of the MABL at 1200UTC on our EEs and MEs are discarded. This accounts for 101 trajectories for MEs and 2 trajectories for EEs. Equation 2.40 is then applied to each of the trajectories on both our EEs and MEs.

Figure 2.21 illustrates the heat budget in Equation 2.40 for EEs as a scatter plot for each trajectory calculation. A line of exact equality is plotted in red, and the line of best fit for our experimental calculations plotted in black. The gradient of the line of best fit is 0.99 and the offset, taken to be a measure of the error associated with the calculation, is $+0.13 \text{ kJ kg}^{-1}$. It can be seen that on our extreme events, the change in thermal energy in the MABL above the GS domain can be almost entirely ($\sim 99\%$) accounted for by the surface heat fluxes and the change in atmospheric pressure. Analogously to Figure 2.21, Figure 2.22 illustrates the heat budget in Equation 2.40 for MEs. The gradient of the line of best fit in this case is 0.83 and the offset is -1.26. Therefore in the case of median heat flux, the surface heat fluxes and change in atmospheric pressure still account for the majority of MABL enthalpy change over the GS domain,

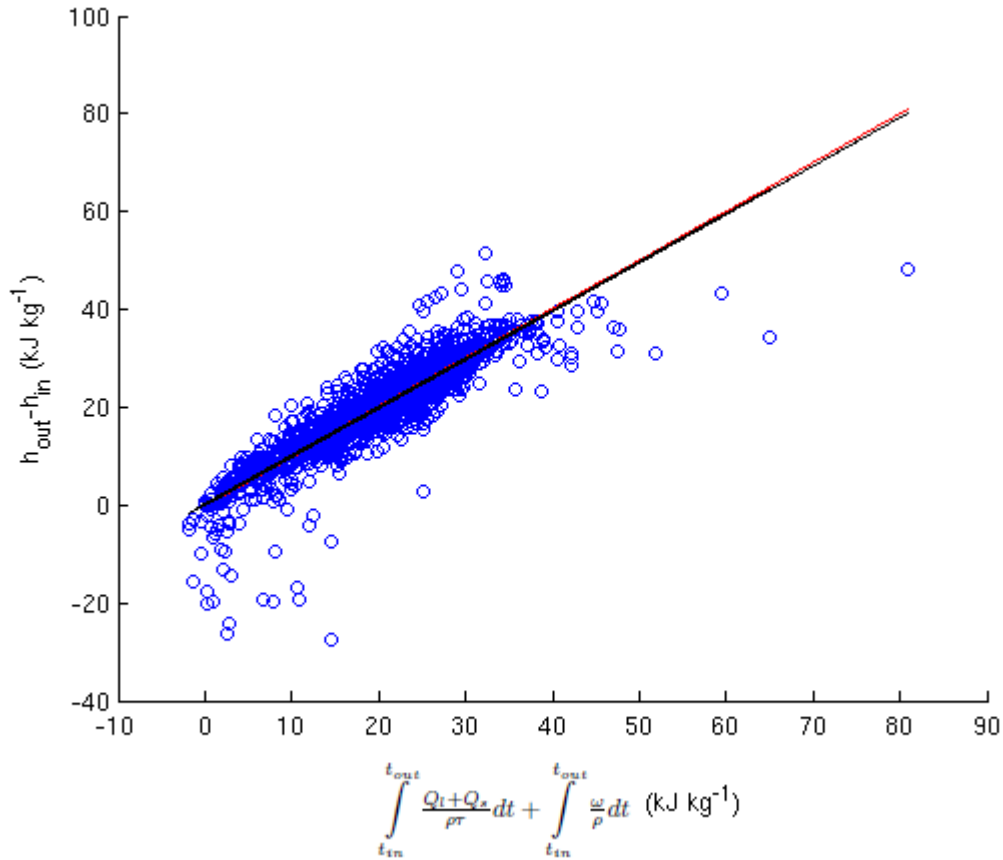


Figure 2.21: In blue: The thermal energy budget in the MABL above the GS domain for each of the representative trajectories on EEs. A line of unit gradient is shown in red and the line of best fit is shown in black.

however there is a more significant fraction ($\sim 17\%$) of the enthalpy change that remains unaccounted for.

Table 2.4 includes some key statistics on the EE and ME trajectories that aids in understanding the results presented in Figure 2.21 and Figure 2.22. First, let us return to the neglect of radiation from our heat budget equation. Firstly, the average time spent in the MABL above the GS domain is 0.49 days on EEs and 0.84 days on MEs, (calculated for each individual trajectory as

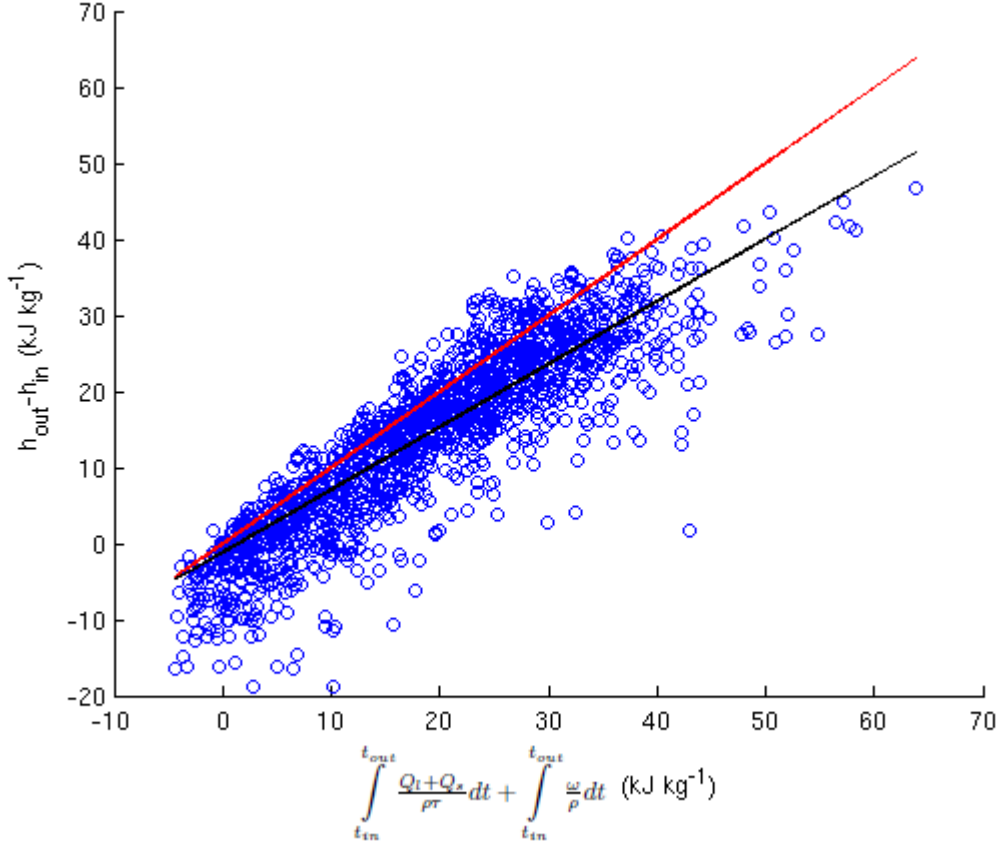


Figure 2.22: As in Figure 2.21, but for trajectories on MEs.

the difference in time between the first exit out of the domain forward, and the first exit backwards). In a mid-latitude boundary layer, typical radiative heating rates are on the order $\sim -1\text{K/day}$ (Savijarvi, 2006). Over 0.49d (0.84d), this heating rate leads to a thermal energy decrease of roughly $c_p T \sim 0.5\text{kJ kg}^{-1}$ ($\sim 0.85\text{kJ kg}^{-1}$). Compared to the magnitudes observed in Figure 2.21 and Figure 2.22, it would appear satisfactory to neglect the radiation term. It is noted that the time spent by air parcels associated with EEs and MEs will encounter the GS at different times of the day. However, our considerations here

	$(t_{out} - t_{in})$	Boundary layer top exit	$\int_{t_{in}}^{t_{out}} \frac{\omega}{\rho} dt$ contribution
EEs	0.49d	0.32%	5.08%
MEs	0.84d	26.2%	-7.11%

Table 2.4: Table representing the average time spent in the MABL above the GS domain in our heat budget analysis, the number of trajectories that exit the GS domain through the boundary layer top, and the contribution of the conversion term to the r.h.s of the heat budget in Equation 2.40.

in the boundary layer are over the ocean, and as such are unlikely to be affected by the diurnal cycle of the underlying SSTs (as they vary little throughout the day).

Neglecting radiation implies that any disparity in the heat budget is due to the entrainment flux. For buoyancy fluxes a constant value of 0.2 is considered to represent the entrainment-to-surface flux ratio for the equilibrium state developed in a linearly stratified atmospheric boundary layer (Fedorovich et al., 2004), although higher values have been observed (e.g. Angevine, 1999). For EEs, the effect of entrainment flux is negligible, whereas for MEs, entrainment could account for up to 17% of the total heat budget, a value consistent with the previously mentioned equilibrium state entrainment-to-surface flux ratio of 0.2.

Another interesting result presented in Table 2.4 is the contribution of the change in pressure term $\int_{t_{in}}^{t_{out}} \frac{\omega}{\rho} dt$ to the r.h.s of Equation 2.40, the sign of which implies generally descending (ascending) air on EEs (MEs) whilst in the GS domain MABL. This is consistent with the respective number of trajectories exiting the domain through the boundary layer top, 0.32% of trajectories on EEs, but 26.2% on MEs. This term is generally considered a “conversion” term between thermal and mechanical energy, and is in many cases assumed to be negligible. Calculation of the heat budget here has shown the magnitude of the term to indeed be small ($\sim 5-7\%$), but nevertheless that it can be as important as several other factors. In particular, especially on EEs, the average value of

this term is for the most part larger than expected radiative heating within the boundary layer.

2.6 CONCLUSIONS

In this chapter, the direct thermal interaction between the Gulf Stream and the overlying MABL has been examined. A GS domain was defined with the purpose of capturing the region of maximum ocean-atmosphere heat exchange and an associated latent heat flux index over this domain was created for a period of thirty-three winter seasons (1979-2011 DJF). The average total heat flux over the GS domain is 282.67 Wm^{-2} , which is slightly higher than the value on the median days (MEs) based on our GSI which is 258.93 Wm^{-2} . On the top 1% of GSI-defined days (EEs), the domain-averaged total heat flux exhibits a sharp spike up to 766.64 Wm^{-2} , underlining the discreteness of intense heat flux events that are consistent with similar studies (e.g. Shaman et al. 2010). In Section 2.3, a Lagrangian trajectory model was developed with the intention of analysing the differences in the effects of the GS on the overlying MABL between EEs and MEs. Driven by previous results on the synoptic activity associated with intense heat fluxes over the GS (Alexander and Scott, 1997, Zolina and Gulev, 2003), a developing Eady (baroclinic) wave was used to test the LTM theoretically, which proved accurate over $3\frac{1}{4}$ -day back- and forward-trajectory simulations.

In Section 2.4, it was shown that EEs are associated with intensely cold dry air behind cold fronts in passing atmospheric waves. Such synoptic systems cause an almost complete exchange over the GS domain from marine to North American continental air, resulting in large heat ocean heat loss and a correspondingly significant increase in the thermal energy of the overlying MABL.

On the EEs themselves, there is a large downward anomaly in the overlying tropopause depth over the GS domain, as could be expected in a region experiencing strong cyclogenesis. Across the same region, there is a sharp spike in the boundary layer height also, which would result in a significant reduction in the free troposphere. On MEs, there are no comparable anomalies in surface pressure, tropopause height or boundary layer height. There is still a large marine-continental exchange in air masses, but a reasonable fraction of air originates over the ocean. This results in warmer and more moist air over the GS domain, leading to reduced heat fluxes in the region. Nevertheless, the surface heat fluxes are large enough to still cause a significant increase in the temperature, moisture and energy of the overlying air. After interaction with the GS, parcels on EEs and MEs travel both north and south, with parcels travelling polewards rising swiftly and experiencing expected reductions in temperature and moisture. In comparison, those that travel equatorwards however maintain relatively similar atmospheric properties.

The GS domain MABL heat budget was examined in Section 2.5. It was shown that for both EEs and MEs, radiative heating offers a negligible contribution to the heat budget, whilst surface heat fluxes dominate overwhelmingly. In fact, on EEs, the increase in thermal energy in the MABL is almost entirely accounted for by surface heat fluxes, with negligible entrainment flux. Extremely few trajectories exit through the boundary layer top. On MEs, the average time spent by trajectories in the GS domain MABL heat budget is roughly 30% longer than on EEs, however the increase in MABL thermal energy is roughly similar. On these days however, there is a reasonable contribution from entrainment flux (roughly 17%). There is also a noticeable contribution on both days of extreme and median surface heat from the conversion term involving change of pressure within the MABL, highlighting the impact of strongly descending and

ascending air above the GS on the thermal energy in the MABL. At 12:00 UTC on EEs (MEs), the surface latent and sensible heat fluxes contribute a total power (area of GS domain roughly $1.25 \times 10^{12} \text{m}^2$) of roughly 0.96PW (0.32PW). Given that the peak in global poleward heat transport is roughly 6PW (Trenberth and Caron, 2001), surface heat fluxes over the Gulf Stream region alone cause a direct thermal increase in the overlying MABL air whose magnitude is significant on a global scale.

As a final note, it is reiterated that the EEs and MEs considered in this chapter are based on analysis of surface latent heat fluxes accumulated from 12:00UTC to 15:00UTC. Considering that over the GS, this is in the early morning, the air travelling off the continent will naturally be colder and drier than in the afternoon, e.g. 00:00UTC (although it will still be relatively cold and dry then as it is the winter season). However, as mentioned in Section 2.2.2 the diurnal cycle in surface latent heat flux over the GS in DJF is relatively small. This suggests that over time the source of the high heat flux events will not change depending on the time of day, nor will there be any significant numerical effect on our previous calculations either. Nevertheless, redefining our EEs and MEs based on heat fluxes in the late afternoon may have the effect of reordering the indices in our GSI. Whilst it has been argued here that this should not affect the main conclusions of this chapter, numerical estimation of any changes can not be given, and this represents a limitation to the current analysis.

CHAPTER 3

THE CONTRIBUTION OF EXTREME EVENTS TO THE MEAN ATMOSPHERIC STATE IN THE GULF STREAM REGION IN WINTERTIME

3.1 INTRODUCTION

Extremes in ocean-atmosphere heat fluxes over the GS region have associated with them synoptic atmospheric variability (Shaman et al. 2010, Alexander and Scott 1997). Indeed, in Chapter 2, the most extreme in heat flux events over our GS domain occurred with the passing of a cold front in a strong cyclone. Such cyclones strongly intensify over the GS (Cione et al. 1993), a region characterized by strong oceanic frontal zones (i.e. strong SST gradients). The influence of strong SST gradients associated with WBCs in the entire troposphere has been previously discussed. In particular, the annual mean surface pattern in precipitation is found to meander with the GS (Minobe et al., 2008), a pattern that significantly weakens with the horizontal smoothing of the sea-surface temperature (SST) gradient. Similarly meandering patterns of surface wind convergence show a high correlation with the Laplacian of sea-level pressure, suggesting the significance of a pressure adjustment mechanism (Lindzen and Nigam, 1987) due to SST forcing. This meandering pattern of wind convergence is found

throughout the entire troposphere, from which a deep atmospheric response to the mean state over the GS is hypothesized.

Such a mechanism, however, does not take account of the strong weather systems that frequently propagate across the region. Indeed, extratropical cyclones and their associated frontal systems are known to be related to heavy precipitation events (Catto and Pfahl, 2013). In fact, extratropical cyclones contribute approximately 60% of all precipitation north of 30N, with this figure exceeding 80% in DJF in the NA storm-track regions (Hawcroft et al, 2012). In addition, local surface wind convergences in the presence of such cyclones are known (e.g. Palmén, 1958) to be much larger than the mean values presented in wintertime climatologies over the GS (e.g. Kuwano-Yoshida et al., 2010 - in which the same dependencies found in Minobe et al. (2008) are shown for wintertime). Such information suggests an alternative viewpoint from which to interpret the results of Minobe et al. (2008), in which the interaction of the ocean and the atmosphere on days of extreme heat flux, rather than those representative of the mean state, is considered.

It is the aim of this chapter to assess the contribution of extreme events of air-sea heat exchange to the mean atmospheric state in the GS region in wintertime. In Section 3.2, the variation of the surface heat flux with regards to the initial atmospheric state is examined. The contribution of extreme events to the mean pattern in precipitation and to the mean pattern in tropospheric wind divergence is considered in Section 3.3 and 3.4 respectively. In Section 3.5, a novel approach is offered in an attempt to explain the significance of strong oceanic frontal zones in influencing the mean wintertime atmospheric state. Finally, some conclusions are presented in Section 3.6. The heat flux data used in this chapter is as described in Chapter 2.2.1, and unless otherwise stated, all other data is ERA-Interim reanalysis data, used at 1.5° horizontal

resolution, at 12:00UTC.

3.2 THE VARIATION OF SURFACE HEAT FLUX WITH ATMOSPHERIC STATE

In Section 2.4, it was shown that the strongest 1% of daily heat flux events over our GS domain were associated with a passing atmospheric transient in MSLP. The pre-existing baroclinic wave intensifies as it travels over the GS before dissipating with time as it travels over the NA, with the strong heat fluxes located behind the cold front of the low pressure centre. Analogous patterns were not present for the median heat flux events.

Figure 3.1 illustrates the full spectrum of MSLP anomalies across DJF 1979-2011 (with regards to the thirty-three year mean shown in panel (k)) averaged across deciles in our GSI, defined in Chapter 2.2.2, from (a) the bottom ten percent of heat flux events through to (j) the top ten percent (“GSI decile plot type A”). The days within the strongest 30% of heat flux events exhibit a distinct signal analogous to that in Section 2.4. This is consistent with the increase of surface heat fluxes with the passing of cold, dry continental air behind a cyclonic cold front. The lower the pressure of the cyclone centre, the stronger the surface heat fluxes associated with its passing. This would be consistent with stronger winds increasing northerly flow and enhancing the exchange of the cold, dry continental air with the warm, moist ocean air. Conversely, the bottom 60% exhibit a strong signal that is the same in pattern, yet opposite in sign. These days where the GS domain-averaged surface heat flux is relatively weak (but always positive) would therefore appear to be associated with the passing of an anticyclone as opposed to a cyclone. This is confirmed by a +/-1 day lagged composite of MSLP for the bottom decile in GSI in Figure 3.2, which depicts an

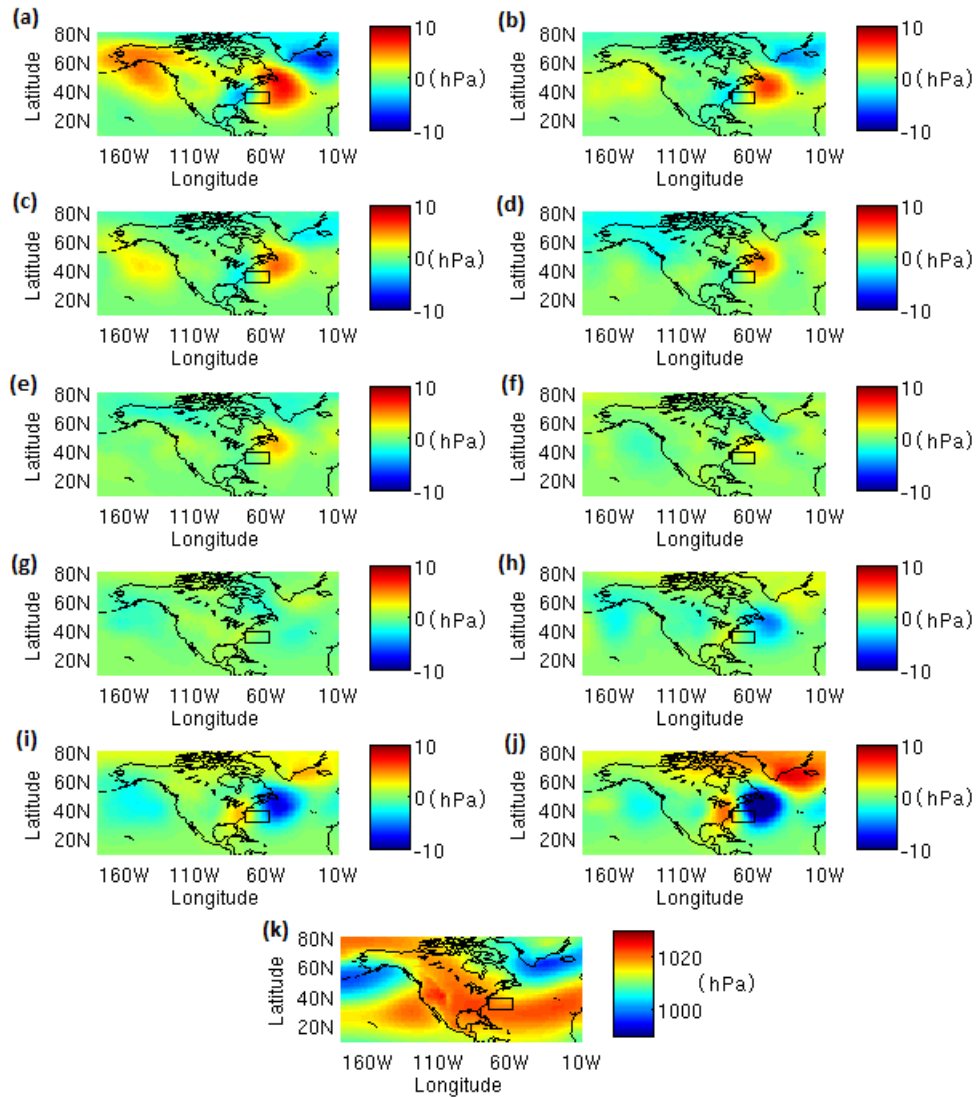


Figure 3.1: Time-mean wintertime anomalies in the mean sea-level pressure, averaged across deciles in the GSI from (a) 0-10% to (j) 90-100%. The thirty-three year average wintertime mean sea-level pressure is shown in (k). The rectangular black box in each plot represents the Gulf Stream domain.

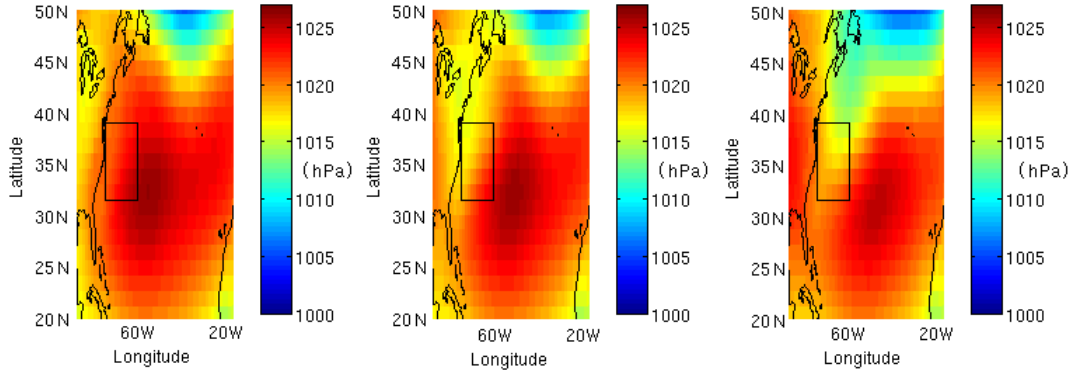


Figure 3.2: Composite of MSLP, averaged across the bottom 10% in the GSI, with a lag of (i) -1 (ii) 0 (ii) + 1 days.

eastward propagating high pressure centre located to the east of the GS domain. In a similar manner, the higher the pressure of the anticyclone centre, the weaker the GS domain-averaged surface heat flux associated with its passing. It is also noted that there is only one decile (60-70%, Figure 3.1 (g)) where there is no appreciable atmospheric anomaly. A consequence of this is that the mean state in MSLP over the GS region is primarily determined by two opposite regimes of passing low and high pressure anomalies. In addition, the decile exhibiting no appreciable atmospheric anomaly is not the median in heat flux, which suggests a bias exists towards extreme events in setting the mean state over the GS region. Furthermore, given that the GS region is an intense region of cyclogenesis, and that these pressure anomalies exist $\sim 90\%$ of the time, such a result appears to be consistent with the concept of a baroclinic waveguide (i.e. a continuous series of cyclonic/anti-cyclonic systems) constantly propagating across the GS (e.g. Chang et al. 2002). Indeed, a strengthening region of low pressure can be found trailing the eastward propagating anticyclone in Figure 3.2. This idea is considered further in Sections 3.3 and 3.4.

Figure 3.3 illustrates a ± 1 day lagged composite of tropopause depth and

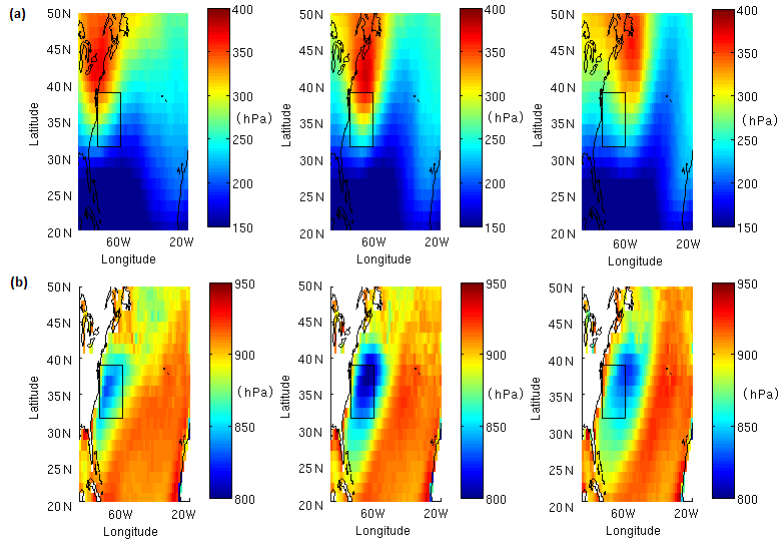


Figure 3.3: Composite of (a) the tropopause depth and (b) the boundary layer height, averaged across the top 10% in the GSI, with a lag of (i) -1 (ii) 0 (iii) +1 days.

boundary layer height for the top 10% decile in GSI. These variables are associated with the baroclinic wave and as with MSLP, pre-existing maxima (tropopause depth ~ 400 hPa, boundary layer height ~ 800 hPa) travel and intensify across the GS domain. Plotted in Figures 3.4 and 3.5 are GSI decile plots for tropopause depth and boundary layer height. A similar pattern to Figure 3.1 can be seen, with deeper (shallower) tropopause depth and boundary layer height associated with stronger (weaker) surface heat fluxes. Again, a bias towards extreme events is suggested.

These results imply that ocean-atmosphere heat fluxes over the GS are wholly dependent on the strength of the passing atmospheric transient, and that the mean state over the GS region is determined by two extreme and opposite regimes. Given the dynamical significance of these variables, it is reasonable to hypothesize that the mean atmospheric state over the GS after the passing of the anomalies could also be determined by such extremes. This is

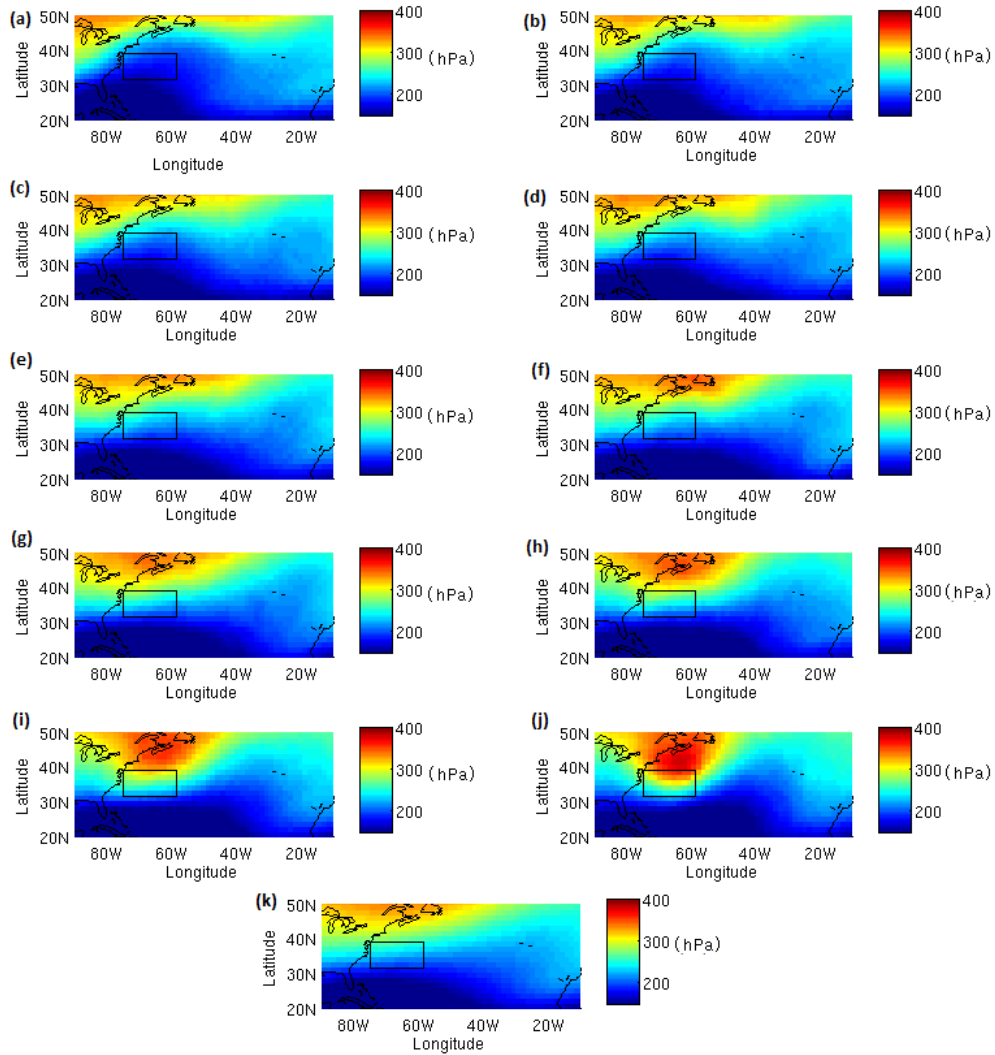


Figure 3.4: Tropopause depth, averaged across deciles in the GSI from (a) 0-10% to (j) 90-100%. The thirty-three year average wintertime tropopause depth is shown in (k). The rectangular black box in each plot represents the Gulf Stream domain.

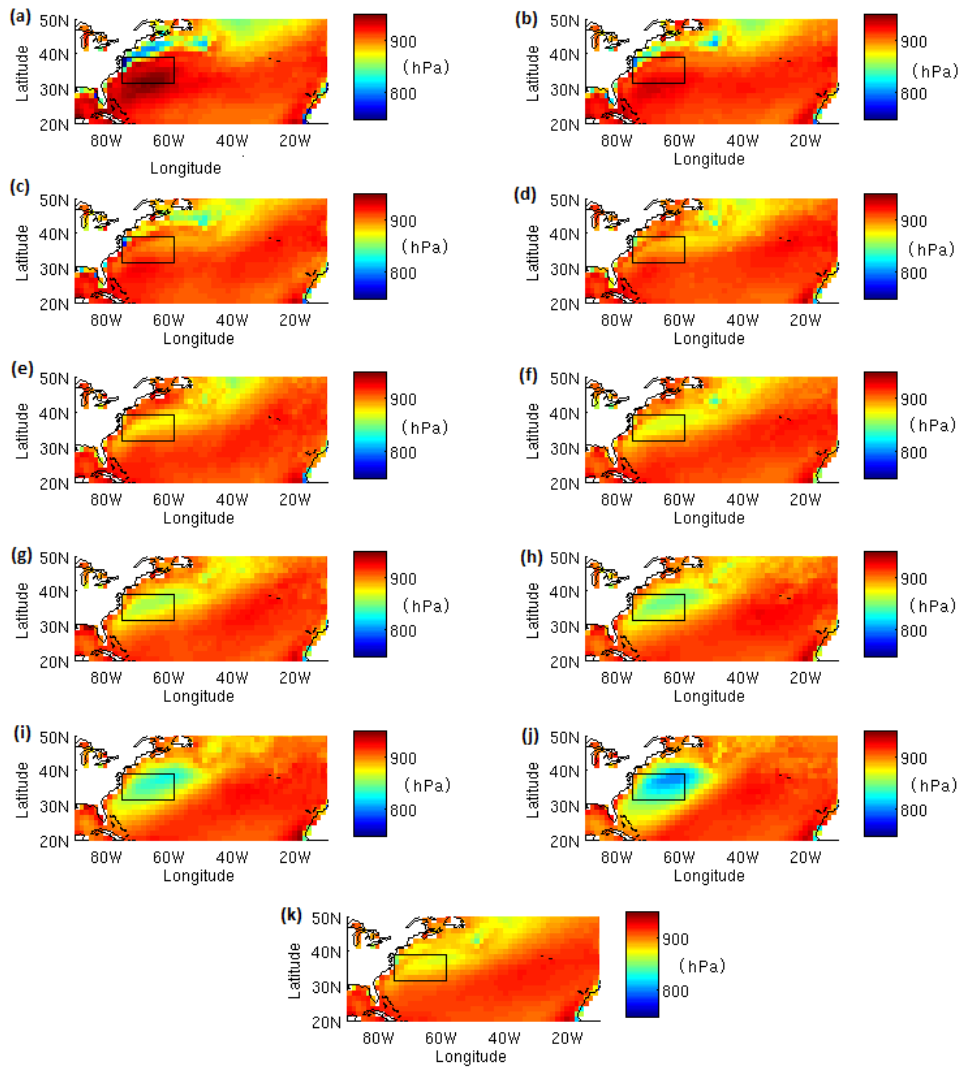


Figure 3.5: As in Figure 3.4, but for the boundary layer height.

now specifically addressed by looking first at precipitation in Section 3.3, then at tropospheric wind divergence in Section 3.4.

3.3 THE CONTRIBUTION OF EXTREMES TO THE MEAN PATTERN IN PRECIPITATION OVER THE GULF STREAM

It is noted at the outset of this section that both convective and large-scale precipitation are not analysed fields, and are hence taken from short-range forecast accumulations in the same manner as the surface heat flux fields (c.f. Chpt. 2.2.1). Consequently, both fields also suffer from spin-up. For the total precipitation, the 20-year average (1989-2008) of the difference between precipitation forecasts 24h-36h and 00h-12h is shown to be $\sim 0.5 \text{mm day}^{-1}$ in the mid-latitude storm track regions (Källberg, 2011). Whilst this represents a larger fraction of the GS precipitation mean than the associated spin-up fraction for the total heat flux, the relative error still falls within reason (e.g. compared to a total precipitation mean of $\sim 4\text{-}8 \text{mm day}^{-1}$ as in Minobe et al. (2008)).

Figures 3.6 and 3.7 illustrate “GSI decile type B” plots of the convective and large-scale precipitation respectively, where parts (a)-(j) are now the weighted contribution of each decile to the mean state (k). That is to say that the sum of the daily values across a specific decile in GSI is now divided by the total 33-year DJF period, rather than just the decile itself (as in Figure 3.4, for example). A consequence of this is that the sum across (a)-(j) is equal to the total mean in (k). (Indeed, the mean value across each decile can be subsequently calculated anyway by simply multiplying by 10). The mean state of the convective precipitation appears to be consistent with the hypothesis in Minobe et al. (2008) that the mean total precipitation is set by the relative pressures on

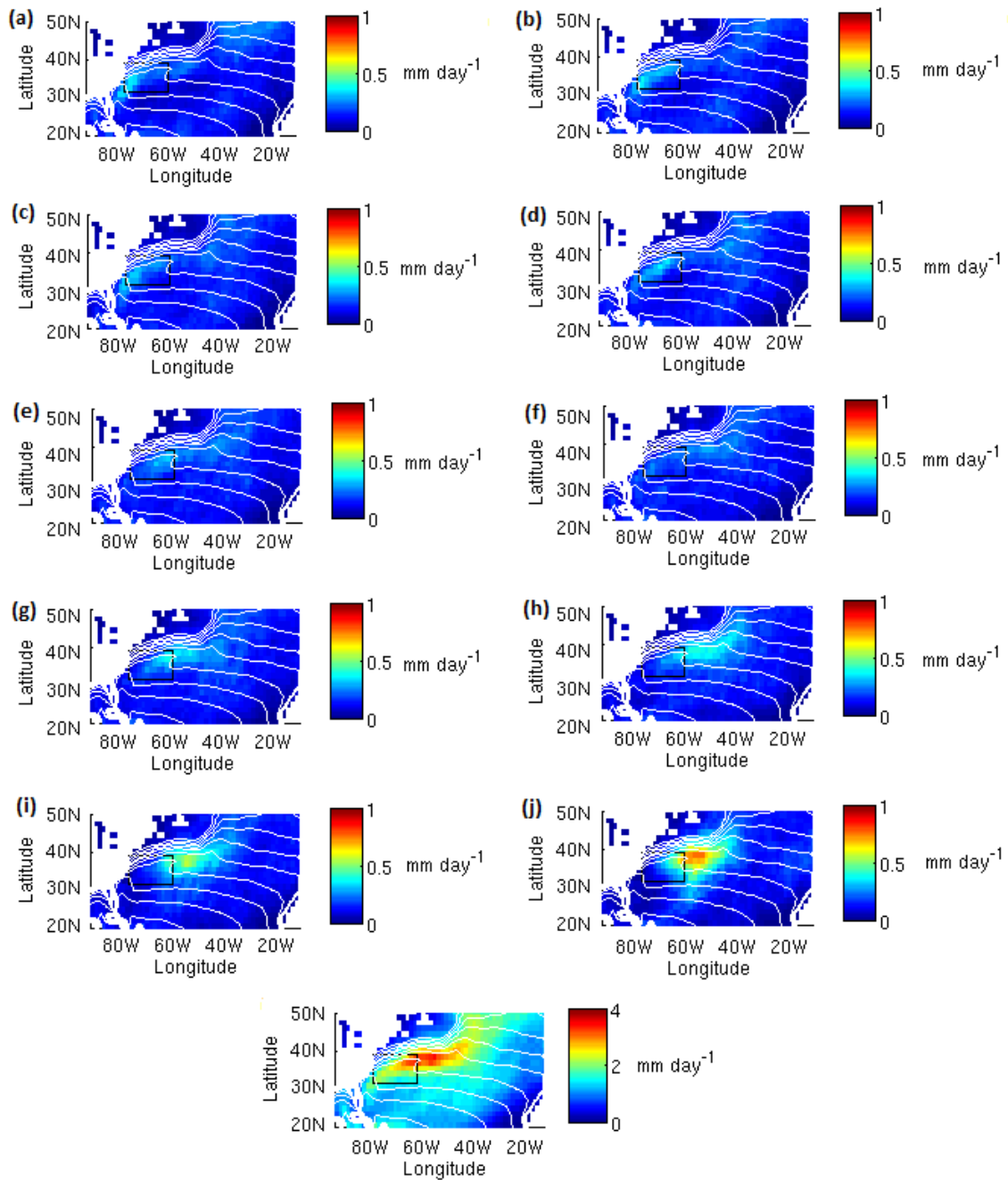


Figure 3.6: Contribution of each decile in GSI, from (a) 0-10% to (j) 90-100%, towards the thirty-three year average wintertime convective precipitation (k). Sea-surface temperature contours from 8°C to 26°C at intervals of 2°C are marked in white. Continental grid points are marked out in white.

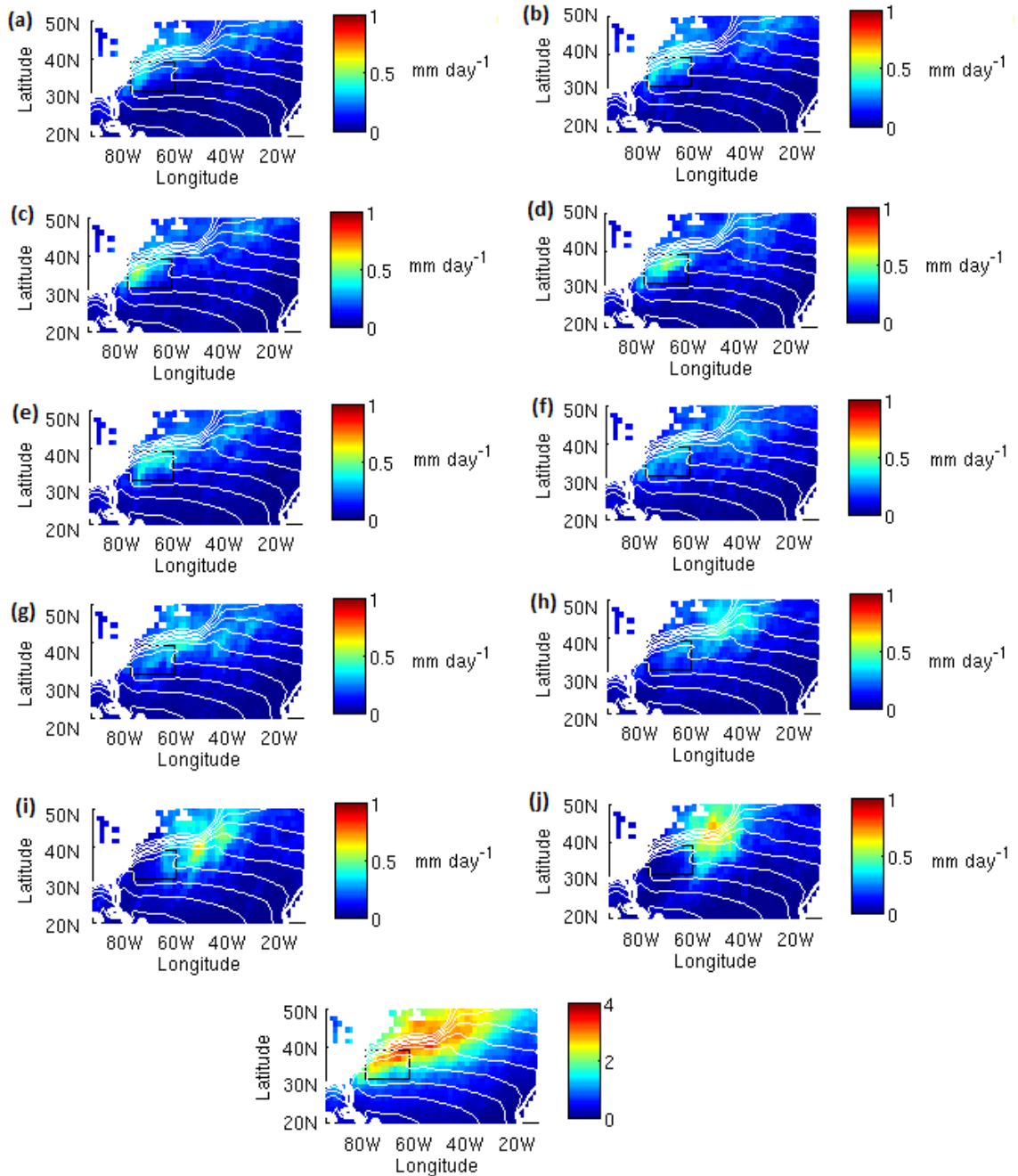


Figure 3.7: As in Figure 3.6, but for the large-scale precipitation.

either side of the GS front anchoring upward motion and enhancing local precipitation. However, the smooth meandering pattern of convective precipitation is noticeably different for the top 30% and bottom 60% of GSI heat flux days. These observations are also true for the large-scale precipitation, and in both cases the weighted contribution of the extreme ends in surface heat flux events are the largest locally in their precipitation.

Given the results of the previous section, it appears that the mean precipitation is in fact determined primarily by atmospheric transients (i.e. cyclones and anticyclones) that pass over the GS. Once again, there is only one decile (g, 60-70%) in either case that closely resembles the pattern of the mean (k), and there are two opposite regimes present. On those days associated with the passing of a cyclone, there is a localisation of precipitation with the low pressure centre, whilst on those days associated with the passing of an anti-cyclone, the local maximum in precipitation is found to the west of the GS domain, where one finds a developing low-pressure centre in Fig 3.1(a)-(f). Indeed, this precipitation maximum is expectedly less than those found in cyclones to the east of the GS domain, that will have picked up moisture as they travelled across the warm underlying ocean currents (hence giving rise to the strong latent heat fluxes).

The precipitation found in the trailing cyclone is further evidence of a baroclinic waveguide introduced in Section 3.2, and the +/-2-day lagged composite of total (convective and large-scale) precipitation shown in Figure 3.8 for the weakest 10% in GSI shows the intensification in precipitation rate which is consistent with a developing low pressure (Fig 3.1(a)) as the cyclone travels across the GS domain. Indeed, the pattern found for a lead of +1 day in Figure 3.8(iv) is similar to that for the strongest 10% in GSI.

The concept of a baroclinic waveguide is further illustrated in Figure 3.9,

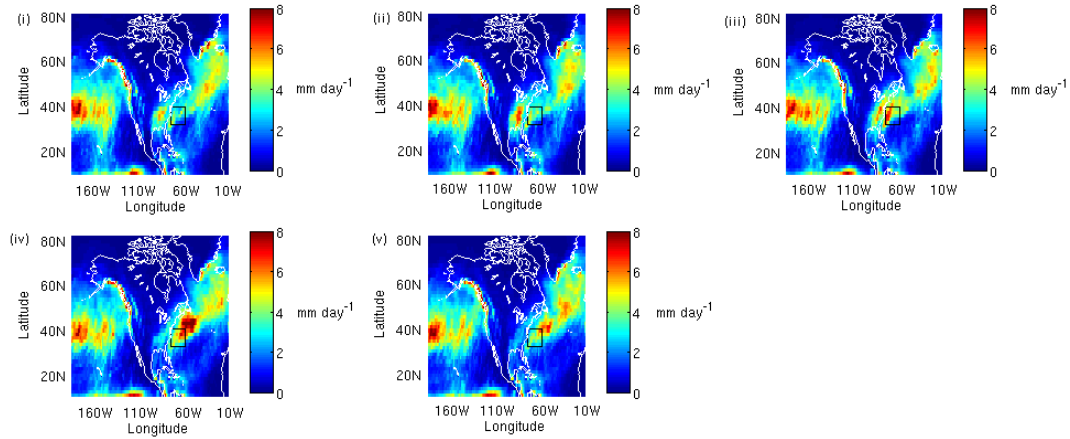


Figure 3.8: Composite of total precipitation averaged across the bottom 10% in the GSI, with a lag of (i) - 2 (ii) -1 (iii) 0 (iv) + 1 (v) + 2 days.

which shows the percentage of precipitation contributed by the (a) weakest and (b) strongest 20% in GSI across the GS region, shown here split into convective and large-scale components to demonstrate their co-location. Up to 50% of the total precipitation is associated with cyclones on each set of these days, with noticeable negative anomalies where one would expect from Figure 3.1 to find an anticyclone. These observations suggest that the mechanism for setting the mean pattern in precipitation is in fact a direct result of the precipitation associated with the baroclinic waveguide.

Figure 3.10 shows again the twenty-year wintertime mean of the (a) convective precipitation and (b) large-scale precipitation, but now with an additional domain (42-64.5W,33-43.5N), larger than the GS domain and chosen to represent a region which experiences a relatively large amount of rainfall on average. Across the twenty winter seasons, this domain experiences a total of 825m of convective precipitation and 859m of large-scale precipitation. On the top 10% of GSI days, this region experiences 154m of convective precipitation and 137m of large-scale precipitation, which represents 19% and 16% of the totals respec-

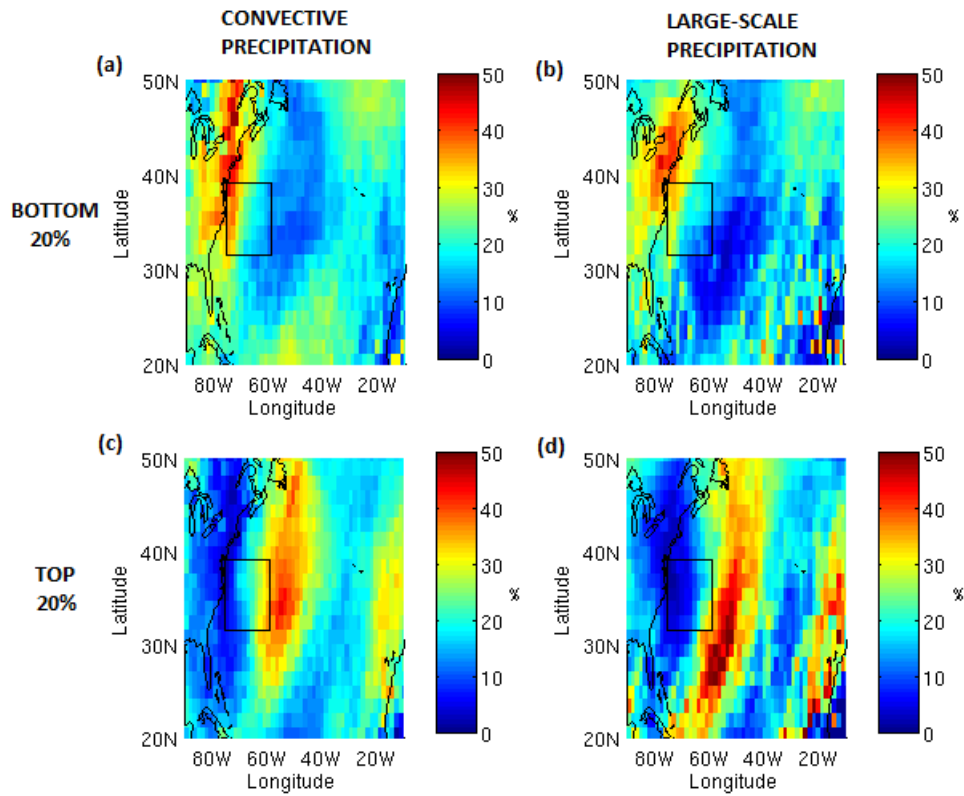


Figure 3.9: The relative percentage contribution of (a) the bottom 20% and (b) the top 20% in GSI towards the convective and large-scale precipitation in the GS region.

tively. On the top 20% of GSI days, these values increase to 268m (32%) and 257m (30%) respectively. As the region is fairly broad, these percentages are expectedly not as large as those that can be found locally in Figure 3.9; however, the numbers still illustrate a general bias towards the days of extreme heat flux in contributing to the total rainfall over the GS.

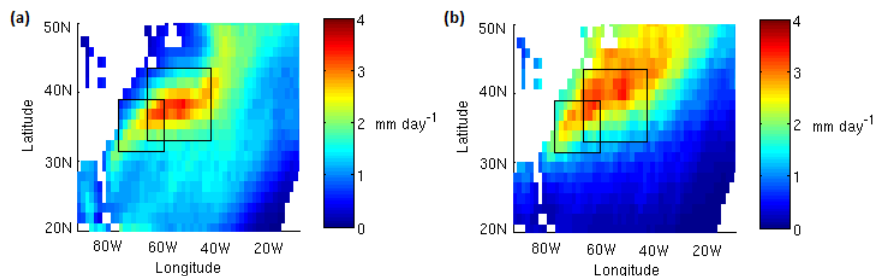


Figure 3.10: Twenty-year wintertime mean of (a) convective precipitation and (b) large-scale precipitation, showing both the GS domain and the domain (42-64.5W,33-43.5N).

3.4 THE CONTRIBUTION OF EXTREMES TO THE MEAN PATTERN IN TROPOSPHERIC WIND DIVERGENCE OVER THE GULF STREAM

Another important result presented in Minobe et al. (2008) was the apparent influence of the GS deep into the troposphere, with mean patterns in upper-tropospheric wind convergence and divergence found to meander with the near-surface mean.

Figure 3.11 illustrates a “GSI decile type B” plot for wind divergence at 950hPa (i.e. near-surface). As has been the case for MSLP and convective and large-scale precipitation, the mean pattern (k) is only recovered in the 60-70% decile (g). Above this decile ((h)-(j)), increasing ocean-atmosphere heat fluxes are associated with the passing of stronger cyclones and thus stronger regions of convergence in the warm sector east of $\sim 70W$, and divergence behind the trailing cold front. As before, the reverse holds true for lower deciles ((a)-(f)), with the presence of an anticyclone east of $\sim 70W$ and wind convergence west of $\sim 70W$ associated with a trailing cyclone’s warm sector. Again, in terms of

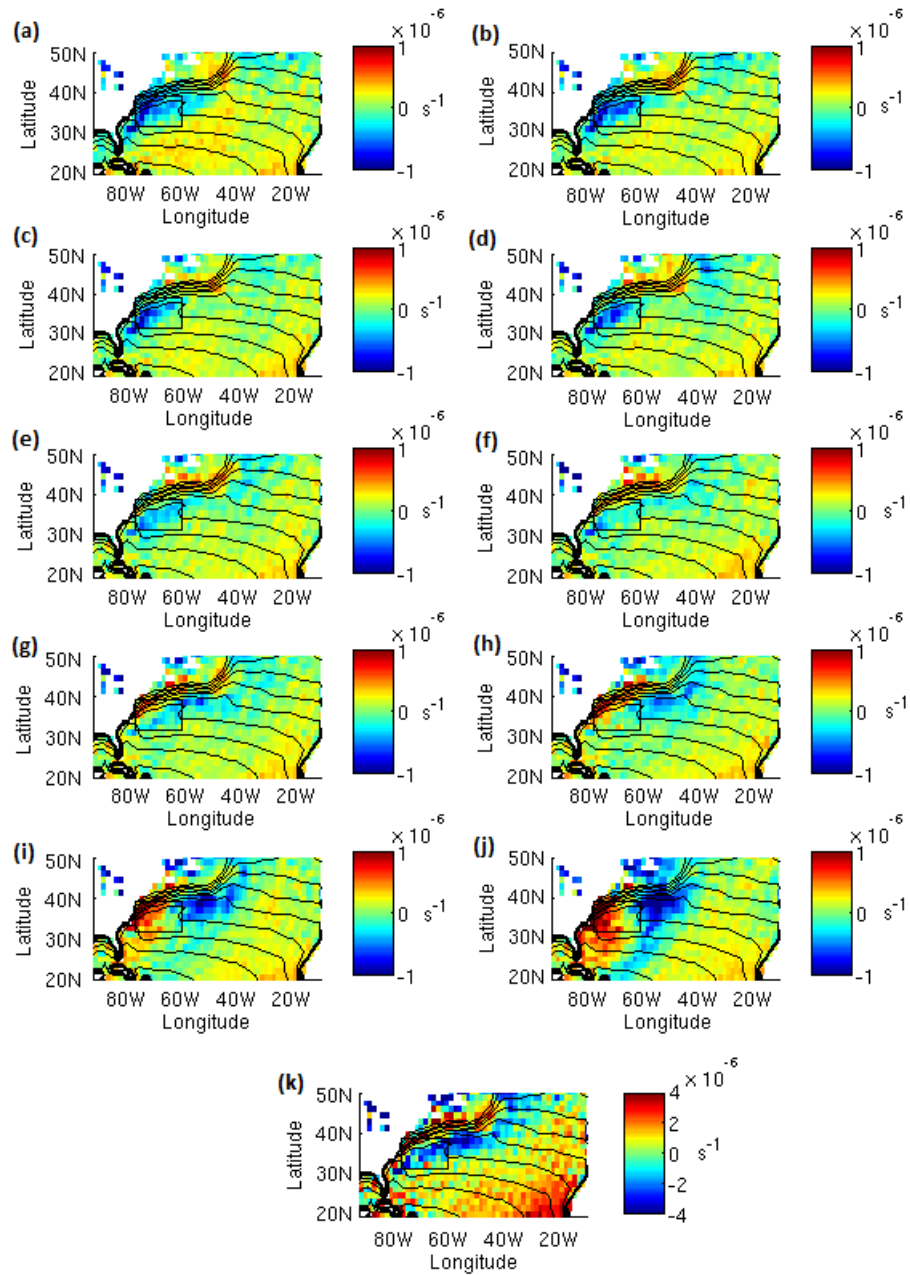


Figure 3.11: Contribution of each decile in GSI, from (a) 0-10% to (j) 90-100%, towards the thirty-three year average wintertime wind divergence at 950hPa (k). Sea-surface temperature contours from 8°C to 26°C at intervals of 2°C are marked in black. Continental grid points are marked out in white.

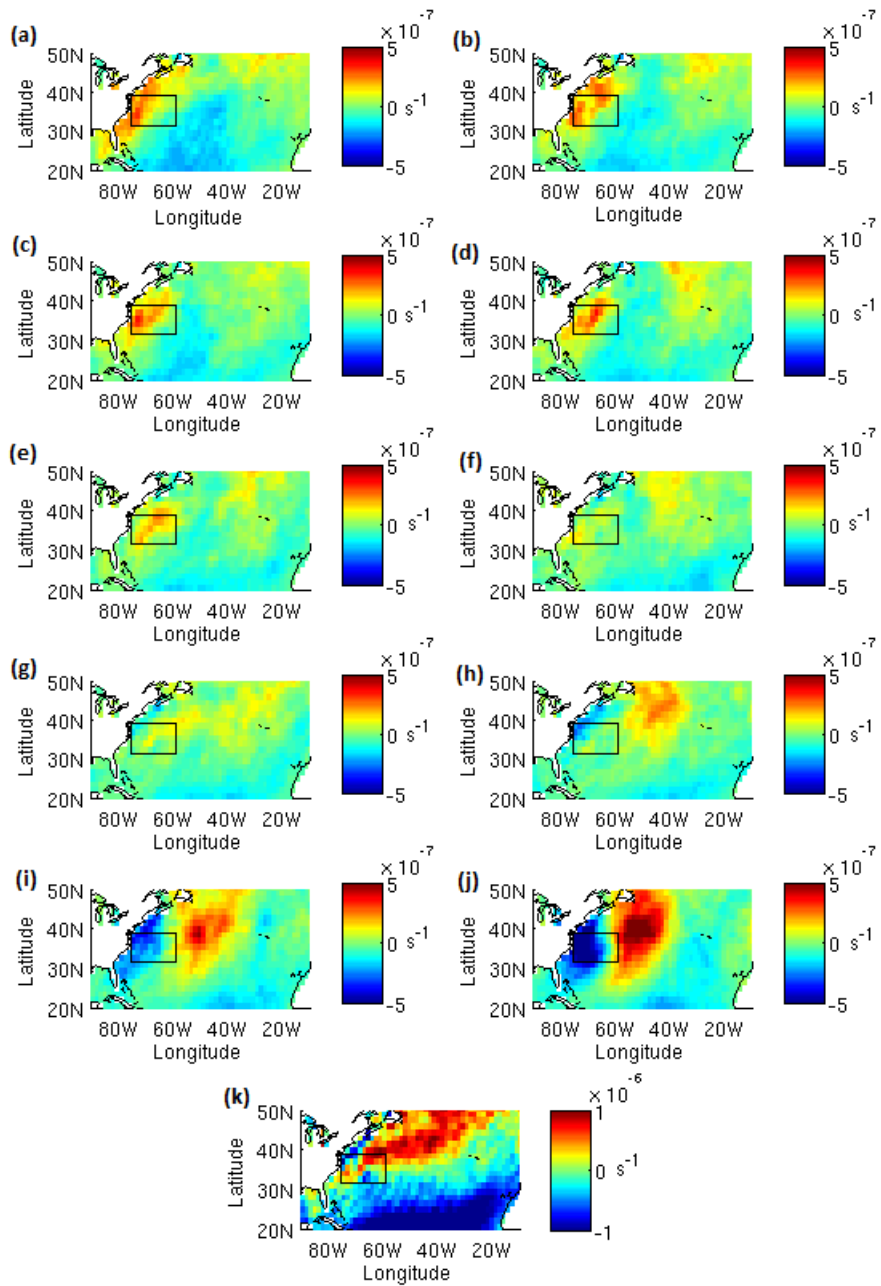


Figure 3.12: Contribution of each decile in GSI, from (a) 0-10% to (j) 90-100%, towards the thirty-three year average wintertime upper-level (500hPa-200hPa averaged) wind divergence (k). Sea-surface temperature contours from 8°C to 26°C at intervals of 2°C are marked in black. Continental grid points are marked out in white.

contribution to the mean, a noticeable bias exists towards the strongest 30% of heat fluxes ((h)-(j)). Furthermore, these decile trends are exactly imitated in the upper-level troposphere, albeit with a reversal of sign. This can be seen in Figure 3.12, which presents a “GSI decile type B” plot for 500hPa-200hPa averaged wind divergence. It would therefore appear that the pattern in upper-level tropospheric wind divergence over the GS is also dominated by the top 30% of heat flux events. Given the association of these days with the passing of a strong cyclone, it would be consistent for the connection between the low- and upper-level wind divergence over the GS to be directly related to the convective and large scale ascent/descent expected within a baroclinic wave. It is also noted that south of the GS, equatorwards of 30N, the region of seemingly unnoticeable convergence evenly distributed in each decile adds up to an area of mean convergence on the same order of magnitude as the mean divergence located above the GS itself.

Figure 3.13 illustrates a “GSI decile type B” plot for the low-level (950hPa) vertical wind. Indeed, the vertical velocity is related to the wind divergence by the continuity equation $\omega + (\frac{\partial u}{\partial x} + \frac{\partial v}{\partial y}) = 0$, where $(\frac{\partial u}{\partial x} + \frac{\partial v}{\partial y})$ is the divergence. As expected, present on days of extremely strong surface heat flux are regions of strong upward (downward) motion, that are exactly collocated with regions of low-level convergence (divergence), and that dominate the mean pattern. These strong areas of ascent and descent are even more pronounced at mid-levels of tropospheric pressure, as shown in Figure 3.14, which illustrates +/-2 day lagged composites of vertical velocity anomalies (defined as in Figure 3.1) at 500hPa for (a) the top 10% in GSI and (b) the bottom 10% in GSI. In both cases, each anomaly appears to once again be associated with a continuous baroclinic waveguide. This figure also demonstrates that the vertical velocities present on extreme GSI days are far larger than the wintertime average.

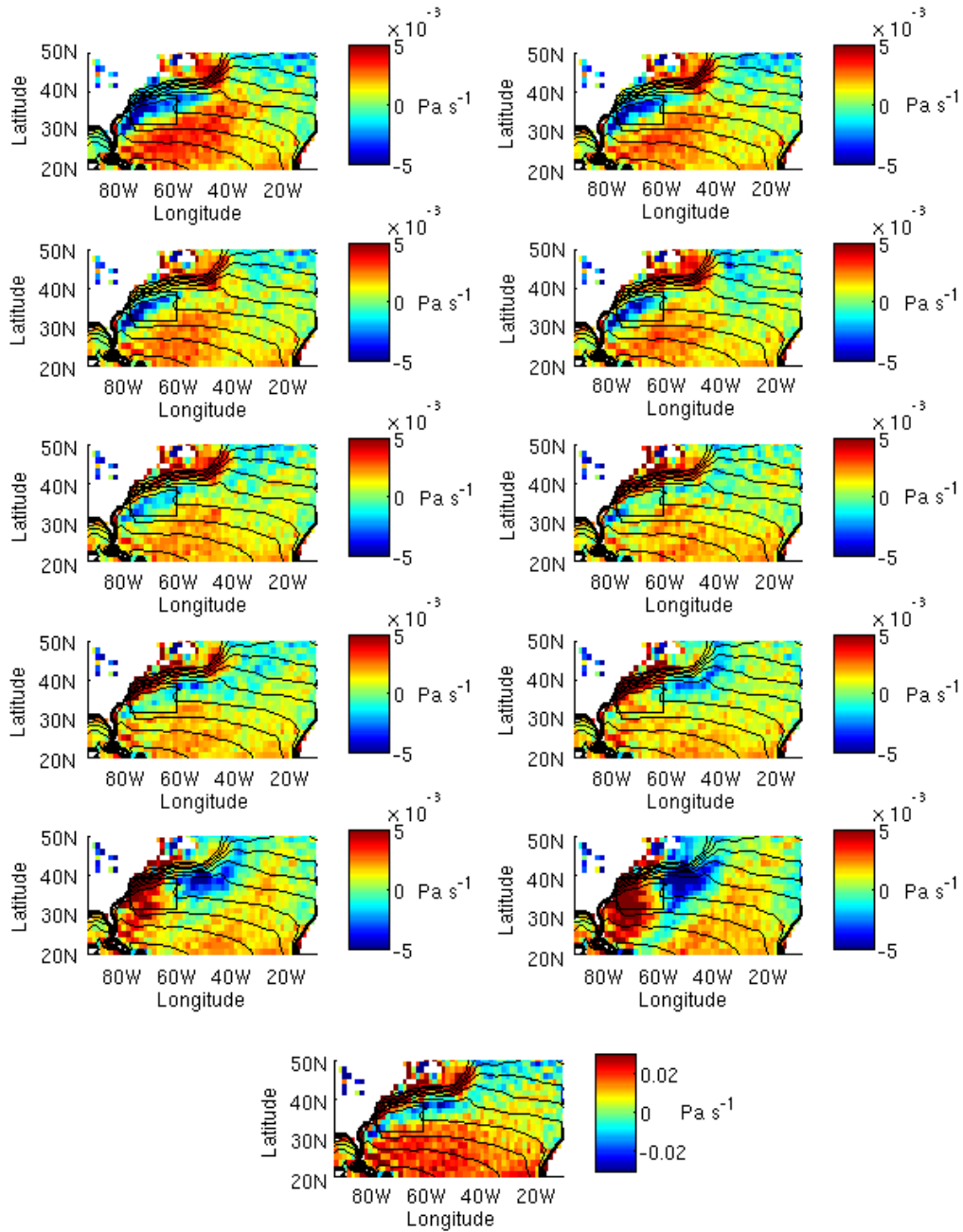


Figure 3.13: As in Figure 3.10, but for the vertical velocity at 950hPa.

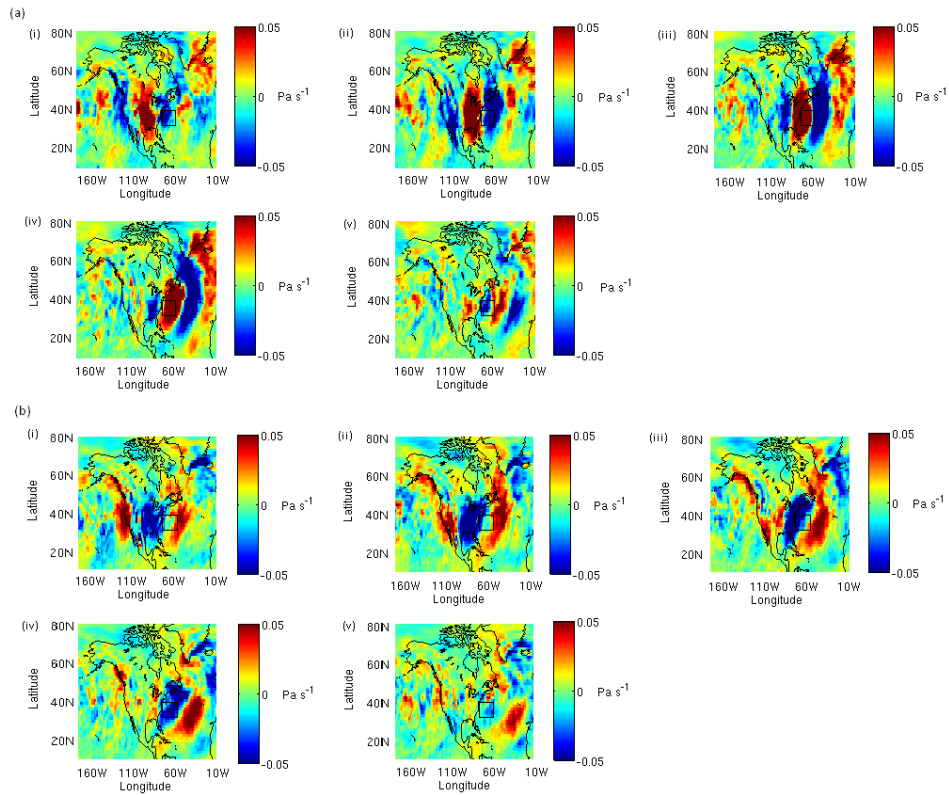


Figure 3.14: Composites of vertical velocity time-mean anomalies averaged across (a) the top 10% and (b) the bottom 10% in the GSI, at 500hPa, with a lag of (i) - 2 (ii) -1 (iii) 0 (iv) + 1 (v) + 2 days.

3.5 ATTEMPTING TO UNDERSTAND THE INTERACTION OF THE GULF STREAM FRONT WITH SYNOPTIC ATMOSPHERIC TRANSIENTS

In the previous sections, it has become clear that the mean wintertime state in precipitation and vertical velocity throughout the troposphere over the Gulf Stream is primarily determined by the passing of synoptic storms. This mean wintertime atmospheric state is intimately connected to the GS front, to the extent where the pattern of precipitation that seemingly meanders with the front disappears with its removal (Kuwano-Yoshida et al., 2010). In this section, a novel approach is explored for EEs (as defined in Section 2.2) in an attempt to offer a potential explanation for these results.

Given the discrete nature of extreme heat flux events, it is a challenging task to analyse long periods of data in order to figure out the mechanism of specific interactions. Results of case studies can vary significantly and also be influenced by neighbouring systems, making it difficult to understand whether the conclusions are generic or not. On the other hand, composites can be used to study an average representative cyclone. However, the method of compositing can smooth out individual cyclone features like fronts and rainbands, which can make it hard to study the processes driving an individual interaction. Here, we will attempt to address this problem by creating a composite centred on the cyclones location, using a proxy in maximum tropopause depth. It is necessary first however, to analyse a standard composite across EEs of the tropopause depth, as shown by the contours in Figure 3.15. Also shown in colour is the boundary layer height, and marked in black is the GS domain. Based on these

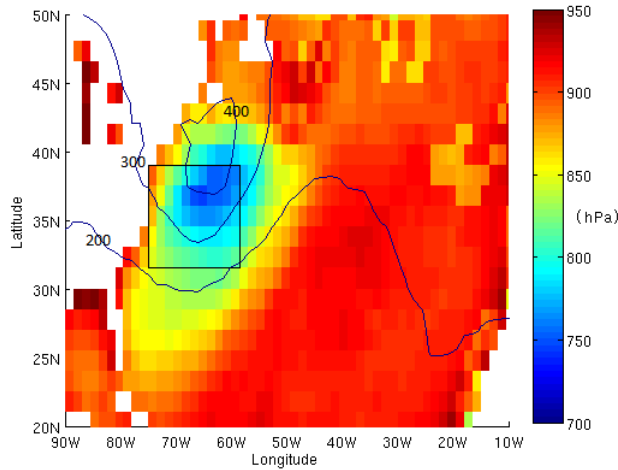


Figure 3.15: Composite of tropopause depth (contour) and boundary layer height (colour) in the GS region, averaged across EEs.

contours, a constant latitude of 37.5° is chosen on which to use our proxy.

At this latitude, for each of the EEs, the longitude of maximum in tropopause depth is located within the GS domain. A plot of meridional (positive northward) and vertical (positive downwards) velocity is then made for each EE for twenty grid points (i.e. $20 \times 1.5^\circ$) either side of this grid point, and then a composite average made over all the EEs. This is shown in Figure 3.16(c) and (d) respectively. This is repeated for a lag of one day ((a),(b)), and a lead of one day ((e),(f)). As can be seen, for these events the proxy in tropopause depth works well; basic features of the eastward propagating cyclone (that can be clearly shown using the Eady model - ref. Chapter 2.3.3) are clearly picked out, such as the westward tilt of the cyclonic circulation with height, and ascent (descent) ahead (behind) of the low centre. It is noted that the surface low centre is at roughly $+5$ grid points at lag zero.

Figure 3.17 illustrates a similar composite, but lagged, and for the atmospheric Ertel-Rossby potential vorticity ((a) lag one day, (b) lag zero and (c) lead one day). Plotted in black are the tropopause and the boundary layer top,

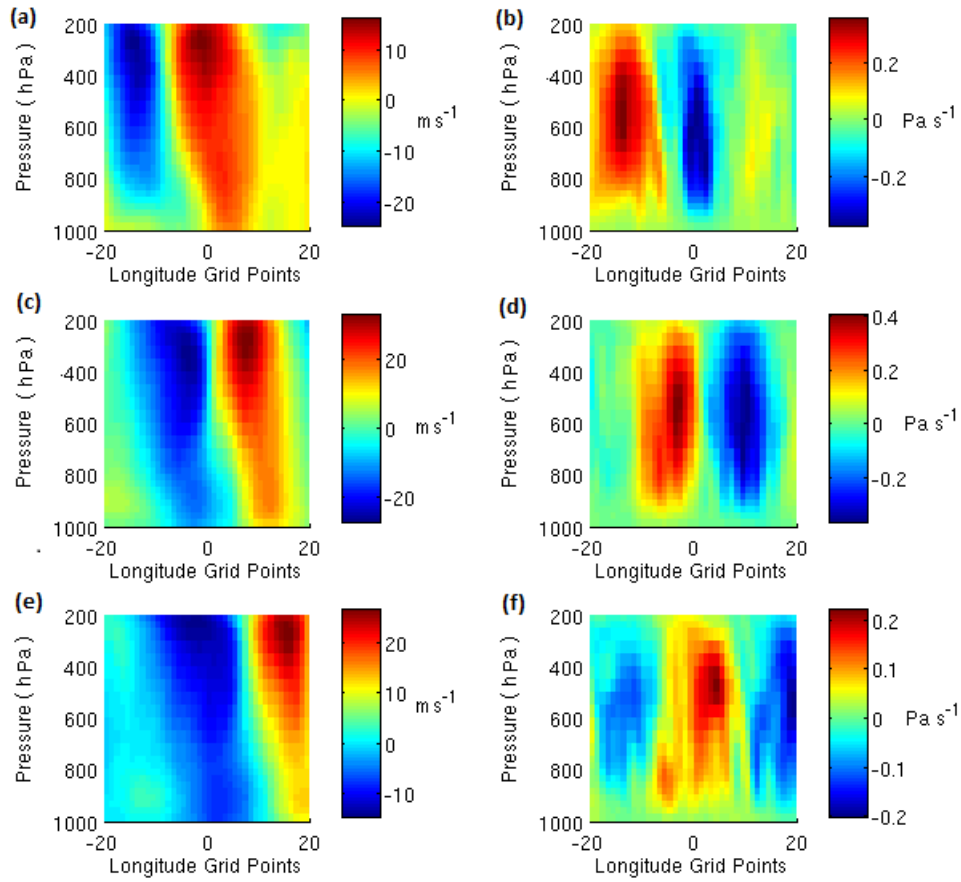


Figure 3.16: Longitudinal composites of meridional ((a),(c),(e)) and vertical velocity ((b),(d),(f)), averaged across EEs with each day centred on the maximum in tropopause depth at constant latitude 37.5° , with a lag of ((a),(b)) -1, ((c),(d)) 0, ((e),(f)) +1 days.

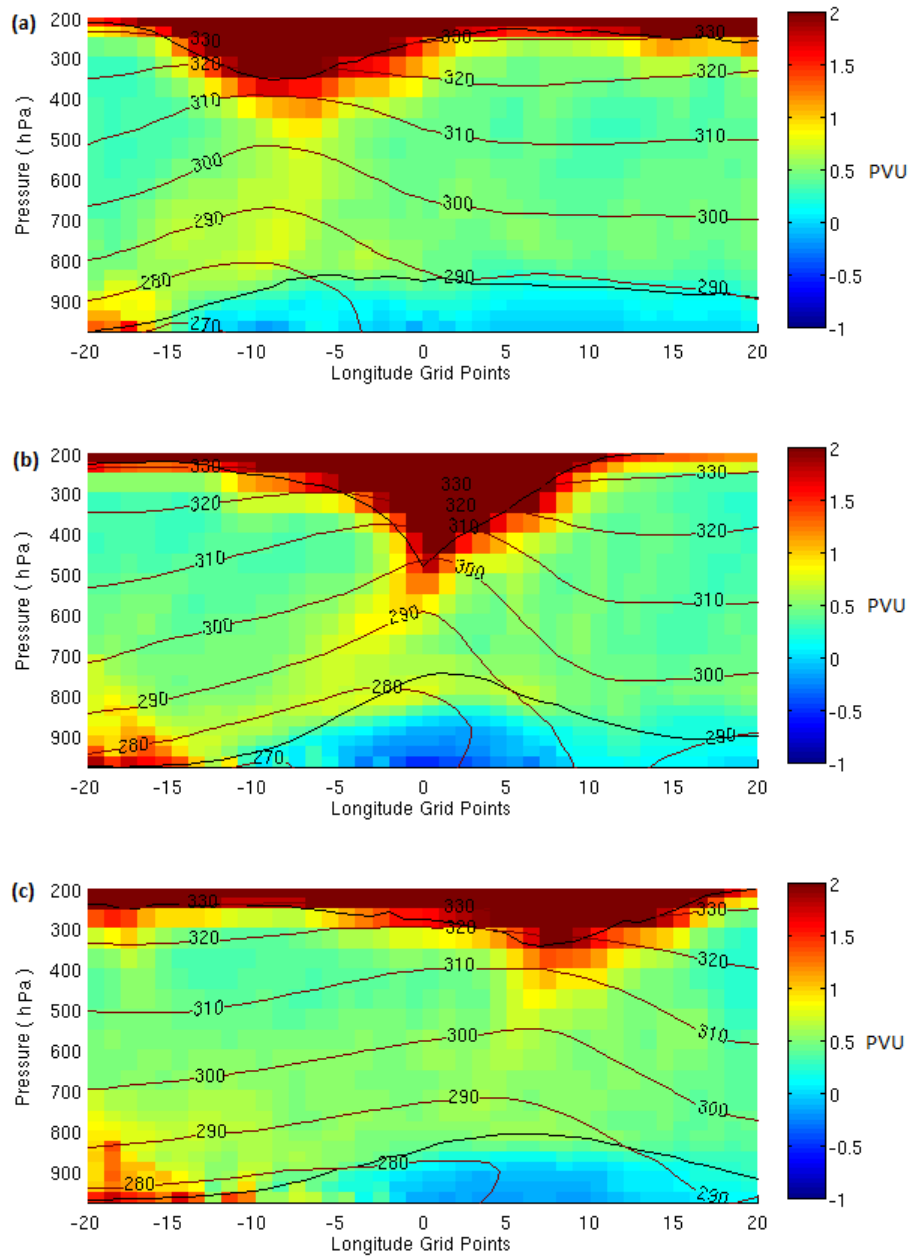


Figure 3.17: Longitudinal composites of atmospheric potential vorticity, averaged across EEs with each day centred on the maximum in tropopause depth at constant latitude 37.5° , with a lag of (a) -1, (b) 0, (c) +1 days. The tropopause and the boundary layer top are represented by thin black lines and contours of potential temperature are also marked.

and contours in potential temperature are marked also. As expected from the proxy and the definition of the tropopause height (line of 2PVU), we observe a deep anomaly in tropopause height, and thus positive PV, that propagates eastward. Across the GS, the boundary layer top is naturally elevated due to the warm current temperatures, however as expected again there is a pronounced spike at lag zero with the passing of the cold front (behind the surface low). Such are the strength of the spikes that at this location, the size of the free troposphere is reduced to $\sim 250\text{hPa}$. Furthermore, co-located with this spike in boundary layer height just below the low centre is a region of negative PV that extends up to $\sim 800\text{hPa}$. Consequentially, the isentropes are heavily distorted in this region. Indeed, where there is strong ascent found to the east of the low centre, there is a potential temperature surface (290-300K) that extends from the surface right up to the tropopause. Figure 3.18, from Hoskins et al. (1985), aids in understanding why this is the case. Figure 3.18(a) illustrates a positive (cyclonic) PV anomaly at the tropopause, which causes a tightening of the isentropes within the anomaly, creating a region of increased static stability. Conversely, a negative (anticyclonic) PV anomaly at the tropopause, as depicted in Figure 3.18(b), causes a loosening of the isentropes, creating a region of decreased static stability. If this negative PV anomaly is located at the surface, this decreased static stability will lead to enhanced upward motion. This in turn will be strengthened by any neighbouring surface positive PV anomaly, which will act to distort the isentropes further, leading to the situation found in Figure 3.17.

It can be seen that with the developing cyclone passing over the GS, there is a noticeable generation of negative PV within the boundary layer behind the cold front. The stronger the presence of negative PV beneath the maximum in tropopause depth, the stronger the isentropes will be distorted and the more

conducive the atmosphere will be to strong vertical motion.

The concept of potential vorticity (PV) as a natural variable for baroclinic systems was introduced in Section 1.2. Within the boundary layer, for motion that is not frictionless and adiabatic, PV can be both created and destroyed via the equation

$$\frac{D(PV)}{Dt} = \frac{1}{\rho} \{ (\nabla \times \mathbf{S}^u) \cdot \nabla \theta + \zeta \cdot \nabla \frac{D\theta}{Dt} \}, \quad (3.1)$$

where \mathbf{S}^u is the frictional force per unit mass. Adamson et al (2006) extended work done by Cooper et al. (1992) and used an idealized three-dimensional baroclinic life-cycle model to find three main processes that affect boundary-layer PV generation.

1. Ekman pumping

For frictionless flow, geostrophic balance means air flows parallel to isobars and cyclonically around a low pressure. However, in the presence of friction, cross-isobaric flow causes flow away from high pressure centres and towards low pressure centres (Ekman, 1905). Within the boundary layer, wind turning towards the low pressure centre results in low-level wind convergence, leading to low-level ascent. This lifts isentropes away from the surface, reducing the static stability, and also leads to a direct reduction of relative vorticity in the region. These processes cause the creation of negative boundary-layer PV.

2. Baroclinic generation

The reduction of horizontal wind from the boundary-layer top to the surface results in large horizontal relative vorticity. Combined with the presence

of frontal regions of a baroclinic wave where there exist large horizontal temperature gradients, frictional turning of the wind causes PV changes that are predominantly positive and concentrated to the east and north-east of a surface low. Such generation requires only baroclinicity and a non-perpendicular alignment of the surface and thermal winds.

3. Surface heat fluxes

In a region of positive absolute vorticity, heat fluxes from the atmosphere into the ocean will reduce the near-surface air temperature, increasing stability and generating positive PV. Conversely, heat fluxes from the ocean into the atmosphere reduce static stability, resulting in the creation of negative PV. The strong negative PV generation found in Figure 3.17 occurs in the cold-sector air to the west of the low centre, which is consistent with the results of Plant and Belcher (2007).

With regards to a cyclone passing over the GS, smoothing the gradient of the GS SST front will act to reduce the gradient in heat fluxes between the cold sector and the warm sector. This would subsequently result in a reduction in the difference in PV between the cold and warm sectors. The isentropes shown in this region in Figure 3.17 that extend from the surface to the tropopause would experience a reduction in distortion, acting to suppress strong ascent in the region. Suppressed vertical motion would also have a knock-on effect on latent heating in the WCBs in the warm sector, a reduction in which would be expected to decrease cyclonic intensity (as discussed in Chapter 1.7). Both these effects could potentially lead to a reduction in the precipitation rate experienced over the GS. In fact, Figure 3.19 plots a similar composite as in Figure 3.17,

again for days when a cyclone is present, but where the GS domain-averaged heat flux is less intense (the 1% of days between the 89.5% and 90.5% highest in the GSI is taken). Indeed, one can observe that whilst the generation of negative PV and the deformation of the isentropes does still occur with the passing of the cold front, they are both noticeably weaker.

3.6 CONCLUSIONS

The mean wintertime state in precipitation and tropospheric wind divergence/vertical velocity over the GS is dominated by two opposite regimes, one associated with the passing of an anti-cyclone, and one associated with the passing of a cyclone. These opposite extremes are reflected in the GS domain-averaged air-sea heat exchange, with the passing of stronger cyclones (anticyclones) resulting in stronger (weaker) ocean-atmosphere heat fluxes. Observations in GSI of the MSLP suggested that up to 90% of the time, atmospheric conditions appear to be determined by a propagating synoptic transient. This is confirmed by GSI decile plots of low- and upper-level wind divergence, as well as precipitation. The magnitude of this percentage, coupled with lagged composites of the upper-level vertical velocity and the precipitation, indicate the presence of a baroclinic waveguide. This is consistent with the idea that storm tracks comprise of an ensemble of wave packets with wave growth and decay occurring over all portions of the storm track (Chang et al., 2002, Wallace et al., 1988). This continuously propagating baroclinic wave (of varying strength) travelling over the GS determines the mean wintertime state in precipitation. However, this result is not simply due to precipitation having only positive values, as the baroclinic waveguide also determines the mean wintertime state in tropospheric vertical velocity, a variable for which ascent and descent can compensate. This can likely be explained by analysing a typical deep tropospheric motion system

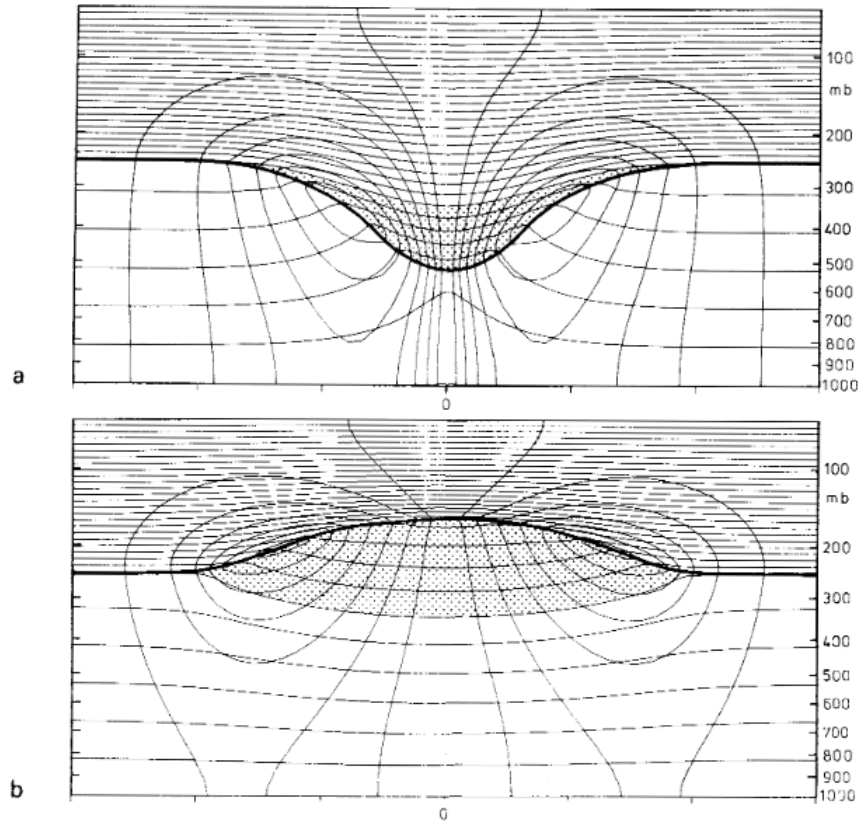


Figure 3.18: Schematic showing the flow structure induced by a (a) positive and (b) negative PV anomaly of simple shape. The location of each PV anomaly is stippled. The tropopause is marked by the thick black line, and thin lines are of isentropes every 5 K and transverse velocity every 3 m s^{-1} (Hoskins et al., 1985).

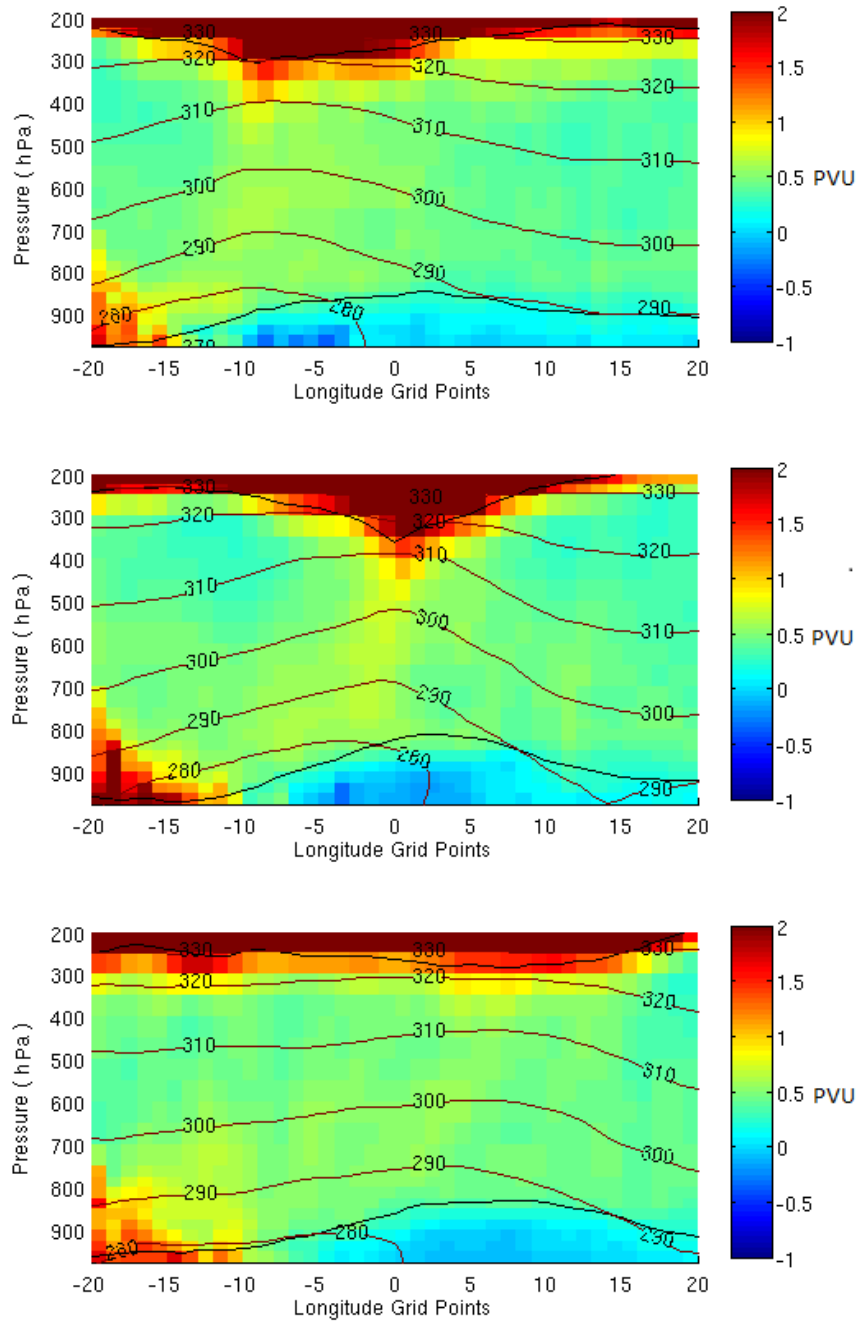


Figure 3.19: As in Figure 3.17, but for the 1% of days between the 89.5% and 90.5% highest indices in the GSI.

(such as a cyclone) projected upon a vertical section, a schematic of which is shown in Figure 3.20, from Green et al. (1966). The pattern of vertical motion is markedly asymmetrical, with the upward motion being large and concentrated into a small part of the system where the condensation of water vapour takes place. In and near this region, the flow is rapid and may be nearly adiabatic (the changes of state are nearly those in the appropriate dry or moist reference process), and a large amount of the condensed water is precipitated. Outside it however, descending motion is cloud-free and the return to surface at the same latitude is limited to the slow rate determined by radiative heat loss, the magnitude of which is equivalent on average to a tropospheric cooling rate of around 1° - 2° C/day. The difference between the actual temperature and potential temperature of warm air near the ground leads to long descent periods of up to 20 days or more. The arms of the descending circulation in Figure 3.20 are left open to indicate that the descent continues in other systems, and that there is no definite boundary on that side. The descending air found in an anti-cyclone trailing behind such a cyclonic system is therefore unlikely to be related in any way to the air that ascended in that cyclonic system.

In addition, it is clear that the stronger the passing atmospheric transient, the larger its contribution to the mean pattern. In the case of precipitation, there is a very noticeable bias towards the most extreme events. Indeed, the top (bottom) 20% of the GSI, associated with the passing of a cyclone (anticyclone), can account for up to 50% of the local precipitation to the east (west - associated with the cyclone trailing behind the anticyclone) of the GS domain. As previously mentioned, a smoothing of the SST gradient across the GS results in a significant weakening of the mean wintertime pattern in precipitation (Kuwano-Yoshida et al., 2010). In the light of these results, it is clear that the key to understanding this occurrence lies in the interaction of the GS front with

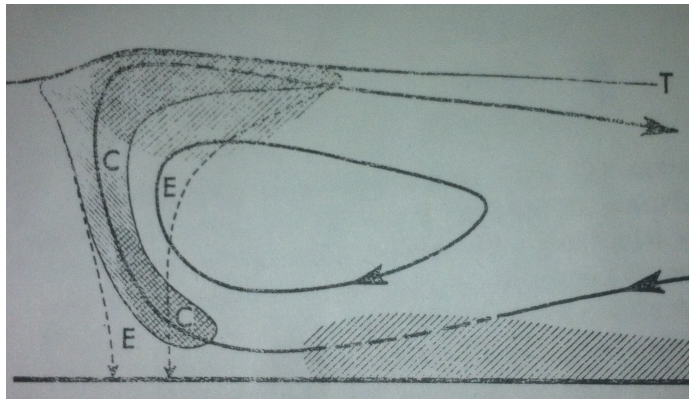


Figure 3.20: Schematic representation of flow in a deep tropospheric motion system, projected upon a vertical section. The hatched area at the surface represents the layer of small-scale convection, within which subsiding air has its potential temperature raised. Air from this layer enters a cumulonimbus or large-scale circulation and ascends into the upper troposphere. Condensation, C, of water vapour occurs, and small-scale convection may develop again in the cloud system where there is cross-hatching. Precipitation falls from the cloud (pecked lines) and there is some evaporation, E, outside it. The descending branch of the large-scale circulation is left open on the right to indicate that it continues in several motion systems, accompanied by a slow radiative loss of potential temperature. T marks the tropopause. (Green et al., 1966).

the passing atmospheric transients. This is studied in more detail in the next research chapter.

In Section 3.5, a potential mechanism whereby the SST gradient could interact with a cyclone and subsequently alter the precipitation rate is suggested. Observations of EEs indicate the presence of negative PV anomalies in the cyclonic cold sector, creating a PV gradient between itself and the warm sector ahead of it. This acts to distort the isentropes, allowing for enhanced vertical motion. Indeed, in this region there is a sharp reduction in the free troposphere over the GS (to only around ~ 3 km in the most extreme cases), whereby isentropes are seen to connect almost from the surface to the tropopause. Smoothing the SST gradient could act to reduce the ocean-atmosphere heat flux gradient between the cold and warm sectors, which would then result in a reduced PV gradient. Such a decrease would act to suppress vertical motion and reduce precipitation. Indeed, similar observations from days where there is a cyclone present but the surface heat flux is weaker show that the generation of negative PV anomalies and the deformation of isentropes, whilst still present, are noticeably weaker. At the time of writing, simulations are currently being run by Benoît Vanni re at Imperial College London using the Meteorological Office Unified Model to test this hypothesis.

CHAPTER 4

THE IMPACT OF SEA-SURFACE TEMPERATURE ON ATMOSPHERIC FRONTS PROPAGATING OVER THE GULF STREAM

4.1 INTRODUCTION

The timescales on which ocean currents change are much longer than those for weather forecasts. This is especially true away from the tropics, where the stronger effects of the Earth's rotation force slower oceanic motions. As a consequence, if a mechanism whereby the extra-tropical oceans impact the atmosphere can be established, an extremely valuable source of climate predictability will be opened. At present, whilst empirical evidence for extra-tropical oceanic influence on climate has been steadily accumulating (e.g. Rodwell et al, 1999, Czaja and Frankignoul, 2002, Woollings et al. 2010), such a mechanism has yet to be singled out.

Over the GS, it has been suggested that the thickness of the layer of oceanic influence is as large as $\sim 5\text{-}10\text{km}$ (Minobe et al, 2008, Czaja and Blunt, 2011). In particular, mean patterns in upper-level tropospheric wind divergence are found to meander with the GS front. Furthermore, analogous mean patterns in precipitation are seen to significantly weaken with a smoothing of the SST

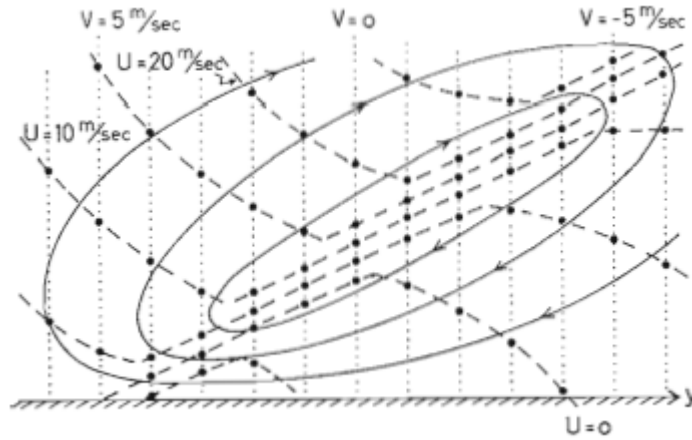


Figure 4.1: Transverse motion in an idealized frontal zone, with warmer air to the left. The frontogenic horizontal deformation field is such that the meridional velocity increases with latitude, and all isotherms in isobaric surfaces are assumed parallel with the front. Dashed lines: zonal velocity isotachs. Dotted lines: meridional velocity isotachs. Solid lines: streamlines of transverse non-geostrophic circulation. (Eliassen, 1962).

gradient. In Chapter 3, these mean wintertime atmospheric patterns in tropospheric divergence and precipitation over the GS were in fact shown to be primarily determined by a “baroclinic waveguide” (i.e. an almost continuous series of propagating cyclones and anticyclones). Given this result, it is evident that the key to understanding the relationship between the sharp SST gradients and the mean wintertime atmospheric pattern lies in the interaction of the oceanic fronts with passing atmospheric fronts, since fronts are where upward motion and precipitation occur.

One mechanism whereby a modification of the SST gradient could alter an atmospheric front is that of “thermal damping”. That is to say, a perturbation of the SST underneath an atmospheric front results in a change in the air-sea heat exchange on both sides of the front. Subsequently, the thermal gradient between either side of the atmospheric front is altered, resulting in a change of

front characteristics. For example, a weakening of the lateral atmospheric temperature gradient would lead to a reduction in the transverse circulation present at the front (Eliassen, 1962); a schematic of an example transverse circulation at a front is shown in Figure 4.1. This would then necessarily affect the vertical velocity and precipitation rate in the region. Additionally, the magnitude of such damping will naturally change depending on the angle of the front relative to the SST gradient. This offers another possibility: that atmospheric fronts are steered by stronger SST gradients, resulting in a preferential angle alignment that could lead to the maintenance of front strength.

In Section 4.2, the model dataset used for the analysis in this chapter is presented, accompanied by some background on atmospheric frontogenesis. In Section 4.3, we start simply by asking - does a smoothing of the GS SST gradient result in a damping of the atmospheric fronts passing over it? Furthermore, what is the dependence of this damping on initial front strength, as well as location over the GS? In section 4.4, the significance of the angle between atmospheric and oceanic fronts is discussed for realistic and smoothed cases of SST gradient. In Section 4.5, the question of whether strong SST fronts alter the direction of propagation of (“steer”) the atmospheric fronts is considered. Finally, in Section 4.6, the profiles of associated atmospheric variables such as vertical velocity and precipitation are assessed, and a consideration is given to the effect of thermal damping.

4.2 MODEL DATASET

4.2.1 SEA-SURFACE TEMPERATURE

The model data to be analysed is from the Atmospheric General Circulation

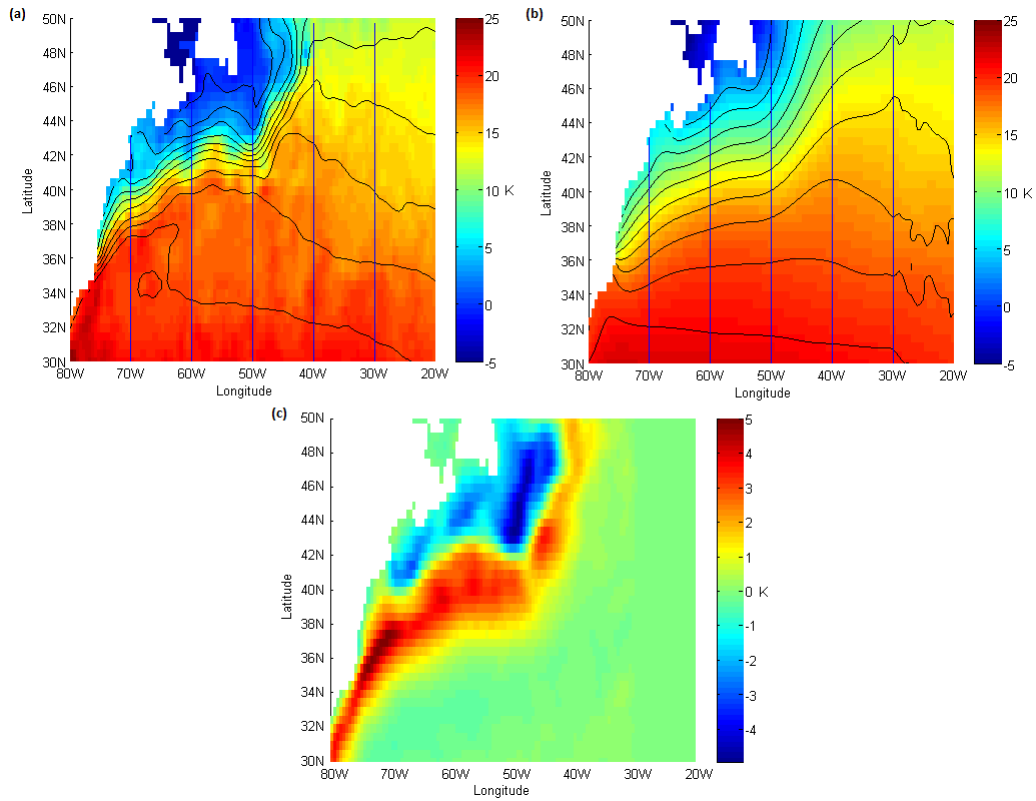


Figure 4.2: Twenty-year wintertime mean (DJF 1981-2000) of SST for the (a) CNTL experiment and (b) SMTH experiment. Contours, in black, are shown from 2°C to 20°C , at 2°C intervals. Also shown on both figures, and annotated in (b), are the lines of constant longitude used for analysis in this chapter. These are (70W, 29.7-43.2N), (60W, 29.7-45.2N), (50W, 29.7-49.7N), (40W, 29.7-49.7N), (30W, 29.7-49.7N). The difference in SST between the CNTL and SMTH experiment is shown in (c).

Model for the Earth Simulator (AFES; Ohfuchi et al., 2004) version 2 (Enomoto et al., 2008), developed at the Earth Simulator Center, Japan Agency for Marine-Earth Science and Technology. The horizontal resolution is T239, about 50km in grid spacing, with 48 scaled pressure levels in the vertical. The bottom boundary condition in the model uses the real-time global SST (Thiébaux et al., 2003) dataset of the NCEP on a 0.5° grid and at daily intervals.

In this chapter, data from two experiments is used: a control experiment (CNTL), which uses the original real-time global SST data, and another experiment (SMTH), which smooths the SST data over the GS region by applying a 1-2-1 running mean filter in both the zonal and meridional directions 100 times on a 0.5° grid over 25° - 55° N, 100° - 30° W. Initial conditions are taken from ERA-40 (Uppala et al., 2006), and the present study uses a 6-hourly output for 20 winter seasons (DJF) between 1981 and 2000. Figures 4.2(a) and (b) show the mean SST for the CNTL and SMTH runs respectively, with both figures plotted up to 20W to further emphasize the effect of the smoothing (i.e. in the difference in SST contours either side of 30W in (b)). The difference in mean SST (CNTL-SMTH) is shown in Figure 4.2(c). Cooler (up to ~ 5 K) water is found in the CNTL case (up to around $\sim 8^\circ$ C mean SST), followed by warmer water (again up to ~ 5 K) and then a region of negligible difference where the SST gradient is originally weakest.

4.2.2 IDENTIFICATION OF ATMOSPHERIC FRONTS

A measure of front intensity $F^* = \zeta_{925} | \nabla T_{925} |$ is used to identify frontal regions, in which ∇T_{925} is the temperature gradient on the 925hPa surface and ζ_{925} is the component of the curl of the wind vector normal to that same pressure surface (the isobaric relative vorticity). The rationale for this choice is that both ∇T_{925} and ζ_{925} are expected to be large in frontal situations. This

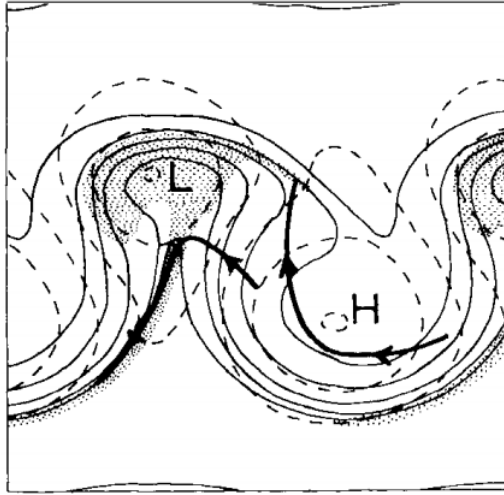


Figure 4.3: An example surface map for a baroclinic wave with a strong surface cold front and a developing warm front. Temperature contours every 4K are shown as continuous lines, geopotential contours are marked with dashed lines, and the region of relative vorticity larger than $\frac{f}{2}$ is shaded. The relative vorticity in the cold front region has a maximum of $5f$. (Hoskins, 1982).

is as a result of the transverse circulation developing when cold and warm air masses are brought into contact by a large scale confluent flow (Hoskins, 1982). An example surface map snapshot of a baroclinic wave is shown in Figure 4.3, in which a strong surface cold front has formed (with a weaker warm front starting to appear to the northeast of the low), colocated with a region of large relative vorticity. In order to make F^* non dimensional (hereafter denoted by F), it is further divided by a typical scale for temperature gradient (1K/100km) and vorticity (the value of the Coriolis parameter at the mid-latitude point of the domain considered, i.e. 40N). An example atmospheric frontal system is shown in Figure 4.4(a), at 12:00UTC on December 28th 1981. The fronts themselves are highlighted in magenta (contour $F \geq 1$), whilst the vertical velocity is shown in colour and SST contours from 2°C to 20°C, at 2°C intervals shown in black. The cold front has a banded structure, with several cold fronts developing

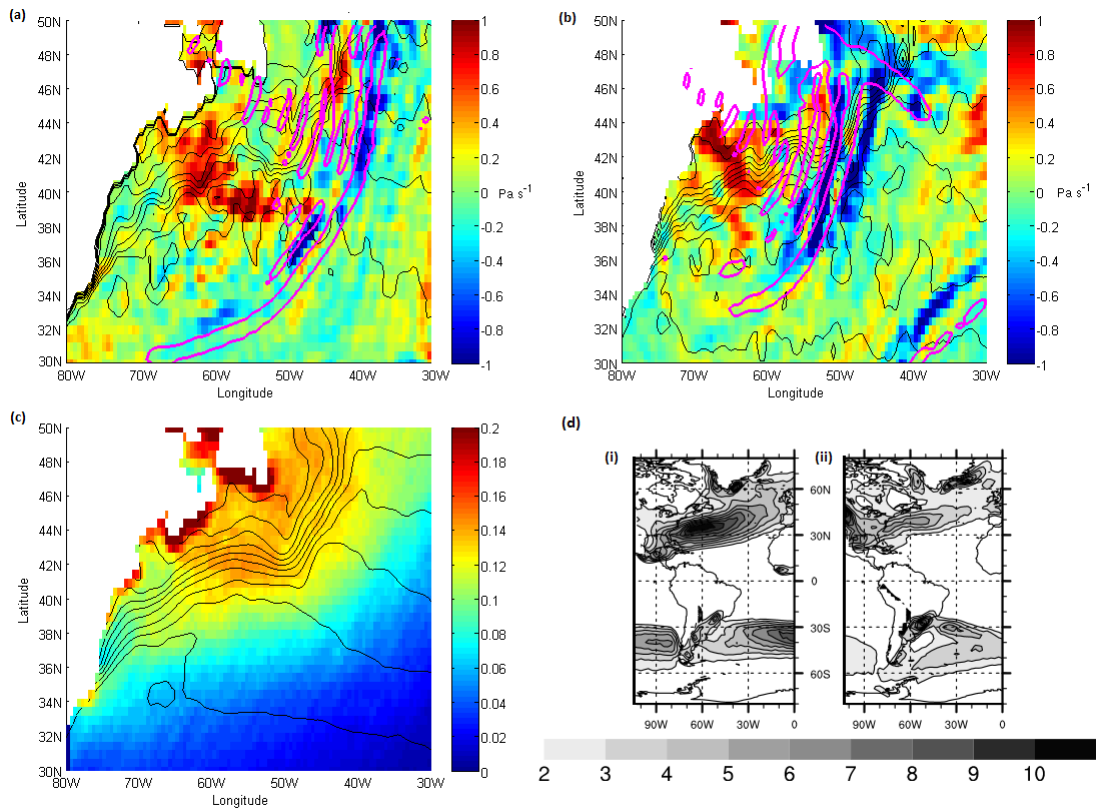


Figure 4.4: (a) An atmospheric front, as defined in the text, highlighted in magenta, at 12:00UTC on December 28th 1981. Also shown at that time is the vertical velocity (colour), and contours of SST from 2°C to 20°C, at 2°C intervals (black). (b) Another atmospheric front, as defined in the text, identified at 18:00UTC on February 28th 2001. (c) Fraction of wintertime days in the CNTL experiment where the front variable F exceeds unity. Contours of SST are as in Fig. 4.2(a). (d) Percentage of wintertime days where (i) a cold front and (ii) a warm front is objectively identified in the Atlantic, from Berry et al. (2011).

behind the main cold front. This phenomena of multiple cold fronts is not rare and is commonly found in observations (e.g. Browning et al., 1997). As expected, there is strong ascent to the east of the leading cold front ($\sim 40^{\circ}\text{W}$) and strong descent to the west ($\sim 60^{\circ}\text{W}$). Figure 4.4(b) similarly identifies another atmospheric frontal system, at 18:00UTC on February 28th 2001, with a more extreme case of the multiple cold front phenomena, and a warm front also identified, with a structure consistent with that of an extra-tropical cyclone described in Chapter 1.7. In this case, there is also a strong banded signature in the mid-level vertical velocity, with ascent at the first and second leading cold front, which offers some strength to the validity of the frontal identification method. Indeed, whilst Hewson (1998) cautions against the use of vorticity as a sole identifier for fronts, its use here is accompanied by a metric in low-level temperature gradient also. By increasing the frontal threshold in F , it is possible to exclude these developing cold fronts, although it is then not possible to correctly identify all the storms propagating through the region. Figure 4.4(c) indicates the frequency of occurrence of events in the CNTL experiment where $F \geq 1$ over the GS. This threshold provides a spatial distribution and frequency of frontal events in agreement with other frontal detection methods. For example, Figure 4.4(d) illustrates the percentage of wintertime days in the ERA-40 reanalysis from Berry et al. (2011) where (i) a cold front and (ii) a warm front is objectively identified in the Atlantic. However, this is a real world example, whereas the data considered in this chapter is model data (a previous use of this diagnostic in the real world can be found in Sheldon et al. (2013)). It is noted that some overestimation of the frontal frequency exists at certain locations along the coastline. This is likely caused by anomalies in the low-level temperature gradient and vorticity that exist at the land-sea boundary in both the CNTL and SMTH experiments and will not significantly affect the

present analysis. Finally, the work in this chapter does not distinguish between cold and warm fronts, although one would expect to find them closely located. Furthermore, it can be seen in Figure 4.4(d) that there are more than twice the number of cold fronts as there are warm fronts over the GS. A potential explanation for this is discussed in Section 4.4.

4.3 THE EFFECT OF SEA-SURFACE TEMPERATURE GRADIENT ON ATMOSPHERIC FRONT STRENGTH

Figure 4.4(c) illustrated the frequency of atmospheric fronts over the GS from the CNTL experiment, i.e. with a realistic SST gradient. Figure 4.5(a) illustrates the same frequency for the SMTH experiment, with the percentage reduction (in the occurrence of $F \geq 1$) with respect to the CNTL experiment plotted in Figure 4.5(b) (i.e. positive (negative) represents a reduction (increase)). It is immediately noticeable that there is a strong reduction in atmospheric front number in the SMTH experiment across the vast majority of the GS meander. This percentage reduction becomes as large as 30% where one encounters the strongest horizontal SST gradient directly off the continent ($\sim 70\text{W}$, 38N). North of 36N , the further one moves away from the continent, the smaller the effect the smoothing process has on the SST gradient, and the magnitude in reduction of atmospheric fronts decreases. Interestingly however, south of $\sim 36\text{N}$ until roughly $\sim 34\text{N}$, there is a region where there is actually a percentage increase in the occurrence of $F \geq 1$, creating a noticeable dipolar pattern west of $\sim 50\text{W}$. It is noted however that the number of fronts here is less than north of 36N and could just represent noise. To this end, the same analysis was performed again on randomly sampled periods of five years (within the same twenty year range), and this same dipolar signal is consistently found, indicating the robustness of

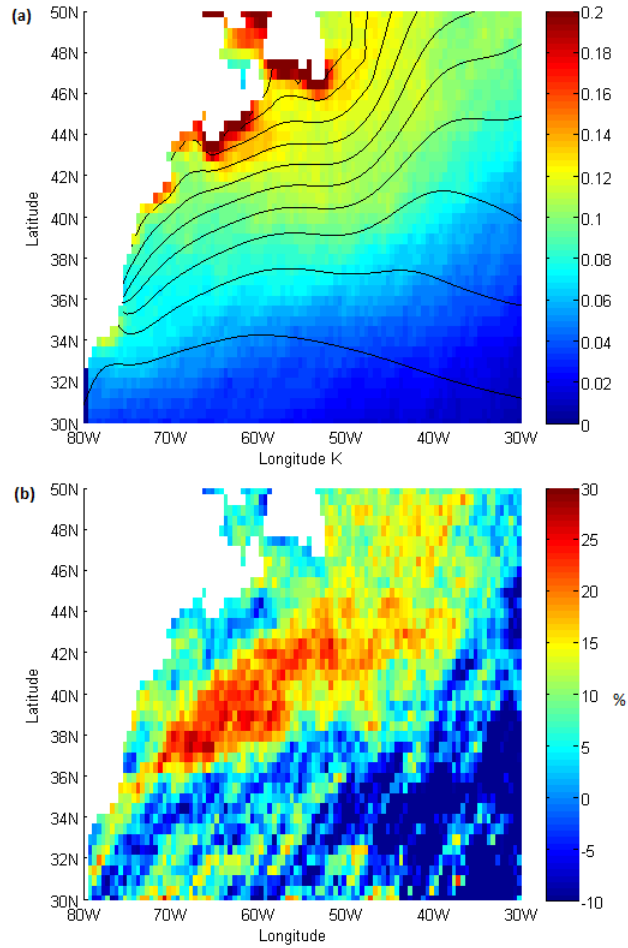


Figure 4.5: (a) As in Figure 4.4(c), but for the SMTH experiment. (b) The percentage reduction in the occurrence of $F \geq 1$ in the SMTH experiment, relative to the CNTL experiment.

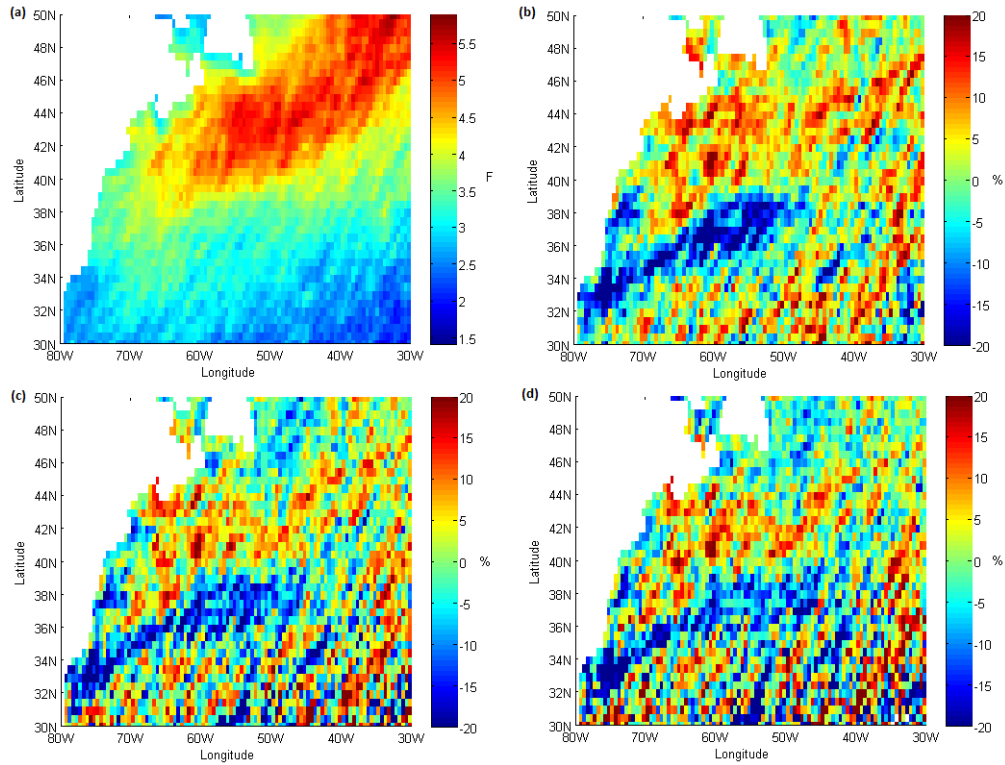


Figure 4.6: (a) Average wintertime value of F when an atmospheric front ($F \geq 1$) is present, with the percentage reduction in F in the SMTH relative to the CNTL experiments shown in (b). This percentage change is calculated for two higher thresholds of atmospheric front intensity in (c) $F \geq 3$ and (d) $F \geq 5$.

the result. Consideration of Figure 4.2 shows that in this area of percentage increase, the horizontal SST gradient is actually larger in the SMTH experiment than it is in the CNTL experiment. Both these observations are consistent with a reduction in atmospheric front strength with reduction in SST gradient.

Whilst it is clear from Figure 4.5(b) that a reduction in atmospheric front strength occurs with the smoothing of the SST gradient, no information is given about the extent to which front strength is affected, nor whether there is a scaling in strength reduction with initial front strength. Figure 4.6(a) shows a plot of the average wintertime value of F when an atmospheric front ($F \geq 1$)

is present. The average value of an atmospheric front when it first travels off the continent is $\sim F = 3$, a value that steadily increases upstream to $\sim F = 5$. This increase in front strength is consistent with the strong baroclinic growth rates exhibited over the GS, and one expects an increase in cyclone intensity in this region. The percentage decrease in front strength (as measured by $F \geq 1$) in the SMTH experiment relative to the CNTL experiment is shown in Figure 4.6(b). Comparison with Figure 4.5(b) shows that west of $\sim 50\text{W}$, where one experiences the biggest change in occurrence of $F \geq 1$, where there is a reduction (increase) in the number of fronts, the front intensity decreases (increases) by roughly 20%. Furthermore, this statistic is calculated for two larger thresholds of F in Figure 4.6(c) ($F \geq 3$) and Figure 4.6(d) ($F \geq 5$). Whilst there is naturally more noise in these cases (as there are less of them), it is still possible to notice that the typical magnitude in the percentage changes west of $\sim 50\text{W}$ is generally extremely similar - in the region where the SST gradient is strongest in the CNTL experiment, a reduction in the SST gradient appears to affect atmospheric fronts equally relative to their strength. It is noted that the region (30-50W, 30-40N) exhibits far too much noise, and so no meaningful conclusion can be drawn here - in any case, there is a relatively negligible amount of atmospheric frontal activity in this area (Figure 4.4(c)) (which is presumably the cause of the high noise level).

4.4 THERMAL DAMPING OF FRONTS

It has been shown in the previous two sections that a reduction in the SST gradient causes a reduction in front intensity over the GS. The strongest reduction in atmospheric front ($F \geq 1$) number occurs just off the eastern coast ($\sim 36\text{W}$) of the United States, where the smoothing process causes the largest change in SST gradient. Upstream (30-50W,40-50N), there is an increase in front intensity, as one would expect from the strong baroclinic growth rate in

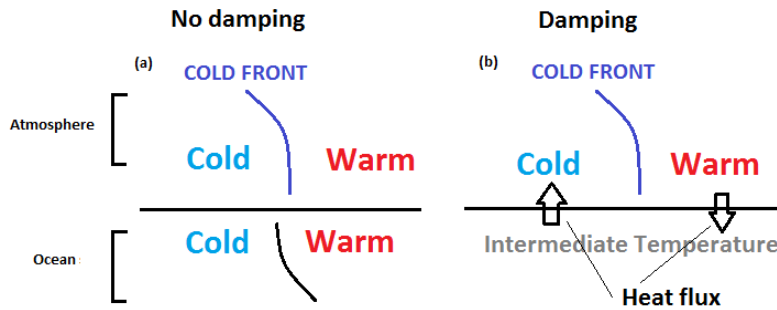


Figure 4.7: Schematic of an atmospheric cold front passing over (a) a strong SST gradient (b) a smoothed SST gradient.

the region. In the absence of a passing weather system, the warm waters of the GS will thermally interact with the background wind provided by stationary waves - a stronger SST gradient will in some manner better “pre-condition” the atmosphere by increasing the local baroclinicity. Naturally, the stronger the regional baroclinicity, the stronger the expected cyclogenesis, and atmospheric front intensification.

However, there is an alternative mechanism that could play a significant role in affecting the intensity of passing atmospheric fronts. The concept of “thermal damping” is illustrated in Figure 4.7, which shows a schematic of a cold front passing over an SST gradient. Over the GS, the interaction of the warm waters with relatively cold continental air ensures that there is a large ocean-atmosphere heat transferral. However, there is also a gradient in SST (a), which causes water to interact with the colder air behind the cold front that is colder than the water interacting with the air in the warm sector ahead. In this respect, the SST gradient acts to partially reduce the action of the surface heat fluxes to dampen the low-level horizontal temperature gradient of the atmospheric cold front. If one were to smooth the SST gradient entirely however, as shown in (b), this reduction would be smaller, leading to a more

intense weakening of the cold front.

In the event of a warm front, this effect is reversed. In the limit of homogeneous SST as in (b), an atmospheric warm front that is aligned in the same manner as the atmospheric cold front previously discussed will experience the same amount of damping. But when there is a strong SST gradient as in (a), there will now be the interaction of colder (warmer) water with warmer (colder) air, resulting in significant frontal damping. In reality, warm air is brought from the south and warm fronts are aligned more towards the perpendicular with regards to the GS SST gradients. Nevertheless, a strong component of thermal damping will still exist relative to that experienced by a cold front. This offers a potential explanation for the disparity in wintertime occurrence between cold fronts and warm fronts in Figure 4.4(c).

Indeed, given that there are more than twice as many cold fronts as warm fronts located over the GS, our analysis of the total number of atmospheric fronts will reflect more heavily on the behaviour of the cold fronts. Given this, the percentage change in atmospheric front occurrence in the SMTH experiment from the CNTL, shown in Figure 4.5, would be consistent with this thermal damping mechanism. Just off the continent, there is a reduction in front intensity north of 36N, where the relative SST gradients in the CNTL experiment are as in (a), and the SMTH experiment as in (b). South of 36N however, the situation switches around, and it is here we find instead an increase in front intensity in the SMTH experiment. This hypothesis is tested more quantitatively in Section 4.6.1.

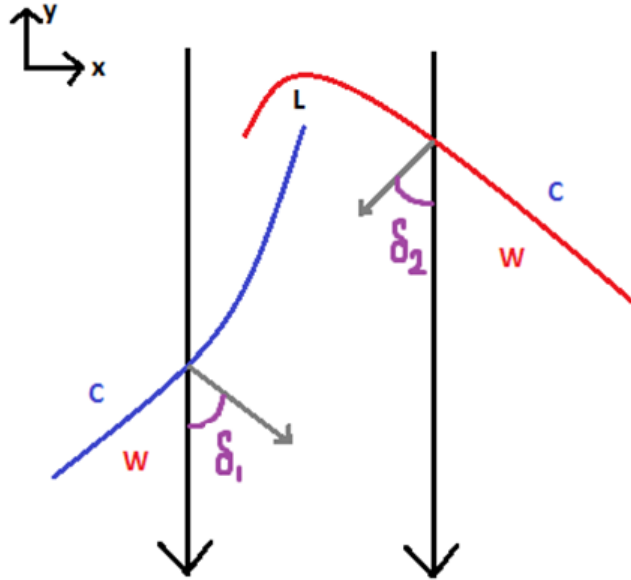


Figure 4.8: Schematic illustrating the angles δ_1 and δ_2 between the frontal horizontal temperature gradient at 925hPa and lines of constant longitude, for cold fronts and warm fronts respectively.

4.5 STEERING OF ATMOSPHERIC FRONTS BY SEA-SURFACE ISOTHERMS

This idea of the oceanic SST gradient thermally damping an atmospheric front also leads to another question - is there a preferential angle alignment of the atmospheric and oceanic fronts? It can be seen from Figure 4.7 that if one changes the angle of the atmospheric cold front with respect to the oceanic front, the differential ocean-atmosphere heat transfer will change accordingly, resulting in a subsequent change in magnitude of the thermal damping effect. This section considers whether a stronger SST gradient acts to alter the direction of the atmospheric fronts, and in this way lead to a preferential angle alignment.

In order to test this, consider an example frontal system as in Figure 4.8. Firstly, the direction of the low level wind shear is computed from the gradient

of the low-level (925hPa) temperature (related via the thermal wind equation - ref. Equation 1.1). This is shown by the grey vectors. Then, the angle between these vectors and lines of constant longitude vectors (shown in black), δ_1 and δ_2 for cold fronts and warm fronts respectively, is calculated. Unfortunately, the present study does not distinguish between cold and warm fronts and the following analysis groups these two angles together into one set of common angles, δ . The implications of not distinguishing between cold and warm fronts are discussed later in this section.

For each of the five constant longitude domains indicated in Figure 4.2, whenever there is an atmospheric front ($F \geq 1$) present, this angle δ is calculated for both the CNTL and SMTH experiments. Using 10 bins (centered on 0° to 90° at 10° intervals), the percentage distribution (i.e. each bin divided by the total occurrence) is then plotted in Figure 4.9 for (a) (70W, 29.7-43.2N) (b) (60W, 29.7-45.2N) (c) (50W, 29.7-49.7N), (d) (40W, 29.7-49.7N) and (e) (30W, 29.7-49.7N). It is noted that the first and last bin include values of δ that range from -5° to 0° , and 90° to 95° respectively. No values in these ranges are physically observed, but this will have no impact on the comparison of angle distribution. The percentage distribution from the CNTL experiment is shown in red and that from the SMTH experiment is shown in black. In (a), (b), (d) and (e), there is a negligible change in the distribution of angles between the CNTL and SMTH experiment. In (c) however, at longitude 50W, it appears as if there could be a shift in the peak of the distributions between $\sim 30^\circ$ to 40° , but it is difficult to be certain using only 10 bins. To this end, this graph is repeated in (f), but using 91 different bins, which increases the noise of the graph but allows for a better idea of that range in the distribution. Indeed, this graph illustrates that there is an apparent shift in the peak of the angle of fronts at this longitude, implying a change of direction (“steering”) of the

atmospheric fronts between the CNTL and SMTH experiment of about 10° . In addition, there appears to be a delay for a front to adjust to the perturbation in the SST gradient shown in Figure 4.2(c). Indeed, once the atmospheric front passes over perturbed SSTs around $\sim 70\text{W}-60\text{W}$, there is a delay on the order of $\sim 10^\circ$ longitude before a change in frontal direction is observed at 50W . This change in direction is then restored to its CNTL state when it passes over similar SST contours around $\sim 40\text{W}-30\text{W}$, again with a delay on the order of $\sim 10^\circ$ longitude. Indeed, assuming the associated storm travels at $\sim 10 \text{ m s}^{-1}$, this leads to a timescale of ~ 1 day, which is consistent with a typical timescale for air-sea interactions and frontogenesis.

Unfortunately, whilst this analysis demonstrates that a perturbation to the GS SST distribution can alter atmospheric fronts propagating through the region, conclusions are limited by not distinguishing between cold fronts and warm fronts. Nevertheless, it has been discussed in Sections 4.2.2 and 4.4 that the current study is expected to represent more heavily the behaviour of cold fronts. Firstly, cold fronts are known to be encountered more frequently over the GS. Secondly, the change in thermal interaction between the GS and the overlying atmospheric fronts from smoothing the SST gradient will affect warm fronts much less than cold fronts, due to the fact that warm fronts tend to be aligned orthogonally to the GS (and hence parallel to the SST gradient). If the distribution of δ does represent mostly the behaviour of cold fronts (i.e. δ_1), then the roughly 10° change in δ at 50W in Figure 4.9 implies that a smoothing of the SST gradient will result in a more meridionally orientated cold front (zonally orientated cold front temperature gradient).

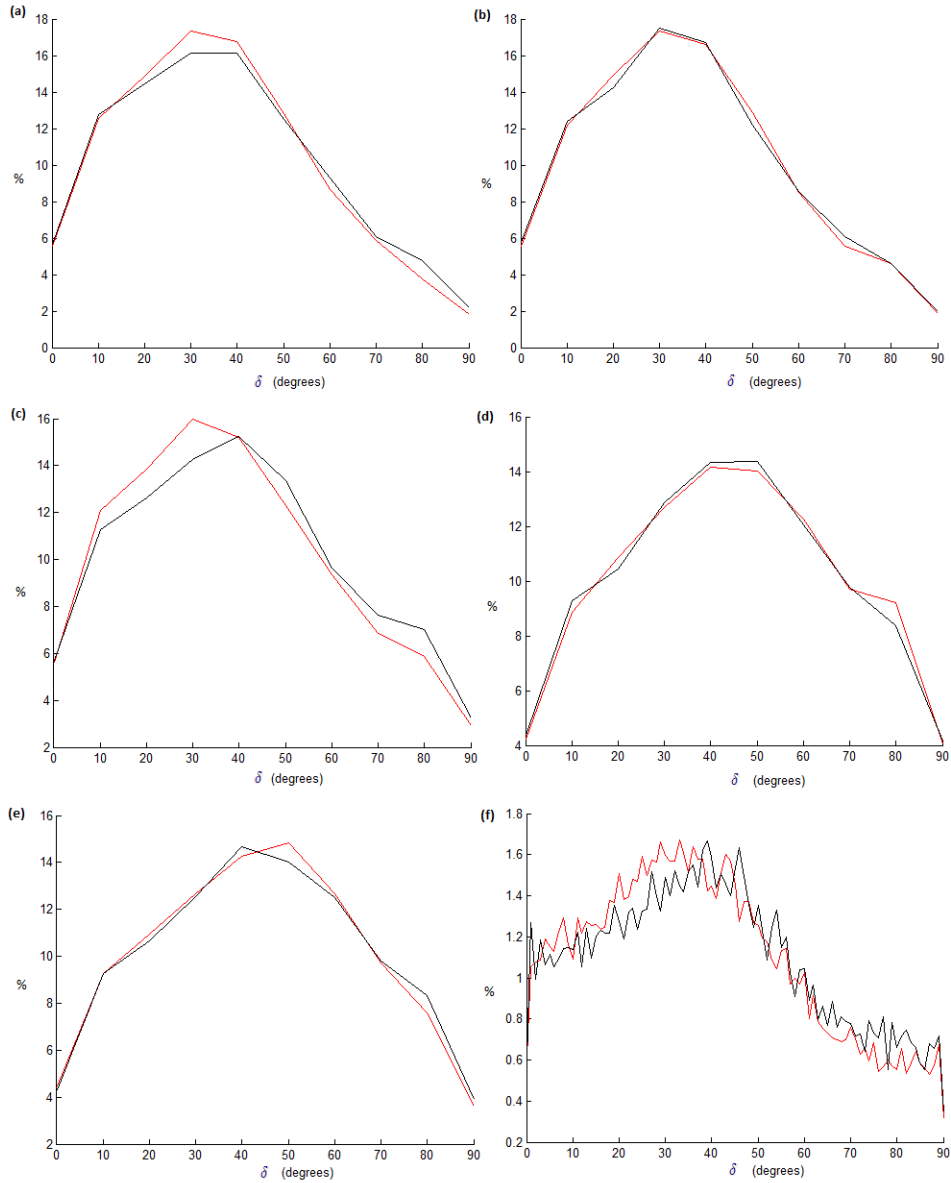


Figure 4.9: The percentage distribution of δ for each of 10 bins (-5° - 5° to 85° - 95° at equal intervals) for (a) (70W, 29.7-43.2N) (b) (60W, 29.7-45.2N) (c) (50W, 29.7-49.7N), (d) (40W, 29.7-49.7N) and (e) (30W, 29.7-49.7N). (f) As in (c), but for 91 different bins (-0.5° - 0.5° to 89.5° - 90.5° at equal intervals). The CNTL simulation is shown in red, whilst the SMTH is shown in black.

4.6 THE EFFECT OF SEA-SURFACE TEMPERATURE GRADIENT ON VERTICAL VELOCITY AND PRECIPITATION

4.6.1 PRECIPITATION

Before considering the variation of precipitation with location, it is first informative to examine a distribution at a particular longitude. Figure 4.10 exhibits a histogram of both the convective and large-scale precipitation across all days across the constant longitude domain (60W, 29.7-45.2N). There are 228,480 total precipitation data points across the analysis period, and each bin is 1mm day^{-1} wide (except for the first bin, which is centred on zero, and so represents rainfall between 0 and 0.5mm day^{-1}). Histograms are shown for both the CNTL and SMTH experiments. Firstly, it is noted that there is an incredibly large range in the precipitation rate. For both experiments, there are values as large as $\sim 90\text{mm day}^{-1}$ for convective precipitation and $\sim 250\text{mm day}^{-1}$ for large scale precipitation. However, there is an overwhelming bias in days towards the lower end of the spectrum, with over 50% of days falling in the $0\text{-}0.5\text{mm day}^{-1}$ bins for both the convective and large scale precipitation. In the SMTH experiment, there appears to be no significantly noticeable shift in terms of the large-scale precipitation relative to the CNTL. For the convective precipitation however, there is a subtle but noticeable shift in the shape of the histogram, steepening the curve in the SMTH experiment compared to the CNTL, and decreasing the amount of stronger convective precipitation events ($> 30\text{mm day}^{-1}$) whilst increasing the amount of weaker events.

The average variation of both convective and large-scale precipitation is addressed in Figure 4.11. Across the twenty-year wintertime analysis period, the mean convective and large-scale precipitation in the CNTL experiment are shown in (a) and (c) respectively. The mean pattern in convective precipitation exhibits a sharp gradient and has a localised maximum ($\sim 5\text{mm day}^{-1}$)

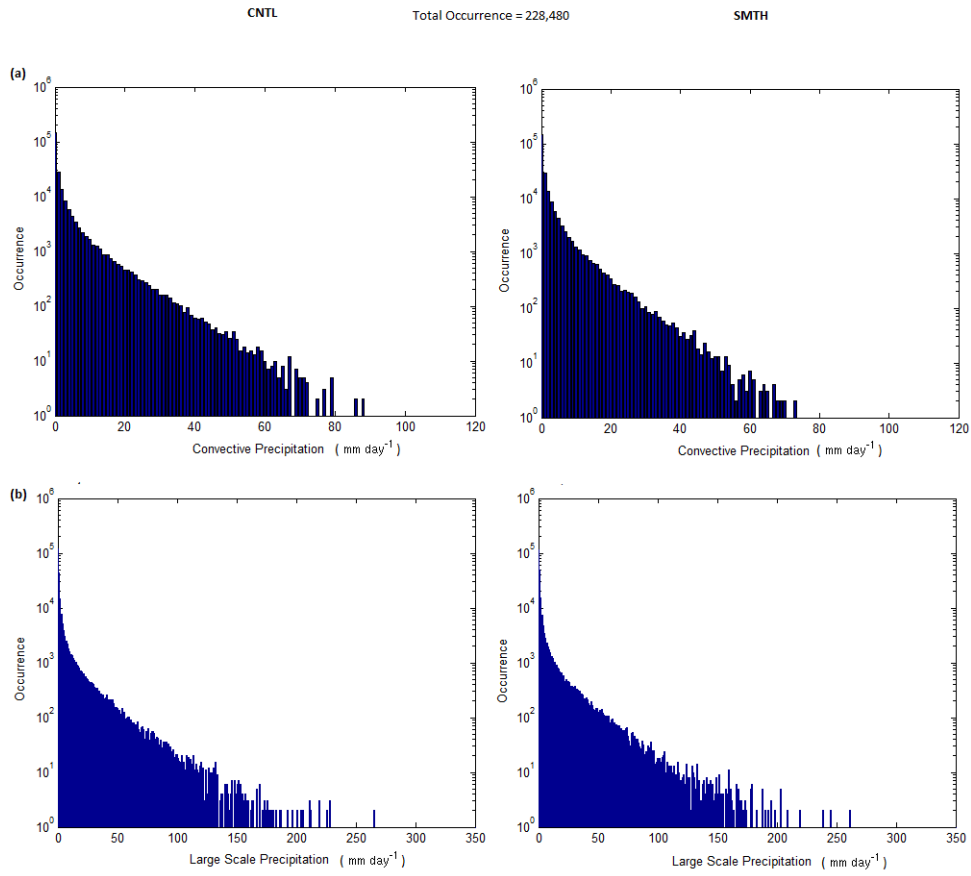


Figure 4.10: Histograms of (a) convective and (b) large-scale precipitation for the constant longitude domain (60W, 29.7-45.2N) across the twenty-year wintertime analysis period, for both the CNTL and SMTH experiments. Each bin is 1mm day^{-1} wide, and each histogram has a total of 228,480 data points.

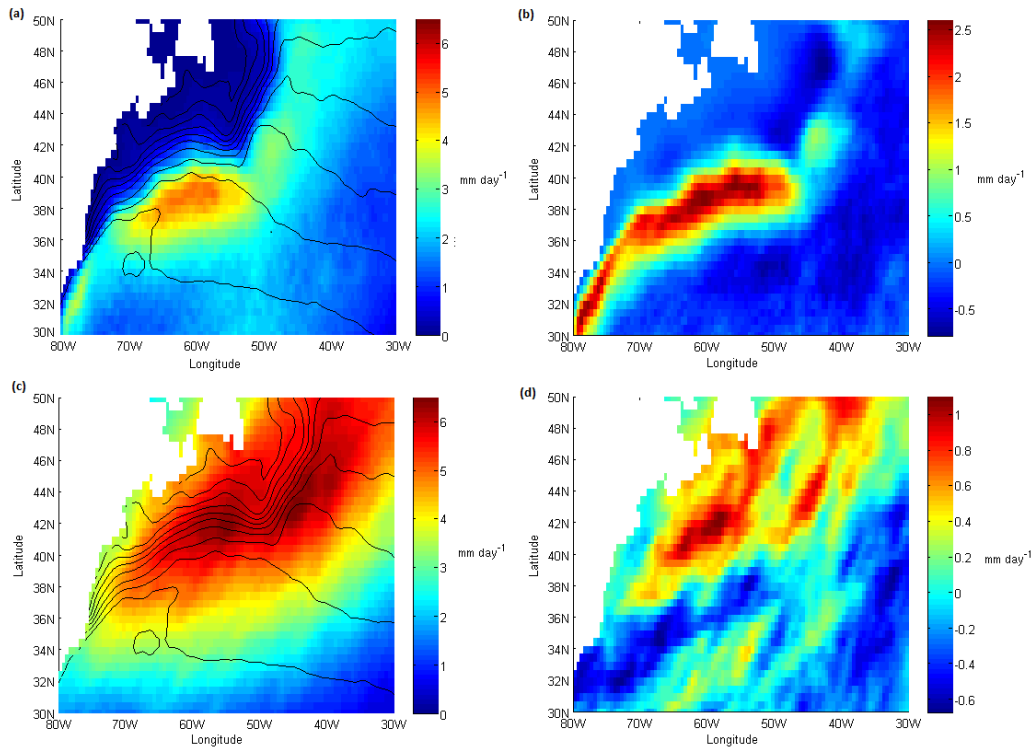


Figure 4.11: Twenty-year wintertime mean in (a) convective precipitation and (c) large scale precipitation in the CNTL experiment. Mean contours of SST are shown in black. The average reduction in the SMTH experiment from the CNTL experiment is shown for the (b) convective precipitation and (d) large scale precipitation.

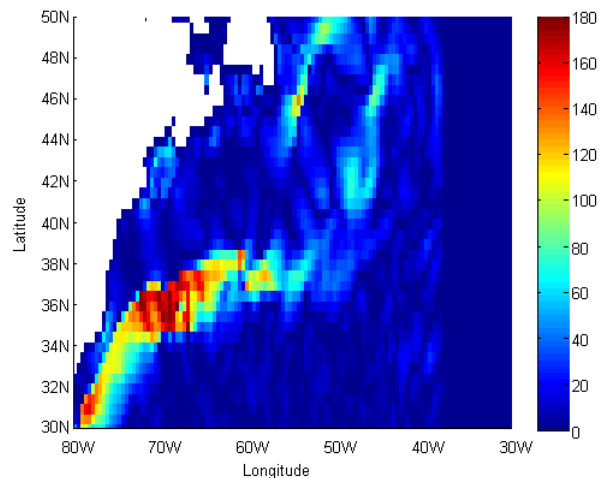


Figure 4.12: Angle between the mean SST gradients in the CNTL and SMTH experiments.

on the warm side of the GS front, whereas the mean large-scale precipitation is generally slightly larger but more diffuse. Indeed, large-scale precipitation is strongly associated with cyclonic warm-sectors and one would expect this from the variation in path as a cyclone travels upstream over the GS. The average reduction in convective and large scale precipitation in the SMTH experiment relative to the CNTL is shown in (b) and (d) respectively (i.e. positive (negative) is a reduction (increase)). Several things are striking about both these plots. Firstly, the reduction in convective precipitation is centered almost entirely along the GS front, with negligible reduction elsewhere (and in fact some minor increases also). In addition, the magnitude is extremely large, with reductions of between $\sim 50 - 75\%$ across the entire front. This is in stark contrast to the reductions in large scale precipitation, which is much smaller (maximum $\sim 15\%$) and is largely spread out; (this observation is consistent with those from Figure 4.10, in which there is a noticeable shift in convective precipitation between the extremes in the two experiments, but not so much for the large-scale

precipitation). Indeed, it is in fact the reduction in the convective precipitation that results in the largest change to the mean pattern in total precipitation over the GS. This is consistent with the results presented in Kuwano-Yoshida et al. (2010).

In the case of large scale precipitation there are comparable increases in precipitation as well. Indeed, these areas of increase in the SMTH experiment are located in the same regions that we expect an increase in the number of atmospheric fronts (cf. Figure 4.5(b)). It is interesting to note that this apparent meridional dipole pattern at $\sim 36\text{N}$ is also consistent with the difference in angle between the CNTL and SMTH SST gradients, as plotted in Figure 4.12. Given that there is no noticeable steering of fronts west of 50W , it follows that the fronts themselves must therefore be on average aligned very differently with the SSTs in the region south of 36N . Figure 4.13 confirms this to be the case. Figure 4.13(a) shows the average wintertime angle between the frontal horizontal temperature gradient at 925hPa and the mean CNTL and SMTH SST gradients, in the region where there is a reduction in large-scale precipitation in Figure 4.11(d). Here, there is not a noticeable difference between the two sets of angles, which implies that the difference in effect of thermal damping between the two experiments is likely minimal. In Figure 4.13(b) however, this average angle is shown for the region where there is an increase in large-scale precipitation in Figure 4.11(d). In the SMTH case, the average angle south of 36N is roughly similar to the average north of 36N , and so the effect of thermal damping will be roughly similar. In the CNTL case however, there is a $\sim 100^\circ$ increase south of 36N , implying that cold fronts passing over this region are aligned almost exactly opposite to those in Figure 4.7(a), and hence strongly feel the effect of thermal damping. This observation is consistent with less fronts and large-scale precipitation in the CNTL experiment here and suggest the importance of

thermal damping in this region.

4.6.2 VERTICAL VELOCITY

Figure 4.14 shows a measure of the relative distribution across all days of vertical velocity at (a) 925hPa and (b) 500hPa for the constant longitude domain (70W, 29.7-43.2N) for the CNTL (red) and SMTH (black) experiments. This is done by first separating the data into bins of 0.1Pa s^{-1} between -13.5 and 4.5Pa s^{-1} , and then dividing by the total number of data points. It can be seen that the vast majority of the time, the vertical velocity falls between -1.5 and 1Pa s^{-1} , with a bias in the extreme tail towards stronger ascent than descent. As expected, the maximum values found at 500hPa are larger than those at 925hPa, most notably the ascent with values as large as $\sim -13\text{Pa s}^{-1}$. However, these extreme tails compress the bulk of the curve and make it difficult to assess the changes between the two experiments. For this reason, our following consideration of the relative vertical velocity distributions between the same five constant longitude domains used in Section 4.5 focus on the range -1 to 1Pa s^{-1} .

In a similar manner to Figure 4.14, a measure of the relative distribution across all days of low-level vertical velocity at 925hPa is shown in Figure 4.15 for the CNTL (red) and SMTH (black) experiments for (a) (70W, 29.7-43.2N) (b) (60W, 29.7-45.2N) (c) (50W, 29.7-49.7N), (d) (40W, 29.7-49.7N) and (e) (30W, 29.7-49.7N). Across all longitudes, in the SMTH experiment there is an increase in the occurrence of weaker vertical velocities (~ -0.1 to 0.1Pa s^{-1}) with respect to the CNTL experiment. This increase is expectedly met with a corresponding decrease in stronger vertical velocities (most noticeably around -0.3Pa s^{-1} and 0.3Pa s^{-1}), since the integral under each curve must equal unity. The magnitude of this change increases from 70W to 60W, stays at a similar level at 50W, then decreases out to 30W, where the change is significantly less.

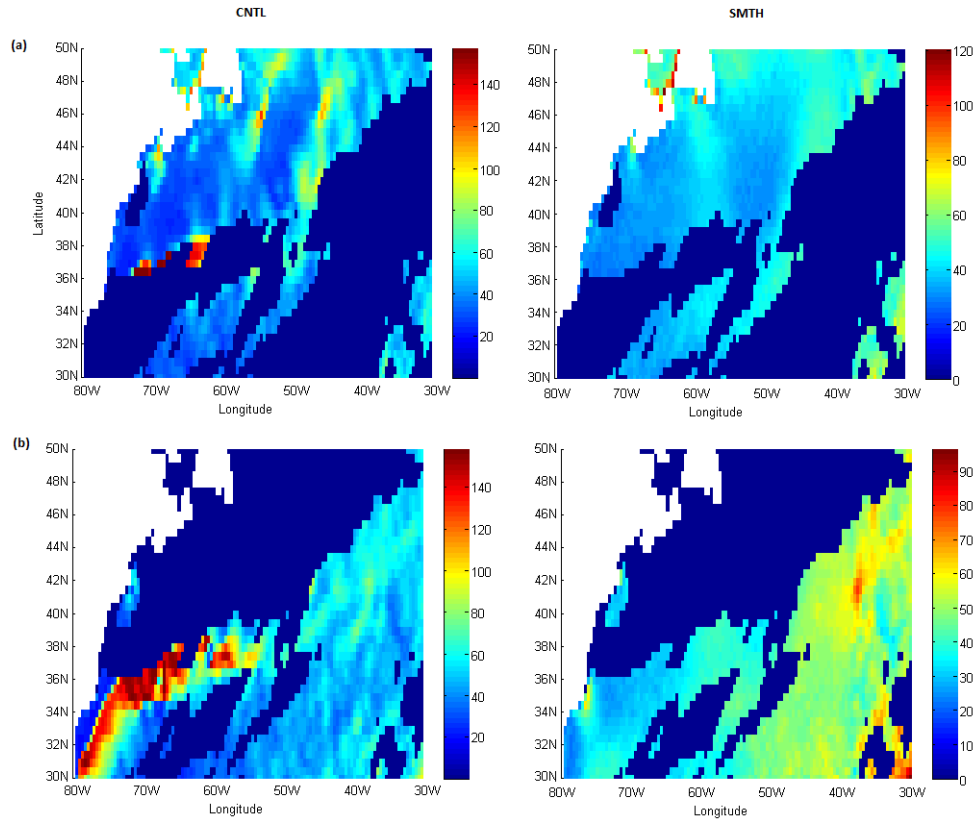


Figure 4.13: Average angle in wintertime between the frontal horizontal temperature gradient at 925hPa and the mean CNTL and mean SMTH SST gradients, for the regions where there is (a) an average reduction in large-scale precipitation in the SMTH experiment relative to the CNTL, and (b) an average increase in large-scale precipitation in the SMTH experiment relative to the CNTL. The broad dark blue areas represent the regions that are not under consideration in their respective plot.

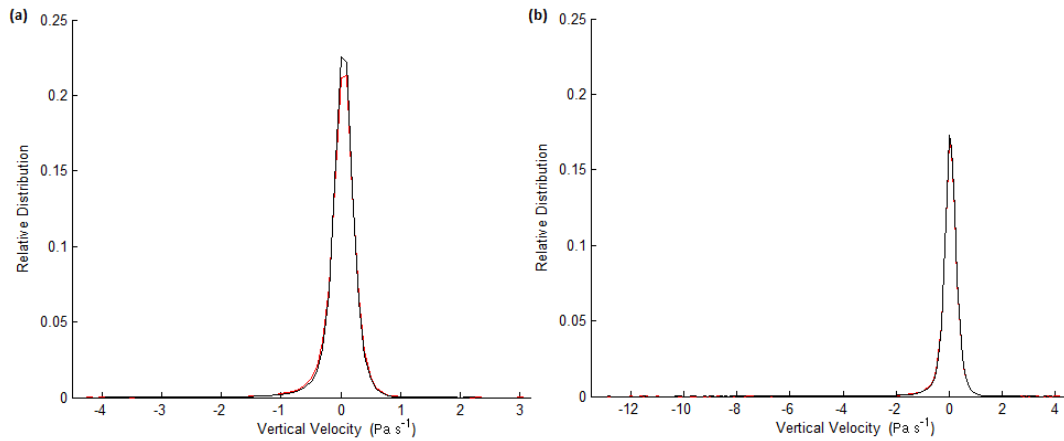


Figure 4.14: Relative distribution across all days of vertical velocity at (a) 925hPa and (b) 500hPa for the constant longitude domain (70W, 29.7-43.2N) for the CNTL (red) and SMTH (black) experiments.

This would appear to be consistent with the longitudinal profile of atmospheric front change in Figure 4.5(b).

This analysis is repeated in Figure 4.16 for the mid-level vertical velocity at 500hPa, where one finds larger vertical velocities than at low-level. This is indeed represented by a smaller relative distribution of weaker velocities and a widening of the curves towards the extreme ends. At 70W, 60W and 50W, there is still an increase in the distribution of weaker velocities in the SMTH experiment relative to the CNTL experiment, with the largest change again found at 60W and 50W. The magnitude of the change is smaller than at low-level however, meaning that the smoothing of the SST gradient is felt less at mid-levels. At 40W and 30W, there is almost no change whatsoever between the SMTH and CNTL profiles. This longitudinal behaviour at mid-level is mimicked at upper-level, as shown in Figure 4.17 for the vertical velocity at 300hPa. The velocities at upper-level are generally smaller than at mid-level however, leading to a larger relative distribution of weaker velocities in comparison. Once again,

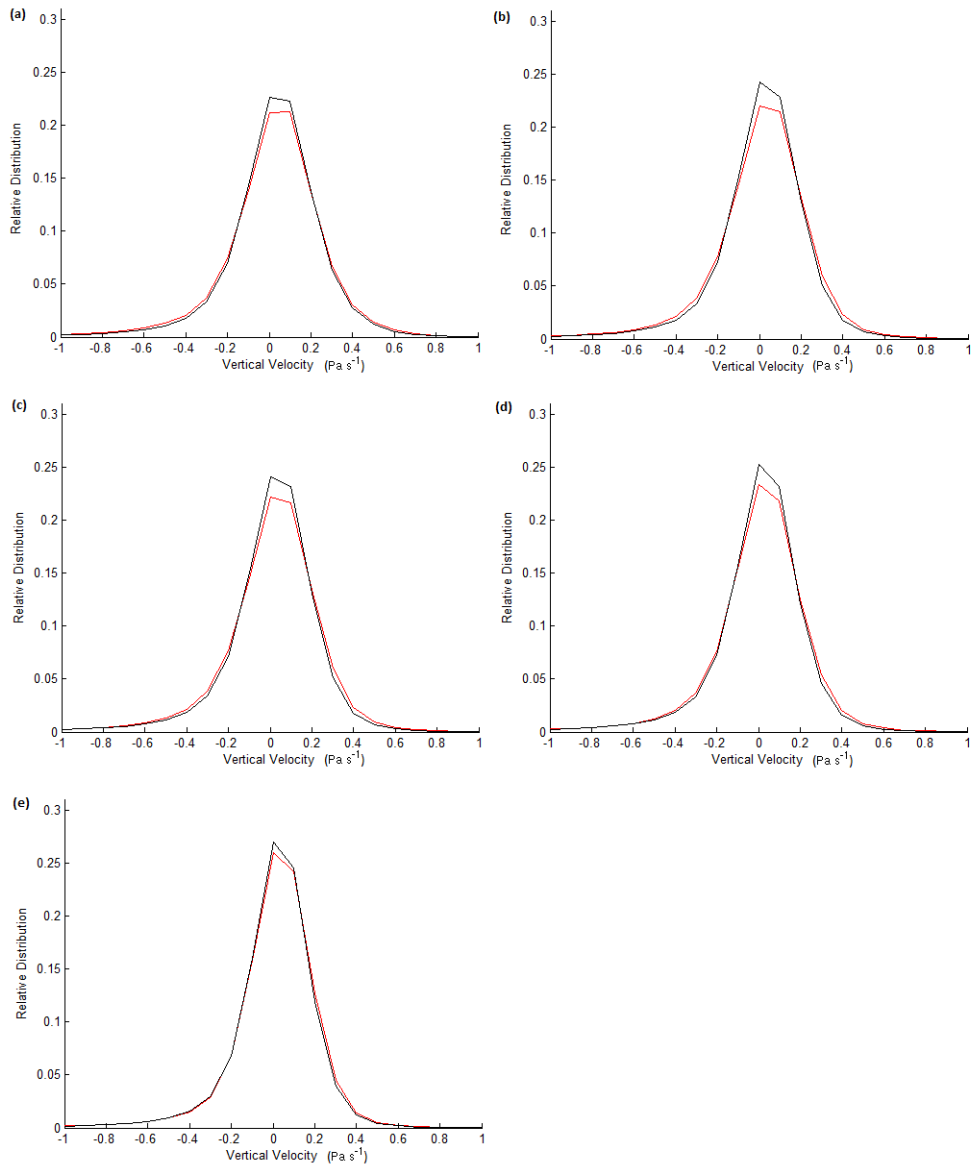


Figure 4.15: Relative distribution across all days of vertical velocity at 925hPa for the CNTL (red) and SMTH (black) experiments for the constant longitude domains (a) (70W, 29.7-43.2N) (b) (60W, 29.7-45.2N) (c) (50W, 29.7-49.7N), (d) (40W, 29.7-49.7N) and (e) (30W, 29.7-49.7N).

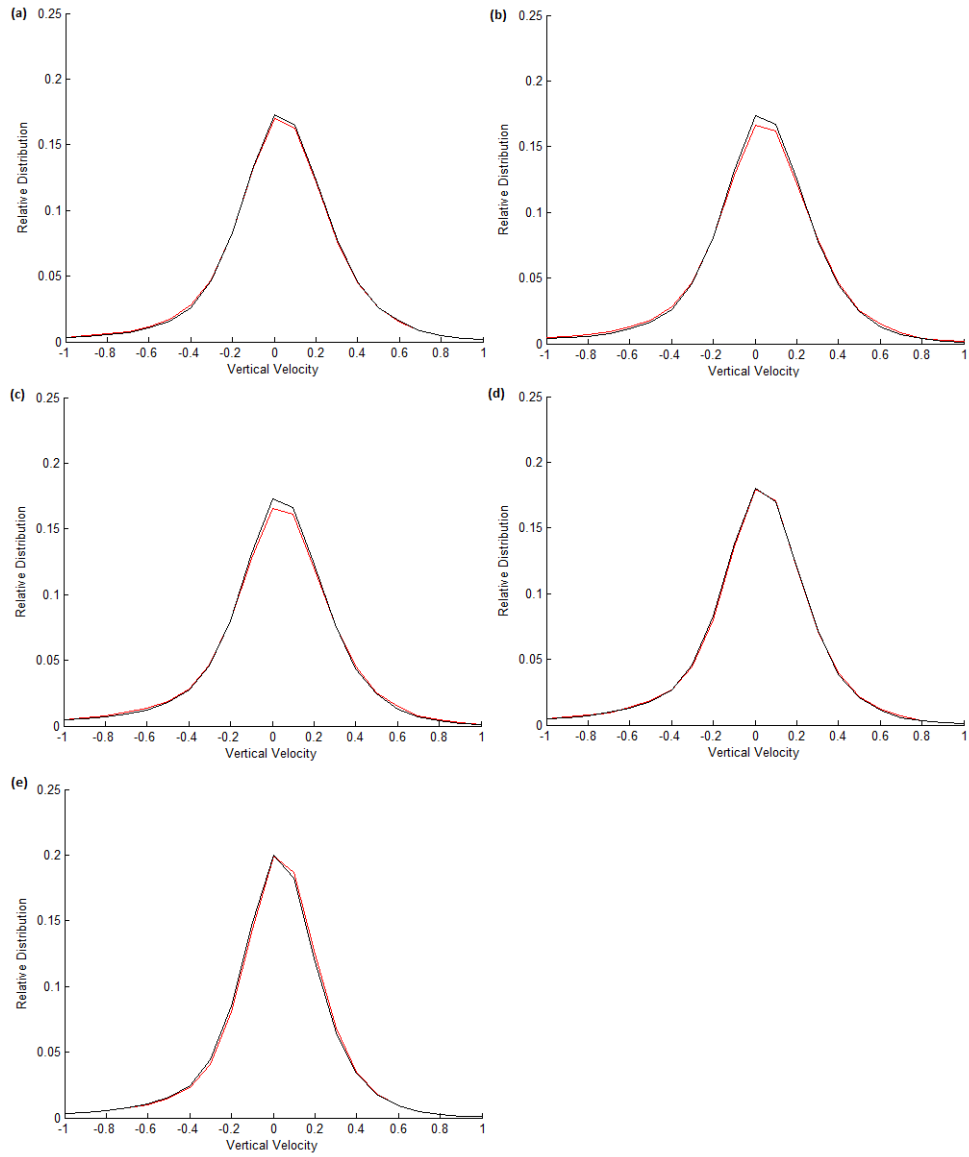


Figure 4.16: As in Figure 4.15, but for the vertical velocity at 500hPa.

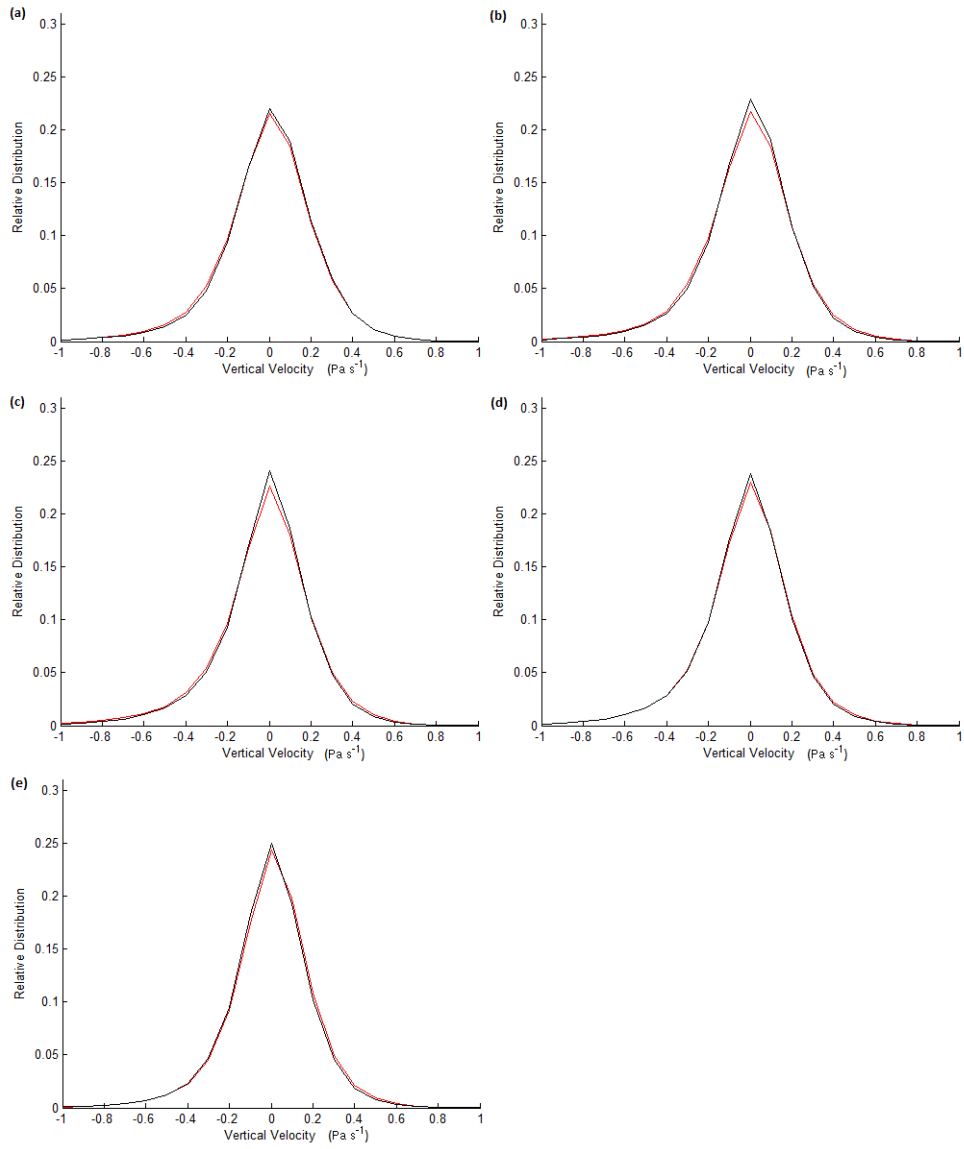


Figure 4.17: As in Figure 4.15, but for the vertical velocity at 300hPa.

the magnitude of any changes between the SMTH and CNTL profiles (i.e. the influence of the smoothing of the SST gradient) further decreases with height.

Figure 4.18 summarises the mean characteristics of the low-, mid- and upper-level vertical velocity in the GS region. The mean vertical velocity at 925hPa in the CNTL experiment (a) expectedly exhibits a meandering mean pattern of descent (ascent) on the colder (warmer) side of the GS front, with magnitudes up to $\sim 0.05 \text{ Pa s}^{-1}$. This mean pattern is reduced in magnitude to a large extent in the SMTH experiment, as seen in a plot of the reduction relative to the CNTL (b) (i.e. CNTL-SMTH). There is also a region of weaker ascent in the south-east section of the domain. It should be noted here that the magnitude of the mean in the CNTL experiment is larger by about a factor of two than those found in ERA-Interim observations at low-levels (ref. Figure 3.12(k), albeit for 950hPa). The cause for this difference is unknown, but it is possible that this is due to the difference in resolution scale used to produce the two sets of data (the resolution is higher in the AFES).

The mean vertical velocity at 500hPa in the CNTL experiment (b) demonstrates a broad region of ascent above the GS, with the average descent associated with the colder side of the GS front minimized over the ocean. Towards the south-east of the domain, there is again a region of descent. As at low-level, the magnitudes of each of these mean vertical velocities is significantly reduced in the SMTH experiment (d). It is noted that the pattern of change between the CNTL and SMTH experiments for mid-level vertical velocity is roughly the same as that for the large-scale precipitation (Figure 4.12 (d)). As expected, areas where there is a reduction (an increase) in mid-level ascent coincide with the areas that experience a reduction (an increase) in large-scale precipitation.

The mean vertical velocity at 300hPa in the CNTL experiment (c) has a broadly similar pattern to that at 500hPa, although the magnitudes are slightly

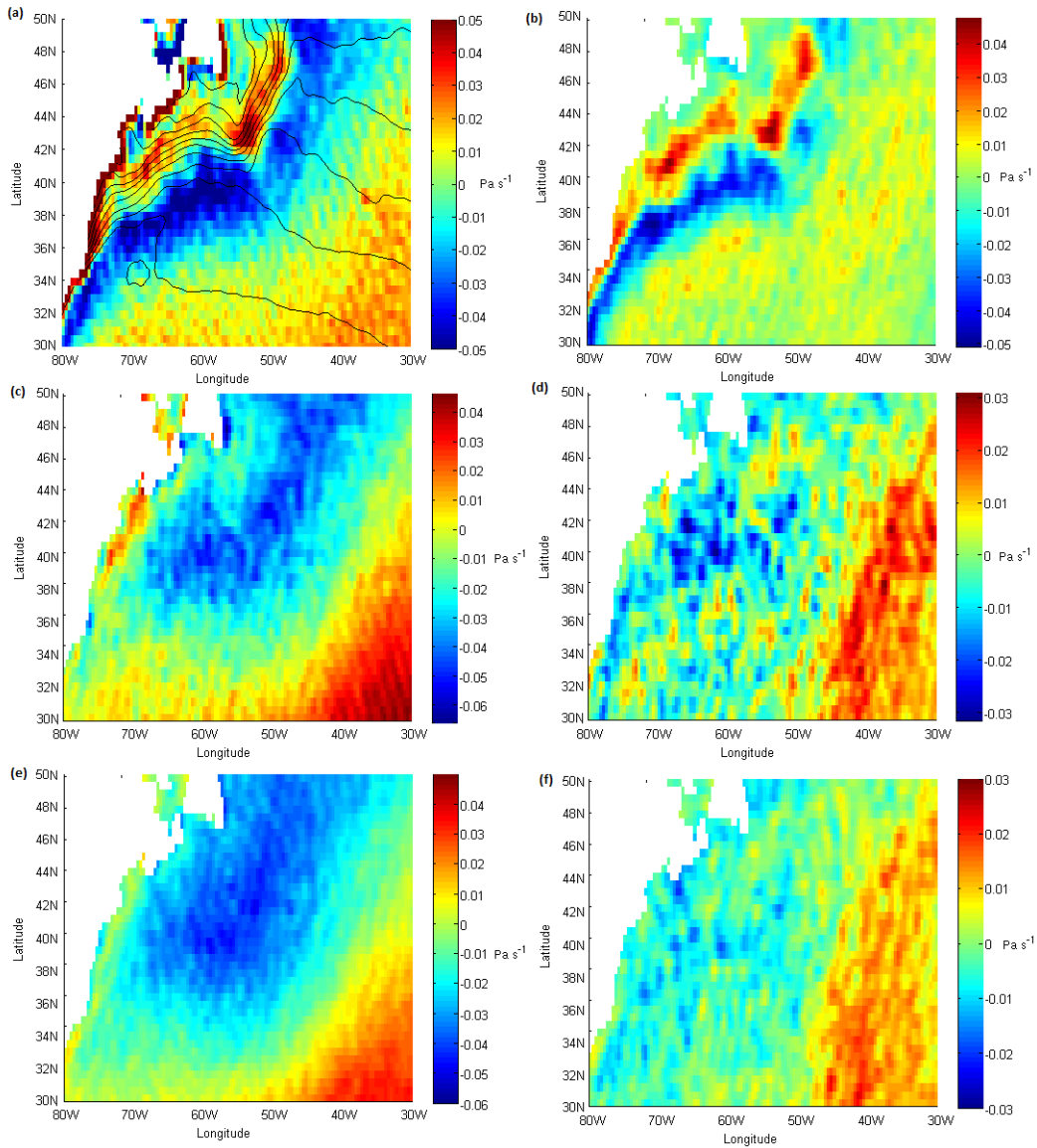


Figure 4.18: Twenty-year wintertime mean in (a) vertical velocity at 925hPa, (c) vertical velocity at 500hPa and (e) vertical velocity at 300hPa in the CNTL experiment. Mean contours of SST are shown in black. The average reduction in the SMTH experiment from the CNTL experiment is shown for the vertical velocity at (b) 925hPa, (d) 500hPa and (f) 300hPa.

smaller. The pattern of reduction is also broadly similar, except for again being smaller in magnitude. Although at low-, mid- and upper-level there is a significant reduction in the mean vertical velocities, this change does not dominate in Figure 4.15, Figure 4.16 or Figure 4.17. This is because the magnitude of the change in mean vertical velocity at both levels is on the order of $\sim 0.01 \text{ Pa s}^{-1}$, which is very small compared to a large proportion of the instantaneous vertical velocities found at any moment over the GS, which can be several orders of magnitude greater. In this manner, any noticeable change found in Figure 4.15, Figure 4.16 or Figure 4.17 is likely to reflect a change in the larger vertical velocities associated with frontal systems.

4.7 CONCLUSIONS

In this chapter, model 6-hourly data from the AFES is used to analyse twenty wintertime seasons over the GS for realistic (CNTL) and smoothed (SMTH) SST gradients. In particular, the effect that smoothing the SST gradient has on passing atmospheric fronts and the precipitation and vertical velocities associated with them is addressed. Firstly, defining atmospheric fronts by regions where $F \geq 1$ is shown in the CNTL experiment to produce occurrence rates consistent with other frontal detection methods ($\sim 10 - 20\%$). The occurrence rate increases as one travels upstream, as well as the average strength of the atmospheric fronts. Indeed, this is expected from the strong Eady growth rates present in the GS region. In the SMTH experiment, there is a broad and noticeable reduction ($\sim 25\%$) in the number of these atmospheric fronts north of 36N, coincident with the largest smoothing of the SST gradient. This reduction is consistent with the decrease in cyclone number density found in Minobe et al. (2008). However, just south of 36N, there is a region where an increase ($\sim 5\%$)

in the number of fronts is observed, although the magnitude of the increase is smaller. The percentage change in atmospheric front strength in both these regions is shown to affect fronts of all strengths the same.

In terms of precipitation, large-scale precipitation contributes a larger magnitude to the mean pattern than the convective precipitation, and also acts over a broader region. However the change in the mean pattern of precipitation that comes from smoothing the SST gradient is dominated by the change in convective precipitation ($\sim 150\%$ larger than the change in large-scale precipitation along the GS front), consistent with the results of Kuwano-Yoshida et al. (2010). Interestingly, the pattern of change in large-scale precipitation exhibits a dipole pattern around 36N , similar to that exhibited by the change in atmospheric front occurrence. Indeed, large-scale precipitation over the GS is associated with the WCBs in passing cyclonic warm sectors. In an attempt to explain why this dipole pattern may occur, the angle between the mean CNTL SST gradient and the mean SMTH SST gradient is examined. Across the majority of the GS, this angle is consistently small, but in the region where there is actually an increase in the number of fronts in the SMTH experiment, we see an extremely large difference in angle ($> 100^\circ$). Further analysis of the orientation of fronts with lines of constant longitude shows that at the corresponding longitudes (70W , 60W), there is no noticeable change in atmospheric front direction between the CNTL and SMTH experiment. However, at 50W , there is some evidence of a change in atmospheric front direction caused by a change in SST gradient. This frontal “steering” appears to be delayed by $\sim 10^\circ$; assuming associated storms travel at $\sim 10 \text{ m s}^{-1}$, this implies a timescale of roughly 1 day, consistent with a typical timescale for air-sea interactions. Once the perturbed front reaches 50W , where there is little change in SST gradient, there is again a delay of around 10° before it returns to its CNTL state (resulting in no noticeable change in

atmospheric front direction at 40W or 30W).

Indeed, given that there is no steering at 70W or 60W, atmospheric fronts in this region must on average be aligned very differently with the SST gradient in the CNTL and SMTH cases. This is shown to be true by examining the average angle of the frontal horizontal temperature gradient at 925hPa with the mean CNTL and SMTH SST gradients, divided into regions by the sign of the change in large-scale precipitation between the two experiments. In the SMTH experiment, this average angle is roughly the same in regions where there is both positive and negative change in large-scale precipitation. In the CNTL experiment however, in the region where there is less large-scale precipitation than in the SMTH, this average angle is extremely large ($> 100^\circ$). Here, atmospheric cold fronts (which are known from observations to be over twice as frequent in this region as warm fronts) will experience a major thermal damping effect due to the SST gradient, as colder (warmer) air will be interacting with relatively warm (cold) water. Indeed, this is consistent with less atmospheric fronts in the CNTL experiment, and such a clear dipole pattern suggests the significant importance of thermal damping on atmospheric fronts in this region.

For the low-level (925hPa), mid-level (500hPa) and upper-level (300hPa) vertical velocities, there are significant reductions in the mean patterns of ascent and descent found over the GS (over 50% in some regions). However, this shift is not significantly noticed when assessing the vertical velocity distributions across the twenty winter seasons, as it is several orders of magnitude smaller than those regularly found at atmospheric fronts. At low-level, at all longitudes there is an increase in weaker (~ -0.1 to 0.1 Pa s^{-1}) vertical velocities met with a corresponding decrease in stronger vertical velocities (most noticeably around ~ -0.3 to 0.3 Pa s^{-1}) when the SST gradient is smoothed. The magnitude of this change is smaller at 40W and 30W, where one encounters a more infrequent

frontal occurrence. At mid-level and upper-level, this change is present at 60W and 50W, although to a lesser extent, indicating the diminishing influence of the oceanic SST gradient higher in the troposphere. At 70W, 40W and 30W, there is no noticeable change in the mid-level and upper-level vertical velocity distributions.

CHAPTER 5

CONCLUSIONS

This thesis has attempted to assess the differences between days of varying ocean-atmosphere heat flux over the Gulf Stream in order to determine the mechanisms that contribute towards the mean atmospheric state in the region. Furthermore, the relationship between the individual atmospheric systems that propagate across this region and the underlying sea-surface temperature pattern has been explored.

In Chapter 2, a Lagrangian trajectory model was created, and subsequently verified quantitatively against a developing Eady (baroclinic) wave, and qualitatively against a realistic observation of warm conveyor belts. This model was used to study the direct thermal interaction between the ocean and the atmosphere over a Gulf Stream domain chosen to represent the area of greatest mean heat exchange, over thirty-three winter seasons (December-February 1979-2011). Two event sets are considered, based on an index of the domain-averaged daily heat flux: one representing the uppermost extreme (top 1% of index, EEs) and one representing the median (MEs). It is found that EEs are associated with an almost complete replacement of the marine air over the domain with continental air. This continental air is expectedly very cold and dry and experiences a large increase in moisture and temperature as it interacts with the warm oceanic water. Large anomalies in tropopause depth are present on these days, indicating cyclonic activity, and sharp increases in the boundary layer height lead to a significant reduction in the free troposphere.

The increase in thermal energy experienced by air parcels on these days over the Gulf Stream domain is almost entirely accounted for by the surface heat fluxes (99%), with negligible contribution from entrainment at the top of the boundary layer. At 12:00UTC on EEs, the surface heat fluxes over the Gulf Stream domain provide a total power of roughly equal 0.96PW, a magnitude that is significant on a global scale (Trenberth and Caron, 2001). On MEs, this power is only a third of this value (0.32PW). There is still considerable exchange between continental and marine air, but a reasonable fraction of air originates over the ocean, causing a reduced ocean-atmosphere heat exchange. There are no analogous anomalies in tropopause depth or boundary layer height, and the air is relatively slow compared to that found on EEs. The majority of the thermal energy increase experienced by the air over the domain still comes from the surface heat fluxes, but there is a non-negligible contribution from entrainment also (17%). Whilst it is promising that the entrainment flux contribution found on MEs is consistent with previous equilibrium-state measurements (Fedorovich et al., 2004), a clear area for improvement comes with the addition of theoretical calculations for the entrainment flux. Naturally, applying contributions in the Lagrangian trajectory model for turbulent and mesoscale wind fluctuations would also further increase the accuracy of the results.

In Chapter 3, it was shown that roughly 90% of the time, one observes either the passing of a cyclone or an anti-cyclone over the Gulf Stream domain defined in Chapter 2, indicating the presence of a continuous baroclinic waveguide of varying strength. The stronger the cyclone (anticyclone), the stronger (weaker) the domain-averaged ocean-atmosphere heat flux. The mean state in both convective and large-scale precipitation is set by these two opposite regimes, with the precipitation overwhelmingly associated with cyclonic activity. On days of stronger (weaker) heat flux, a cyclone is present to the east (west) of the domain,

exhibiting values much larger than those found in the mean. Indeed, the top and bottom 20% of heat flux events, as defined in Chapter 2, can both account for up to 50% of the mean precipitation locally (depending on the location of the cyclone). This baroclinic waveguide also determines the mean pattern in vertical velocity throughout the entire troposphere. Again, the magnitude of the vertical velocities found in these two opposite regimes is much larger than those found in the mean. Unlike precipitation however, vertical velocity can have both positive and negative sign. It would therefore not be unreasonable to expect that such an alternating series of vertical velocities would cancel, leaving the residual pattern found on the 10% of days when there is no appreciable synoptic activity. However, consideration of a typical deep tropospheric motion system (as in Green et al., 1966) suggests that the pattern of ascent and descent would indeed be markedly asymmetrical due to the descending motion being without boundary and limited to the slow rate determined by radiative heat loss.

Additionally in this chapter, a potential mechanism is introduced whereby the SST gradient could interact with a cyclone and subsequently alter the precipitation rate. Observations of EEs (as defined in Chapter 2) indicate the presence of a strong negative (Ertel-Rossby) potential vorticity anomaly in the cyclonic cold sector. This creates a potential vorticity gradient between the cold sector and the warm sector ahead of it. It is suggested that altering the sea-surface temperature gradient subsequently changes this gradient of potential vorticity through anomalies in the surface heat fluxes, thereby affecting the surrounding isentropes and any subsequent vertical motion. Research is ongoing at Imperial College to test this hypothesis. Further related research is also being done, including work to find an indicator of the cold sector using potential vorticity that could be used to partition precipitation occurring behind the cold front. At the time of writing, it has been found using the Meteorological

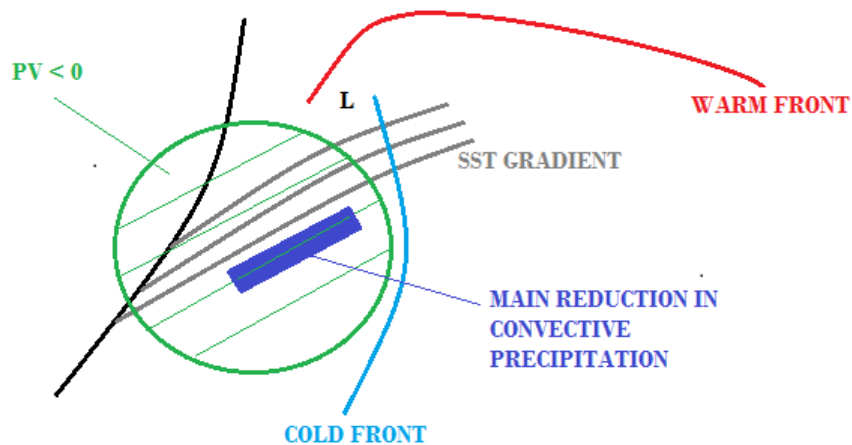


Figure 5.1: Schematic showing a cyclone passing over the Gulf Stream. A smoothing of the SST gradient, as in Minobe et al. (2008), reduces the convective available potential energy on the warm side of the Gulf Stream, resulting in the largest region of reduction in convective precipitation. Colocated with a broad area of the cold sector is a region of negative PV.

Office Unified Model that in the cold sector of a cyclone passing over the Gulf Stream, dry and cold air parcels acquire more buoyancy over the warm side of the strong sea-surface temperature gradient, acting to increase the convective available potential energy. This destabilizes the atmospheric column and leads to enhanced convective precipitation. Smoothing the SST gradient results in a sharp decrease in the convective precipitation in this region, which accounts for the main reduction in the mean wintertime precipitation over the Gulf Stream observed in Kuwano-Yoshida et al., (2010) (Figure 5.1, Benoît Vannière, Personal comm., 2014).

In Chapter 4, the relationship between sea-surface temperature gradient and atmospheric fronts, and their associated vertical velocities and precipitation is further explored. This is done by using model data from the Atmospheric General Circulation Model for the Earth Simulator for twenty wintertime seasons over the Gulf Stream for realistic (CNTL) and smoothed (SMTH) sea-surface

temperature gradients. Analysis shows that smoothing the sea-surface temperature gradient broadly reduces the number of atmospheric fronts, up to around 30% in the region where there is the largest reduction in gradient. As expected, it is shown that atmospheric fronts intensify as they travel upstream. The relative percentage of reduction in front intensity between the two experiments is the same for fronts of all strengths. Considering longitudinal profiles shows that at low-levels this front intensity decrease results in a corresponding reduction in the occurrence of stronger vertical velocities. This effect can also be seen at mid- and upper-level, but to a lesser extent, indicating the influence of the sea-surface temperature gradient decreases with height.

However, there is also a region where the number of fronts is increased. In this region in the SMTH experiment, the average angle between fronts and the mean sea-surface temperature gradient is roughly the same as where there is a marked decrease in fronts. In the CNTL case, there is a sharp increase in this angle in this region. This has the effect of aligning atmospheric cold fronts in such a way that they experience an extremely large amount of thermal damping. Considering that in general, more cold fronts are found in the GS region than warm fronts (Berry et al., 2011), our analysis will represent more heavily the behaviour of cold fronts, and this observation is then consistent with strong thermal damping leading to a significant reduction in front strength. The significant change in orientation of the mean SST gradient between the CNTL and SMTH experiment in this region is also observed to produce a "steering" of atmospheric fronts (i.e. alter the direction of frontal propagation). This effect is exhibited on a timescale typical of air-sea interactions. On that same timescale, the perturbed front is then observed to return to its CNTL state once passing over regions where there is no significant change in mean SST gradient direction.

Smoothing the sea-surface temperature gradient also leads to a change in

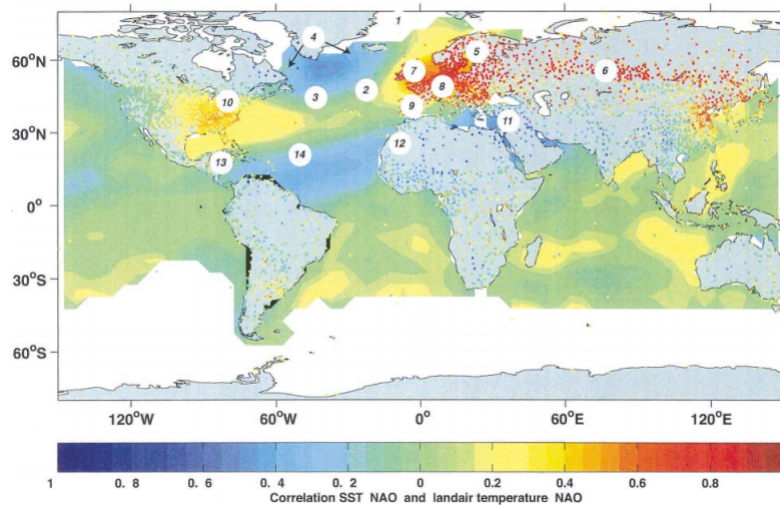


Figure 5.2: Correlation between the December-March North Atlantic Oscillation index and global surface temperature (SST is used over the oceans) (Marshall et al., 2001).

the mean pattern of precipitation. Although the large-scale precipitation is originally stronger and broader, the reduction in the mean pattern is dominated by the convective precipitation. Interestingly however, the change in large-scale precipitation exhibits the same dipole pattern in terms of sign as the change in front intensity between the two experiments discussed earlier. This lends further evidence to the effect of thermal damping in this region. This dipole pattern in sign is also exhibited in the change in sea-surface temperature; combined with the aforementioned shift observed between the two experiments in the direction of frontal propagation at 50W, the potential for some exciting future work is opened. Indeed, it is known that a change in the phase of the North Atlantic Oscillation (i.e. a tilt in orientation of the storm-track over the North Atlantic) causes an SST tripole anomaly in the North Atlantic (Figure 5.2, Marshall et al., 2001). These anomalies, whilst not located exactly as in the present analysis, could reasonably be considered in the same manner as the change between the

CNTL and SMTH experiments. The analysis in this chapter suggests that such an anomaly would noticeably affect both the strength and propagation direction of passing atmospheric fronts, which offers a potential mechanism for positive oceanic feedback on the North Atlantic Oscillation.

Bibliography

- Adamson, D. S., Belcher, S. E., Hoskins, B. J., & Plant, R. S. (2006). Boundary layer friction in midlatitude cyclones. *Quarterly Journal of the Royal Meteorological Society*, 132(614), 101-124.
- Alexander, M. A., & Scott, J. D. (1997). Surface flux variability over the North Pacific and North Atlantic oceans. *Journal of climate*, 10(11), 2963-2978.
- Angevine, W. M. (1999). Entrainment results including advection and case studies from the Flatland boundary layer experiments. *Journal of Geophysical Research: Atmospheres* (1984–2012), 104(D24), 30947-30963.
- Arnold, F., Schneider, J., Gollinger, K., Schlager, H., Schulte, P., Hagen, D. E., Whitefield, P.D., & Van Velthoven, P. (1997). Observation of upper tropospheric sulfur dioxide and acetone pollution: Potential implications for hydroxyl radical and aerosol formation. *Geophysical research letters*, 24(1), 57-60.
- Berrisford, P., Dee, D. P. K. F., Fielding, K., Fuentes, M., Källberg, P., Kobayashi, S., & Uppala, S. (2009). The ERA-Interim Archive. ERA report series, (1), 1-16.
- Berry, G., Reeder, M. J., & Jakob, C. (2011). A global climatology of atmospheric fronts. *Geophysical Research Letters*, 38(4).
- Bjerknes, J. (1919). On the structure of moving cyclones. *Monthly Weather Review*, 47(2), 95-99.

Bjerknes, J. (1964). Atlantic air-sea interaction. *Advances in geophysics*, 10(1), 82.

Bjerknes, J., & Solberg, H. (1922). Life cycle of cyclones and the polar front theory of atmospheric circulation. *Geophys. Publ.* 3(1), 1-18.

Blackmon, M. L., Wallace, J. M., Lau, N. C., & Mullen, S. L. (1977). An observational study of the Northern Hemisphere wintertime circulation. *Journal of the Atmospheric Sciences*, 34(7), 1040-1053.

Booth, J. F., Thompson, L., Patoux, J., Kelly, K. A., & Dickinson, S. (2010). The signature of the midlatitude tropospheric storm tracks in the surface winds. *Journal of Climate*, 23(5).

Boutle, I. A., Beare, R. J., Belcher, S. E., Brown, A. R., & Plant, R. S. (2010). The moist boundary layer under a mid-latitude weather system. *Boundary-layer meteorology*, 134(3), 367-386.

Boutle, I. A., Belcher, S. E., & Plant, R. S. (2011). Moisture transport in midlatitude cyclones. *Quarterly Journal of the Royal Meteorological Society*, 137(655), 360-373.

Bretherton, F. P. (1966). Critical layer instability in baroclinic flows. *Quarterly Journal of the Royal Meteorological Society*, 92(393), 325-334.

Browning, K. A. (1986). Conceptual models of precipitation systems. *Weather*

and Forecasting, 1(1), 23-41.

Browning, K. A. (1990). Organization of clouds and precipitation in extratropical cyclones. *Extratropical Cyclones: The Erik Palmén Memorial Volume*, 129-153.

Browning, K. A., Roberts, N. M., & Illingworth, A. J. (1997). Mesoscale analysis of the activation of a cold front during cyclogenesis. *Quarterly Journal of the Royal Meteorological Society*, 123(544), 2349-2374.

Businger, S., Graziano, T. M., Kaplan, M. L., & Rozumalski, R. A. (2005). Cold-air cyclogenesis along the Gulf-Stream front: investigation of diabatic impacts on cyclone development, frontal structure, and track. *Meteorology and Atmospheric Physics*, 88(1-2), 65-90.

Carlson, T. N. (1980). Airflow through midlatitude cyclones and the comma cloud pattern. *Monthly Weather Review*, 108(10), 1498-1509.

Catto, J. L., & Pfahl, S. (2013). The importance of fronts for extreme precipitation. *Journal of Geophysical Research: Atmospheres*, 118(19), 10-791.

Cayan, D. R. (1992). Latent and sensible heat flux anomalies over the northern oceans: Driving the sea surface temperature. *Journal of Physical Oceanography*, 22(8), 859-881.

Chang, E. K., Lee, S., & Swanson, K. L. (2002). Storm track dynamics. *Journal of Climate*, 15(16).

Charney, JG (1947): The dynamics of long waves in a baroclinic westerly current. *Journal of Meteorology* 4, 135–62

Chelton, D. B., Schlax, M. G., Freilich, M. H., & Milliff, R. F. (2004). Satellite measurements reveal persistent small-scale features in ocean winds. *Science*, 303(5660), 978-983.

Chen, S. J., Kuo, Y. H., Zhang, P. Z., & Bai, Q. F. (1992). Climatology of explosive cyclones off the east Asian coast. *Monthly weather review*, 120(12), 3029-3035.

Cione, J. J., Raman, S., & Pietrafesa, L. J. (1993). The effect of Gulf Stream-induced baroclinicity on US East Coast winter cyclones. *Monthly weather review*, 121(2), 421-430.

Clayson et al.. SeaFlux Version 1 Documentation. Available at:
http://seaflex.org/seaflex_data/DOCUMENTATION/Seaflux_final.pdf

Colucci, S. J. (1976). Winter Cyclone Frequencies over the Eastern United States and Adjacent Western Atlantic,-. *Bulletin of the American Meteorological Society*, 57(5), 548-553.

Cooper, I. M., Thorpe, A. J., & Bishop, C. H. (1992). The role of diffusive effects on potential vorticity in fronts. *Quarterly Journal of the Royal Meteorological Society*, 118(506), 629-647.

Czaja, A., & Blunt, N. (2011). A new mechanism for ocean–atmosphere coupling in midlatitudes. *Quarterly Journal of the Royal Meteorological Society*, 137(657), 1095-1101.

Czaja, A., & Frankignoul, C. (2002). Observed impact of Atlantic SST anomalies on the North Atlantic Oscillation. *Journal of Climate*, 15(6).

Davis, C. A., & Emanuel, K. A. (1991). Potential vorticity diagnostics of cyclogenesis. *Monthly weather review*, 119(8), 1929-1953.

Deser, C., Alexander, M. A., & Timlin, M. S. (2003). Understanding the persistence of sea surface temperature anomalies in midlatitudes. *Journal of Climate*, 16(1).

Draxler, R. R., & Hess, G. D. (1997). Description of the HYSPLIT4 modeling system.

Eady, E. T. (1949). Long waves and cyclone waves. *Tellus*, 1(3), 33-52.

Eckhardt, S., Stohl, A., Wernli, H., James, P., Forster, C., & Spichtinger, N. (2004). A 15-year climatology of warm conveyor belts. *Journal of climate*, 17(1).

ECMWF, E. (2009). IFS documentation CY33r1. part IV, Tech. rep., ECMWF, available at: http://www.ecmwf.int/research/ifsdocs/CY33r1/PHYSICS/IFS_Part4.pdf.

Ekman, V. W. (1905). On the influence of the earth's rotation on ocean cur-

rents. *Ark. Mat. Astron. Fys.*, 2, 1-53.

Eliassen, A. (1962). On the vertical circulation in frontal zones. *Geofys. Publ.*, 24(4), 147-160.

Emanuel, K. (1994). *Atmospheric convection*. Oxford University Press.

Enomoto, T., Kuwano-Yoshida, A., Komori, N., & Ohfuchi, W. (2008). Description of AFES 2: Improvements for high-resolution and coupled simulations. In *High Resolution Numerical Modelling of the Atmosphere and Ocean* (pp. 77-97). Springer New York.

Ertel, H. (1942). Ein neuer hydrodynamischer Wirbelsatz. *Meteorol. Z.*, 59, 277-281.

Esbensen, S. K., & Kushnir, Y. (1981). The heat budget of the global ocean: An atlas based on estimates from surface marine observations (No. 29). Oregon State University.

Fedorovich, E., Conzemius, R., & Mironov, D. (2004). Convective entrainment into a shear-free, linearly stratified atmosphere: Bulk models reevaluated through large eddy simulations. *Journal of the atmospheric sciences*, 61(3).

Giordani, H., & Caniaux, G. (2001). Sensitivity of cyclogenesis to sea surface temperature in the northwestern Atlantic. *Monthly weather review*, 129(6), 1273-1295.

Green, J. S. A., Ludlam, F. H., & McIlveen, J. F. R. (1966). Isentropic relative flow analysis and the parcel theory. *Quarterly Journal of the Royal Meteorological Society*, 92(392), 210-219.

Grodsky, Semyon A., Abderrahim Bentamy, James A. Carton, Rachel T. Pinker, (2009): Intraseasonal Latent Heat Flux Based on Satellite Observations. *J. Climate*, 22, 4539–4556.

Gupta, S., McNider, R. T., Trainer, M., Zamora, R. J., Knupp, K., & Singh, M. P. (1997). Nocturnal wind structure and plume growth rates due to inertial oscillations. *Journal of Applied Meteorology*, 36(8), 1050-1063.

Harrold, T. W. (1973). Mechanisms influencing the distribution of precipitation within baroclinic disturbances. *Quarterly Journal of the Royal Meteorological Society*, 99(420), 232-251.

Hawcroft, M. K., Shaffrey, L. C., Hodges, K. I., & Dacre, H. F. (2012). How much Northern Hemisphere precipitation is associated with extratropical cyclones? *Geophysical Research Letters*, 39(24).

Haynes, P. H., & McIntyre, M. E. (1987). On the evolution of vorticity and potential vorticity in the presence of diabatic heating and frictional or other forces. *Journal of the atmospheric sciences*, 44(5), 828-841.

Hewson, T. D. (1998). Objective fronts. *Meteorological Applications*, 5(01), 37-65.

Hoskins, B. J. (1982). The mathematical theory of frontogenesis. *Annual review of fluid mechanics*, 14(1), 131-151.

Hoskins, B. J., & Hodges, K. I. (2002). New perspectives on the Northern Hemisphere winter storm tracks. *Journal of the Atmospheric Sciences*, 59(6).

Hoskins, B. J., & Valdes, P. J. (1990). On the existence of storm-tracks. *Journal of the atmospheric sciences*, 47(15), 1854-1864.

Hoskins, B. J., James, I. N., & White, G. H. (1983). The shape, propagation and mean-flow interaction of large-scale weather systems. *Journal of the atmospheric sciences*, 40(7), 1595-1612.

Hoskins, B. J., McIntyre, M. E., & Robertson, A. W. (1985). On the use and significance of isentropic potential vorticity maps. *Quarterly Journal of the Royal Meteorological Society*, 111(470), 877-946.

Huang, J., Lee, X., & Patton, E. G. (2011). Entrainment and budgets of heat, water vapor, and carbon dioxide in a convective boundary layer driven by time varying forcing. *Journal of Geophysical Research: Atmospheres* (1984–2012), 116(D6).

Josey, S. A. (2001). A comparison of ECMWF, NCEP-NCAR, and SOC surface heat fluxes with moored buoy measurements in the subduction region of the northeast Atlantic. *Journal of Climate*, 14(8), 1780-1789.

Josey, S. A., Kent, E. C., & Taylor, P. K. (1999). *New Insights into the Ocean*

Heat Budget Closure Problem from Analysis of the SOC Air–Sea Flux Climatology. *Journal of Climate*, 12(9).

Kållberg, P. (2011). Forecast drift in ERA-Interim. European Centre for Medium Range Weather Forecasts.

Kållberg, P., Berrisford, P., Hoskins, B., Simmons, A., Lamy-Thépaut, S. and Hine, R. (2005). ERA-40 atlas.

Kobashi, F., Xie, S. P., Iwasaka, N., & Sakamoto, T. T. (2008). Deep atmospheric response to the North Pacific oceanic subtropical front in spring. *Journal of Climate*, 21(22).

Konda, M., Ichikawa, H., Tomita, H., & Cronin, M. F. (2010). Surface Heat Flux Variations across the Kuroshio Extension as Observed by Surface Flux Buoys. *Journal of Climate*, 23(19).

Kuwano-Yoshida, A., Minobe, S., & Xie, S. P. (2010). Precipitation Response to the Gulf Stream in an Atmospheric GCM*. *Journal of Climate*, 23(13).

Lindzen, R. S., & Nigam, S. (1987). On the role of sea surface temperature gradients in forcing low-level winds and convergence in the tropics. *Journal of the Atmospheric Sciences*, 44(17), 2418-2436.

Liu, V. C. (1956). Turbulent dispersion of dynamic particles. *Journal of Meteorology*, 13(4), 399-405.

Liu, W. T., Xie, X., & Niiler, P. P. (2007). Ocean–Atmosphere Interaction over Agulhas Extension Meanders. *Journal of Climate*, 20(23).

Madonna, E., Wernli, H., Joos, H., & Martius, O. (2014). Warm Conveyor Belts in the ERA-Interim Dataset (1979-2010). Part I: Climatology and Potential Vorticity Evolution. *Journal of Climate*, 27(1).

Marshall, J., Kushnir, Y., Battisti, D., Chang, P., Czaja, A., Dickson, R., Hurrell, J., McCartney M., Saravanan, R., & Visbeck, M. (2001). North Atlantic climate variability: phenomena, impacts and mechanisms. *International Journal of Climatology*, 21(15), 1863-1898.

Massacand, A. C., Wernli, H., & Davies, H. C. (2001). Influence of upstream diabatic heating upon an Alpine event of heavy precipitation. *Monthly weather review*, 129(11), 2822-2828.

Minobe, S., Kuwano-Yoshida, A., Komori, N., Xie, S. P., & Small, R. J. (2008). Influence of the Gulf Stream on the troposphere. *Nature*, 452(7184), 206-209.

Morgan, M. C., & Nielsen-Gammon, J. W. (1998). Using tropopause maps to diagnose midlatitude weather systems. *Monthly weather review*, 126(10).

Nakamura, H., Sampe, T., Goto, A., Ohfuchi, W., & Xie, S. P. (2008). On the importance of midlatitude oceanic frontal zones for the mean state and dominant variability in the tropospheric circulation. *Geophysical Research Letters*, 35(15).

Nakamura, H., Sampe, T., Tanimoto, Y., & Shimpō, A. (2004). Observed associations among storm tracks, jet streams and midlatitude oceanic fronts. *Geophysical Monograph Series*, 147, 329-345.

Nakamura, H., Ya, P., Shimpō, A., & Ya, P. (2004). Seasonal variations in the Southern Hemisphere storm tracks and jet streams as revealed in a reanalysis dataset. *Journal of Climate*, 17(9).

National Oceanography Centre. Southampton, United Kingdom. <http://noc.ac.uk>.

Nonaka, M., & Xie, S. P. (2003). Covariations of sea surface temperature and wind over the Kuroshio and its extension: Evidence for ocean-to-atmosphere feedback. *Journal of climate*, 16(9).

Ohfuchi, W., Nakamura, H., Yoshioka, M. K., Enomoto, T., Takaya, K., Peng, X., Yamane, S., Nishimura, T., Kurihara, Y., & Ninomiya, K. (2004). 10-km mesh meso-scale resolving simulations of the global atmosphere on the Earth Simulator: Preliminary outcomes of AFES (AGCM for the Earth Simulator). *J. Earth Simulator*, 1, 8-34.

Palmén, E. (1958). Vertical circulation and release of kinetic energy during the development of Hurricane Hazel into an extratropical storm. *Tellus*, 10(1), 1-23.

Pauluis, O., & Held, I. M. (2002). Entropy Budget of an Atmosphere in Radiative–Convective Equilibrium. Part II: Latent Heat Transport and Moist Processes. *Journal of the Atmospheric sciences*, 59(2).

Pauluis, O., Czaja, A., & Korty, R. (2010). The global atmospheric circulation in moist isentropic coordinates. *Journal of Climate*, 23(11).

Persson, P. O. G., J. E. Hare, L.B. Nance, and B. Walter (2008): Impact of air-sea interaction on extra-tropical cyclones. *Proc. ECMWF Workshop on Ocean-Atmosphere Interactions*, Reading, United Kingdom, ECMWF, 123-146.

Pfahl, S., Madonna, E., Boettcher, M., Joos, H., & Wernli, H. (2014). Warm Conveyor Belts in the ERA-Interim Dataset (1979-2010). Part II: Moisture Origin and Relevance for Precipitation. *Journal of Climate*, 27(1).

Plant, R. S., & Belcher, S. E. (2007). Numerical Simulation of Baroclinic Waves with a Parameterized Boundary Layer. *Journal of the Atmospheric Sciences*, 64(12).

Reed, R. J., & Danielsen, E. F. (1958). Fronts in the vicinity of the tropopause. *Archiv für Meteorologie, Geophysik und Bioklimatologie, Serie A*, 11(1), 1-17.

Reed, R. J., & Sanders, F. (1953). An investigation of the development of a mid-tropospheric frontal zone and its associated vorticity field. *Journal of Meteorology*, 10(5), 338-349.

Rodwell, M. J., Rowell, D. P., & Folland, C. K. (1999). Oceanic forcing of the wintertime North Atlantic Oscillation and European climate. *Nature*, 398(6725), 320-323.

Rossby, C. G. (1936). Dynamics of steady ocean currents in the light of exper-

imental fluid mechanics.

Rossby, C. G. (1940). Planetary flow patterns in the atmosphere. *Quart. J. Roy. Meteor. Soc*, 66, 68-87.

Sampe, T., & Xie, S. P. (2007). Mapping high sea winds from space. *Bulletin of the American Meteorological Society*, 88(12).

Sanders, F. (1986). Explosive cyclogenesis in the west-central North Atlantic Ocean, 1981-84. Part I: Composite structure and mean behavior. *Monthly weather review*, 114(10), 1781-1794.

Savijärvi, H. (2006). Radiative and turbulent heating rates in the clear air boundary layer. *Quarterly Journal of the Royal Meteorological Society*, 132(614), 147-161.

Shaman, J., Samelson, R. M., & Skyllingstad, E. (2010). Air–Sea Fluxes over the Gulf Stream Region: Atmospheric Controls and Trends. *Journal of Climate*, 23(10).

Shapiro, M. A., & Keyser, D. A. (1990). Fronts, jet streams, and the tropopause. US Department of Commerce, National Oceanic and Atmospheric Administration, Environmental Research Laboratories, Wave Propagation Laboratory.

Sheldon, L., Czaja, A., & Casado, M. (2013). Slantwise instability over the Gulf Stream.

Simmons, A. J., & Hoskins, B. J. (1979). The downstream and upstream development of unstable baroclinic waves. *Journal of the Atmospheric Sciences*, 36(7), 1239-1254.

Sinclair, V. A., Belcher, S. E., & Gray, S. L. (2010). Synoptic controls on boundary-layer characteristics. *Boundary-layer meteorology*, 134(3), 387-409.

Sinclair, V. A., Gray, S. L., & Belcher, S. E. (2008). Boundary layer ventilation by baroclinic life cycles. *Quarterly Journal of the Royal Meteorological Society*, 134(635), 1409-1424.

Song, Q., Cornillon, P., & Hara, T. (2006). Surface wind response to oceanic fronts. *Journal of Geophysical Research: Oceans (1978–2012)*, 111(C12).

Stoelinga, M. T. (1996). A potential vorticity-based study of the role of diabatic heating and friction in a numerically simulated baroclinic cyclone. *Monthly weather review*, 124(5), 849-874.

Stohl, A. (1998). Computation, accuracy and applications of trajectories—a review and bibliography. *Atmospheric Environment*, 32(6), 947-966.

Stohl, A., Haimberger, L., Scheele, M. P., & Wernli, H. (2001). An intercomparison of results from three trajectory models. *Meteorological Applications*, 8(2), 127-135.

Stohl, A., Eckhardt, S., Forster, C., James, P., & Spichtinger, N. (2002). On the pathways and timescales of intercontinental air pollution transport. *Journal*

of Geophysical Research: Atmospheres (1984–2012), 107(D23), ACH-6.

Stohl, A., Hittenberger, M., & Wotawa, G. (1998). Validation of the Lagrangian particle dispersion model FLEXPART against large-scale tracer experiment data. *Atmospheric Environment*, 32(24), 4245-4264.

Stohl, A., Wotawa, G., Seibert, P., & Kromp-Kolb, H. (1995). Interpolation errors in wind fields as a function of spatial and temporal resolution and their impact on different types of kinematic trajectories. *Journal of Applied Meteorology*, 34(10), 2149-2165.

Stommel, H. (1948). The westward intensification of wind-driven ocean currents. *Trans. Amer. Geophys. Union*, 29(2), 202-206.

Stull, R. B. (1988), *An Introduction to Boundary Layer Meteorology*, pp. 666, Kluwer Acad., Norwell, Mass.

Sweet, W., Fett, R., Kerling, J., & La Violette, P. (1981). Air-sea interaction effects in the lower troposphere across the north wall of the Gulf Stream. *Monthly Weather Review*, 109(5), 1042-1052.

Taguchi, B., Nakamura, H., Nonaka, M., & Xie, S. P. (2009). Influences of the Kuroshio/Oyashio Extensions on Air–Sea Heat Exchanges and Storm-Track Activity as Revealed in Regional Atmospheric Model Simulations for the 2003/04 Cold Season. *Journal of Climate*, 22(24).

Thiébaux, J., Rogers, E., Wang, W., & Katz, B. (2003). A new high-resolution

blended real-time global sea surface temperature analysis. *Bulletin of the American Meteorological Society*, 84(5).

Tokinaga, H., Xie, S. P., Kobashi, F., & Tanimoto, Y. (2009). Local and remote influences of the Kuroshio Extension on the atmosphere. *US CLIVAR Variations*, 7, 1-4.

Trenberth, K. E. (1981). Observed Southern Hemisphere eddy statistics at 500 mb: Frequency and spatial dependence. *Journal of the atmospheric sciences*, 38(12), 2585-2605.

Trenberth, K. E. (1991). Storm tracks in the Southern Hemisphere. *Journal of the Atmospheric Sciences*, 48(19), 2159-2178.

Trenberth, K. E., & Caron, J. M. (2001). Estimates of meridional atmosphere and ocean heat transports. *Journal of Climate*, 14(16).

Troen, I. B., & Mahrt, L. (1986). A simple model of the atmospheric boundary layer; sensitivity to surface evaporation. *Boundary-Layer Meteorology*, 37(1-2), 129-148.

Uppala, S. M., Kållberg, P. W., Simmons, A. J., Andrae, U., Bechtold, V., Fiorino, M., ... & Woollen, J. (2005). The ERA-40 reanalysis. *Quarterly Journal of the Royal Meteorological Society*, 131(612), 2961-3012.

Wallace, J. M., Lim, G. H., & Blackmon, M. L. (1988). Relationship between cyclone tracks, anticyclone tracks and baroclinic waveguides. *Journal of the*

atmospheric sciences, 45(3), 439-462.

Wallace, J. M., Mitchell, T. P., & Deser, C. (1989). The influence of sea-surface temperature on surface wind in the eastern equatorial Pacific: Seasonal and interannual variability. *Journal of Climate*, 2(12), 1492-1499.

Wernli, H. (1997). A lagrangian based analysis of extratropical cyclones. II: A detailed case study. *Quarterly Journal of the Royal Meteorological Society*, 123(542), 1677-1706.

White, G., Saha, S., 1999. Estimation of the global energy and water cycle from global data assimilation. In: Browning, K.A., Gurney, R.J. (Eds.), *Global Energy and Water Cycles*. Cambridge University Press, Cambridge, UK, pp. 55–60

Woollings, T., Hoskins, B., Blackburn, M., Hassell, D., & Hodges, K. (2010). Storm track sensitivity to sea surface temperature resolution in a regional atmosphere model. *Climate dynamics*, 35(2-3), 341-353.

Yu, L., & Weller, R. A. (2007). Objectively Analyzed Air–Sea Heat Fluxes for the Global Ice-Free Oceans (1981–2005). *Bulletin of the American Meteorological Society*, 88(4).

Zhong, S., & Fast, J. (2003). An evaluation of the MM5, RAMS, and Meso-Eta models at subkilometer resolution using VTMX field campaign data in the Salt Lake Valley. *Monthly Weather Review*, 131(7).

Zolina, O., & Gulev, S. K. (2003). Synoptic Variability of Ocean–Atmosphere

Turbulent Fluxes Associated with Atmospheric Cyclones. *Journal of climate*,
16(16).

Appendix

A.1 SYMBOLS AND PHYSICAL CONSTANTS

c	Phase speed [m s^{-1}]
c_p	Specific heat capacity of air at constant pressure [$1004 \text{ J K}^{-1} \text{ kg}^{-1}$]
C_H	Sensible heat transfer exchange coefficient
C_Q	Latent heat transfer exchange coefficient
d	Distance [m]
e	Rate of evaporation per unit volume [$\text{kg m}^{-3} \text{ s}^{-1}$]
f	Coriolis parameter [s^{-1}]
F	Front intensity parameter [$\text{K m}^{-1} \text{ s}^{-1}$]
F^*	Non-dimensional front intensity parameter
g	Gravitational acceleration [9.81 m s^{-2}]
h	Specific enthalpy [J kg^{-1}]
H	Enthalpy per unit volume [J m^{-3}]
J	Diffusive flux of water vapour [$\text{kg m}^{-2} \text{ s}^{-1}$]
k	Zonal wavenumber [m^{-1}]
l	Meridional wavenumber [m^{-1}]
l_v	Latent heat of vaporization of water [$2.26 \times 10^6 \text{ J kg}^{-1}$]
L_d	Rossby deformation radius [m]
N^2	Static stability [s^{-2}]
p	Pressure [Pa]
P	Surface precipitation [$\text{kg m}^{-2} \text{ s}^{-1}$]
PV	Potential vorticity [$\text{K kg}^{-1} \text{ m}^2 \text{ s}^{-1}$]
q	Specific humidity [kg kg^{-1}]

Q	Heat supplied per unit volume [J m^{-3}]
R_E	Radius of the Earth [$6.37 \times 10^6 \text{m}$]
Ri	Richardson number
s	Dry static energy [J kg^{-1}]
\mathbf{S}^u	Frictional force per unit mass [m s^{-2}]
t	Time [s]
T	Temperature [K]
u	Zonal velocity [m s^{-1}]
u_i	i-th component of velocity [m s^{-1}]
U	Zonal velocity at tropopause [m s^{-1}]
U_o	Background zonal velocity [m s^{-1}]
$ U_n $	Horizontal wind speed [m s^{-1}]
v	Meridional velocity [m s^{-1}]
\mathbf{v}	3D velocity vector: (u,v,w) [m s^{-1}]
V_T	Terminal velocity of raindrops [m s^{-1}]
w	Vertical velocity [m s^{-1}]
x	Zonal distance [m]
\mathbf{x}	3D position vector: (x,y,z) [m]
y	Meridional distance [m]
z	Vertical distance [m]
α	Land-dependent parameter
Γ	Tropopause height [m]
δ	Angle between the temperature gradient at 925hPa and lines of constant latitude
ε	Surface evaporation [$\text{kg m}^{-2} \text{s}^{-1}$]
ζ	Relative vorticity [s^{-1}]
θ	Potential temperature [K]

κ	Rate of condensation per unit volume [$\text{kg m}^{-3} \text{ s}^{-1}$]
λ	Longitude
Λ	Vertical wind shear [s^{-1}]
μ	Non-dimensional horizontal wavenumber parameter
ρ	Density of air [kg m^{-3}]
σ	Eady growth rate [s^{-1}]
ϕ	Latitude
Φ	Vertical component of the perturbation to the streamfunction [$\text{m}^2 \text{ s}^{-1}$]
ψ	Streamfunction [$\text{m}^2 \text{ s}^{-1}$]
ω	Rate of change of pressure [Pa s^{-1}]

A.2 ABBREVIATIONS

AFES	Atmospheric General Circulation Model for the Earth Simulator
BADC	British Atmospheric Data Centre
CCB	Cold Conveyor Belt
CNTL	Realistic (control) sea-surface temperature gradient simulation
DJF	December, January and February
EBC	Eastern Boundary Current
ECMWF	European Centre for Medium-Range Weather Forecasts
EE	Extreme Event
ERA	European Centre for Medium-Range Weather Forecasts Reanalysis
ERBE	Earth Radiation Budget Experiment
GS	Gulf Stream

GSI	Gulf Stream Index
LHF	Latent Heat Flux
LTM	Lagrangian Trajectory Model
MABL	Marine Atmospheric Boundary Layer
ME	Median Event
MSE	Moist Static Energy
MSLP	Mean Sea-Level Pressure
NA	North Atlantic
NCEP	National Centers for Environmental Prediction
NH	Northern Hemisphere
NP	North Pacific
QGPV	Quasi-geostrophic Potential Vorticity
SA	South Atlantic
SH	Southern Hemisphere
SHF	Sensible Heat Flux
SI	South Indian
SMTH	Smoothed sea-surface temperature gradient simulation
SP	South Pacific
SST	Sea-surface Temperature
UTC	Coordinated Universal Time
WBC	Western Boundary Current
WCB	Warm Conveyer Belt